NTNU

Norwegian University of
Science and Technology

# Thorium (Th) alteration veins in the Northern Trondheimfjord area

Almachius Mutasingwa

Geology
Submission date: May 2017
Supervisor: Rune Berg-Edland Larsen, IGP
Co-supervisor: Aasly Kurt, IGB

Norwegian University of Science and Technology
Department of Geoscience and Petroleum

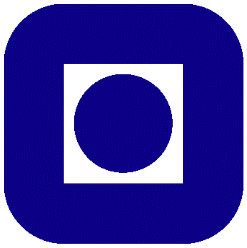

NTNU
Norwegian University of Science and Technology

# Thorium (Th) alteration veins in the Northern Trondheimfjord area

**Almachius Mutasingwa**

Geology

Submission date: December 2017

Supervisor: Rune Berg-Edland Larsen - IGP

Norwegian University of Science and Technology

Faculty of Engineering, Department of Geoscience and Petroleum

**Abstract**

Th-alteration of red carbonate veins within Ytterøy island in the northern Trondheimfjord area was investigated by focusing on field work, mineral chemistry and geochemistry. The principal aim of this thesis was to evaluate the chemistry and mineralogy of the Th-alteration in the red carbonate veins. Modal mineralogy of rocks was obtained from X-ray Diffractometry (XRD), mineral chemistry from Scanning Electron Microscope (SEM) and Electron Micro Probe Analysis (EPMA) analyses. Whole-rock and trace element of samples were obtained from Inductively-Coupled Mass Spectrometry (ICP-MS). Red carbonate veins are dominated by mineral assemblages of quartz, calcite, dolomite, ankerite, barite, microcline, epidote and hornblende whilst the lamprophyre dyke is dominated by mineral assemblages of hornblende, calcite, epidote, titanite and microcline. EPMA analyses indicate that thorogummite is the main Th source in the red carbonate veins. Overall, thorium content in samples is not equally distributed because of variable hydrothermal fluid chemistries and this has led to chemical variation even in a single phase. Thorogummite phase is highly enriched with Th up to 62.4 wt% Th whilst the red carbonate veins contains up to 77.2 wt% $ThO_2$. Similarly, Geiger Muller has detected some traces of Th concentration in some samples (up to 8 μsv/h) during the field work. Thorogummite is highly enriched with $ThO_2$ concentrations and contains relatively low uranium concentration. Thorium enrichment is thought to have occurred because of hydrothermal alteration of thorite/or Th-rich minerals and influx of external fluid rich in thorium mineralization. Hydrothermal fluids are considered to facilitate leaching and transportation of Th either from alkaline igneous complexes and/or granite rocks located at depth or near to the country rocks. High concentration of Th was observed in the thorogummite phase whilst feldspars, carbonates, sulfates, sulfides, and other silicates (i.e. epidote, hornblende, titanite) contains less/no thorium concentration. The lamprophyre dyke contains no thorogummite phase, but show some traces of thorium.

Based on geochemistry of samples, red carbonate veins are depleted in LREE mineralization whilst Lamprophyre dyke is enriched with LREE. Exception was observed in sample AM-16-003B and AM-16-007 (red carbonate vein respectively) were their REE patterns trends similar to those observed in the lamprophyre dyke. However, the fromer samples contains low REE concentrations. It was considered that, both red carbonate and lamprophyre dyke samples could have been enriched from similar process but originate from different source rocks. The distribution of lamprophyre dyke in the study area is highly limited because of being either

eroded/extracted and/or poorly exposed. With exception to lamprophyre dyke, Th-alteration in the red carbonate veins is considered to have occurred following early hydrothermal fluids interaction which later precipitated several mineral assemblages. An influx of external fluids rich in Th from a nearby alkaline igneous complex and granite rocks is also important. Both fluids were responsible for leaching, transportation and deposition of different mineral phases which were investigated in samples. Generally, the lamprophyre dyke was slightly affected with hydrothermal fluid interaction since most of its mineral texture were occassionally preserved.

**Acknowledgement**

This thesis is a part of Master of science degree in Natural Resource Management, Resource Geology at the Faculty of Engineering, department of Geoscience and Petroleum at NTNU. The whole studies were funded by Norwegian Government under Quota Scheme.

First and foremost, I express my sincere thanks to Prof. Rune Berg-Edland Larsen for accepting my suggestion on a project topic related to the mineral resource. He was a kind, motivator, guiding and giving a positive feedback on time wherever needed. I thank to Co-supervisor Kurt Aasly for his great contribution, I have learned a lot to my best of understanding. My sincere thanks to the thin section Lab staffs: Kjetil Eriksen and Arild Edin Monsøy for a better job on a thin section preparation, XRD and XRF Lab staffs: Laurentius Tijhuis and Torill Sørløkk, EM-Lab staff: Morten Peder Raanes for his time on the EPMA analyzing several thin sections which has greatly supported my thesis. Bjørn Eske Sørensen and Yingda, I really count their assistance on the SEM during the analysis. I would like to give my gratitude to the University of Smithsonian (USA), Department of Mineral Sciences which has provided the standards for Rare Earth minerals. Many thanks to Quota Scheme through Norwegian Government for providing a grant for Master studies at NTNU as well as the University of Dodoma for granting a permission to attend my studies. Also, I thank Anette Utgården Granseth, Emily B Kiswaka, Chone Lugangizya and Ida Jahanne Svendsen Røisi, I appreciate their time and constructive ideas towards my thesis. Finally, thanks to my family, classmates and Tanzanian people living in Trondheim, they have been encouraging, advising and inspiring all the time I was here in Trondheim.

Table of content

# List of figures

# List of tables

**Abbreviations**

**EDS** – Energy Dispersive X-ray Spectrometry

**BSE** – Back Scatter Electron

**LREE** – Light Rare Earth Electron

**HREE** – Heavy Rare Earth Element

**XPL** – Cross polarized light

**PPL** – Plane polarized light

**REE** – Rare Earth Element

**NTNU** – Norwegian University of Science and Technology

**APT** – Apatite

**QTZ** – Quartz

**MICR – Microcline**

**DOL** – Dolomite

**EPT** – Epidote

**HLB -** Hornblende

**SEM** – Scanning Electron Microscope

**SE** – Secondary Electron

**XRF** – X-ray Fluorescence

**XRD** – X-ray Diffractometry

**EPMA** – Electron Probe Micro Analysis

**ICP-MS** – Inductively Coupled Mass Spectroscope

**WDS** – Wavelength Dispersive X-ray Spectrometers

**NYF** – Niobium – Yttrium – Fluorine

**HFSE** – High Field Strength Elements

**MTFZ** – Møre Trøndelag Fault Zone

**LCT** – Lithium – Cesium - Tantalum

**THGT** – Thorogummite

**PY** – Pyrite

**BRT** – Barite

**FRT** – Fluorite

**DPS** – Diopside

**ALB** – Albite

**ANK –** Ankerite

**$CO_3^{2-}$ -** Carbonate

**GSQ** – Geological Survey of Queensland

# Chapter 1

# Introduction

## 1.1 Previous study

Møre-Trøndelag Fault zone (MTFZ) is located in Central Norway within the Trondheimfjord area (Figure 1) in which the Ytterøya Island is situated in the central part (Figure 2) (Grønlie & Torsvik, 1989). The fault lies between the islands of Hitra and Smøla, where it can be followed through the inland area and along the coastline from Nord Trøndelag (WSW) to Sør-Trøndelag and Møre respectively (Gabrielsen & Ramberg, 1979). About 700 red-colored veins, alteration zones and breccias have been reported within MTFZ (Grønlie & Torsvik, 1989) that are dominated by thorium (Th) and iron-carbonate minerals (Grønlie & Torsvik, 1989). Dominant veins cut through metasediments, metavolcanics and igneous rocks in the nappes of Middle and Upper Allochtons (Wolff, 1976). Most of the veins and breccias are controlled by joints and faults formed during the late stage of extensional faulting (Grønlie & Torsvik, 1989). Some of the breccias are reported to follow an earlier faults formed during the Late Devonian/Early Carboniferous collision and docking and strike-slip within MTFZ (Sturt et al., 1987; Grønlie & Torsvik, 1989). The entire formation processes of veins and breccias were accompanied by flux of hydrothermal fluids that led to alteration of host rocks and precipitation of various mineral assemblages. The earliest alteration phenomena involved Sodium (Na) metasomatism which has precipitated iron carbonates (Grønlie & Torsvik, 1989). Consequently, potassium (K) metasomatism led to the deposition of quartz, calcite and fluorite. During metasomatism hydrothermal fluids reacted with the host (red carbonate veins) that has resulted in the formation of different styles of alteration (Grønlie & Torsvik, 1989; Robb, 2005). Due to intensity, composition as well as hydrothermal pressure of the reacting fluids, different phenomena within the host rock have been reported. Among these include; a single-thin red vein, swarms of sometimes interconnecting red veins, hydrothermally altered benches of host rock, major breccia zones up to 10 m wide, and highly radioactive quartz/K-feldspar/haematite/thorium-mineral rich breccia (Grønlie & Torsvik, 1989).

Mineral assemblages within MTFZ identified in the veins and breccias by microscopy, XRD, SEM and XRF analytical methods. XRD and SEM show the dominance of quartz, microcline or adularia, ankerite-dolomite, calcite, siderite, albite, apatite and fluorite. Geochemistry of

veins and breccias were reported by using XRF and microprobe analysis which has indicated Th and REE (Ce, La and Y) as a dominant trace element in samples. However, their total concentration is lower compared to the Th concentration (i.e. Th > Ce + La). Microprobe analysis reported thorogummite ($Th(SiO_4)_{1-x}(OH)_{4X}$) and cheralite ((Th, Ca, Ce) ($PO_4$, $SiO_4$)) as major thorium hosting minerals, which occur as dusty, irregular and minute inclusion in K-feldspars (Grønlie & Torsvik, 1989). Major element analysis of $ThO_2$ content in thorogummite and cheralite indicated (48-56 wt%, Th) and (25-27 wt%, Th) respectively (e.g., Grønlie 1984; in Grønlie & Torsvik, 1989). Grønlie & Torsvik, (1989) reported 760 ppm Th as an average concentration in veins and breccias. Variable Th concentration in the iron-carbonate veins (100-500 ppm), feldspathic fenites and thorium enriched breccias (0.1 wt % - 0.2 wt%) are also reported (Grønlie & Torsvik, 1989).

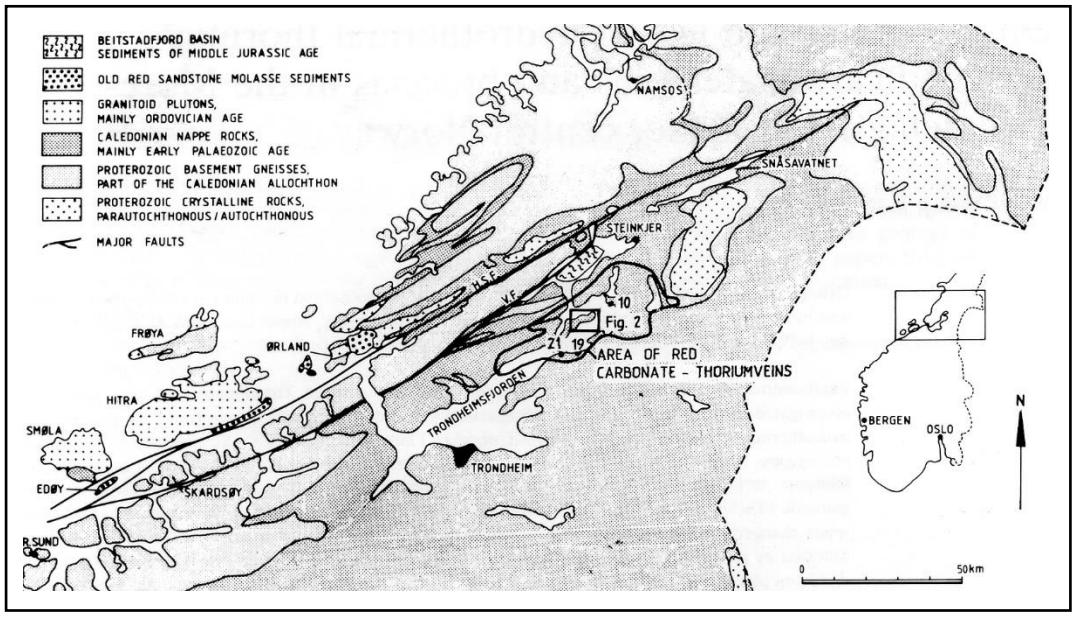


Figure 1. Map showing the location of Møre Trøndelag Fault Zone (demarcated by NE-SW trending lines) (Grønlie & Roberts, 1989).

In the center of the Trondheimfjord area, the Ytterøy island (Fig.2) is characterized by an ultramafic Lamprophyre dyke (Grønlie & Torsvik, 1989). The formation of the dyke (intrusion) is considered as a first stage of igneous activity within the island and occurred during the Permian time (Carstens, 1961). The dyke is located 50 km NNE of Trondheim in the central part of the fjord. It is Lower Ordovician in age with a NE-SW orientation, 80-90 cm thick and ca. 14 km long with an attitude of ca. 060°/70° SE. It is also characterized with sharp and chilled marginal zones between limestone and Lamprophyre.

The dyke is mainly dominated by an assemblages of olivine, biotite, clinopyroxene, calcite, analcite and magnetite whilst K-feldspar and apatite occur as accessory minerals. The Island is dominated by meta volcanic rocks such as greenschist and quartz-augen-gneisses which form the lithostratigraphic unit (Støren group) within the Trondheim region (Carstens, 1961). In the SW, the Island comprises 20-25 m strongly deformed schistose greenstone lithologies (Mitchell & Roberts, 1986b).

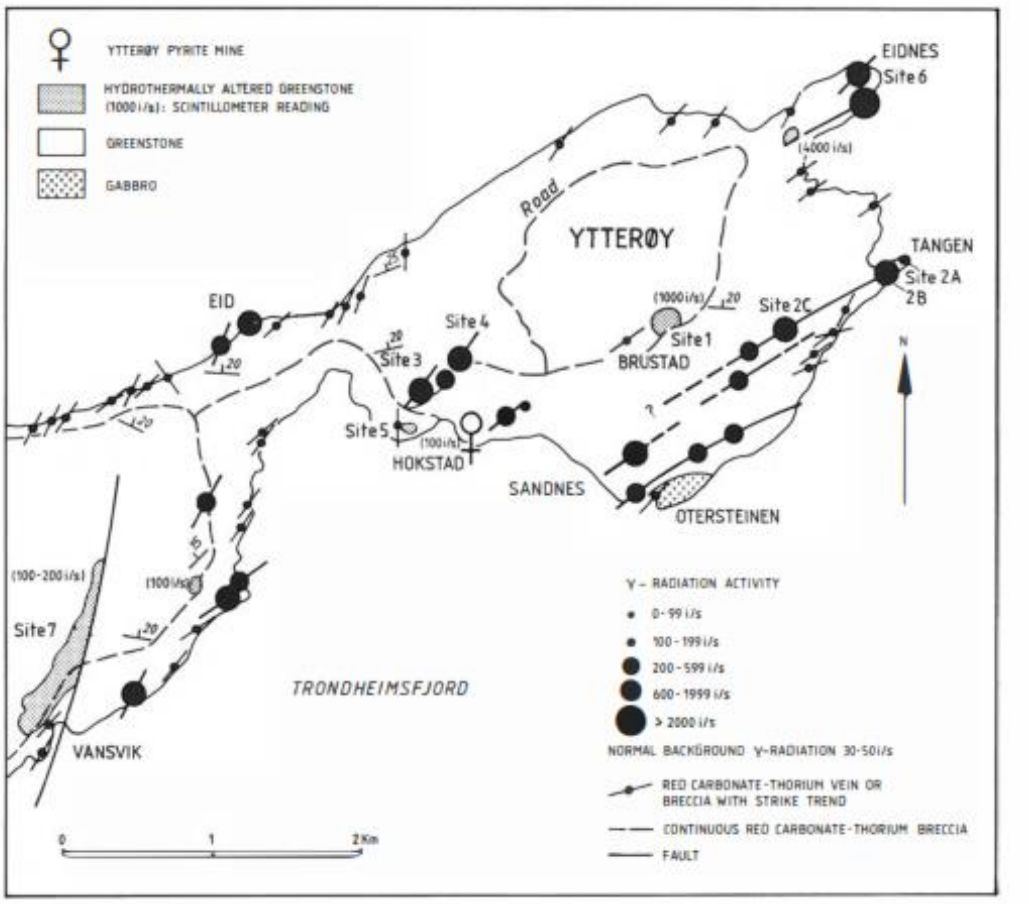


Figure 2. Location map showing the Th-rich locations at Ytterøya Island (Grønlie & Torsvik, 1989).

## 1.2 Aim of thesis

This project is focusing on the thorium alteration of veins in the Northern Trondheimfjord area mostly on the Ytterøy island. The island is dominated by veins and breccia, which are enriched in thorium content up to 1.3 wt% (Grønlie & Roberts, 1989). These mineralizations occur in veins as hydrothermal alteration product of the mineral thorite to form thorogummite (Burt, 1989a).

The entire process of thorium mineralization in these veins occurred due to Th alteration which need to be investigated particularly because as much as 1 wt% was reported (Grønlie & Roberts, 1989), in comparison to the average crustal abundance of 7.2 ppm (Kara & Committee, 2008). Due to high Th concentrations, a detailed study in determining the chemistry and mineralogy of the thorium bearing veins became the principal aim of this thesis work. Mineralogy, geochemistry and field observations undertaken will seek to confirm the amount of Th and the process that has led to thorium alteration within veins/breccia. To understand the entire process, the following task have been performed to accomplish this study: (1) field mapping of the veins and breccias related to thorium alteration processes (2) Mineralogy, mineral chemistry and bulk chemistry for selected samples to identify minerals associated with veins/breccias (3) Discuss the origin of fluids that led to Th-mineralizations within veins/breccias. In addition, previously applied techniques (Grønlie & Roberts, 1989) such as scanning electron microscope (SEM) and X-ray Diffractometry (XRD) will be employed. The study will incorporate electron probe micro analysis (EPMA), inductively-coupled mass spectrometry (ICP-MS) and petrographic studies in order to better understand the formation of these unusal deposits.

## 1.3 Background

### 1.3.1 Regional geology

The initial stages of MTFZ are linked to the tectonic evolution of NW Europe (Grønlie & Roberts, 1989). In the Trondheimfjord area the formation of MTFZ is related to the Scandinavian Caledonides. The Caledonides are generally categorized into four major allochthonous units each comprising numerous nappes (David Roberts & Gee, 1985). These units include; Lower, Middle, Upper and Uppermost allochthons units (Slagstad et al., 2014). The effects of the Caledonian orogenesis in the Trondheimfjord area is marked by the faulting of the basal Precambrian crystalline bedrock complex of heterogeneous gneisses characterized by meta-granitoids and meta-gabbros (Grønlie & Roberts, 1989). Orogenesis effects has led to transpression and sinistral strike-slip shear movement as a result of oblique collision between the Baltica, Laurentia and intervening microcontinent fragments (Grønlie & Roberts, 1989) during Devonian period (Figure 4). Several individual faults within MTFZ of about 20-30 km wide were identified (Oftedahl, 1972) following an interpretation of lineament images derived

by the Landsat-borne Multispectral Scanner (Gabrielsen & Ramberg, 1979). The separation of Laurentia, Gondwana and Baltica occurred during Early Palaeozoic Appalachian-Caledonian orogenic belt formation (Van Staal et al., 1998). Separation of landmasses occurred in response to closure of Iapetus, Tornquist and Rheic oceans (Van Staal et al., 1998; Cocks & Torsvik, 2002). Closure of the oceans took place during the Late Cambrian time and was marked by the formation and obduction of suprasubduction-zone ophiolites and primitive island-arc assemblages. Rearrangement process of whole landmasses and it associate formations are now preserved along the Caledonian – Appalachian orogenic belt (Figure 3). These events were followed by succession of more mature oceanic and / or continental arcs on top margins of the continental lithosphere. The succession continued relative to the proceeding closure during active Mid-Silurian to Early Devonian continental-continental collision (Slagstad et al., 2014).

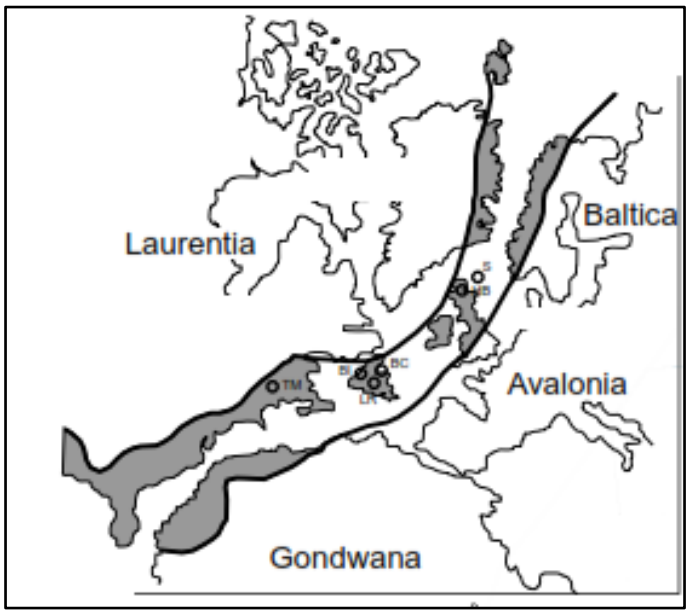


Figure 3. Some ophiolite occurrences in the Appalachians, highlighting the similarities in timing of formation and obduction between the Caledonian and Appalachian ophiolites (Slagstad et al., 2014).

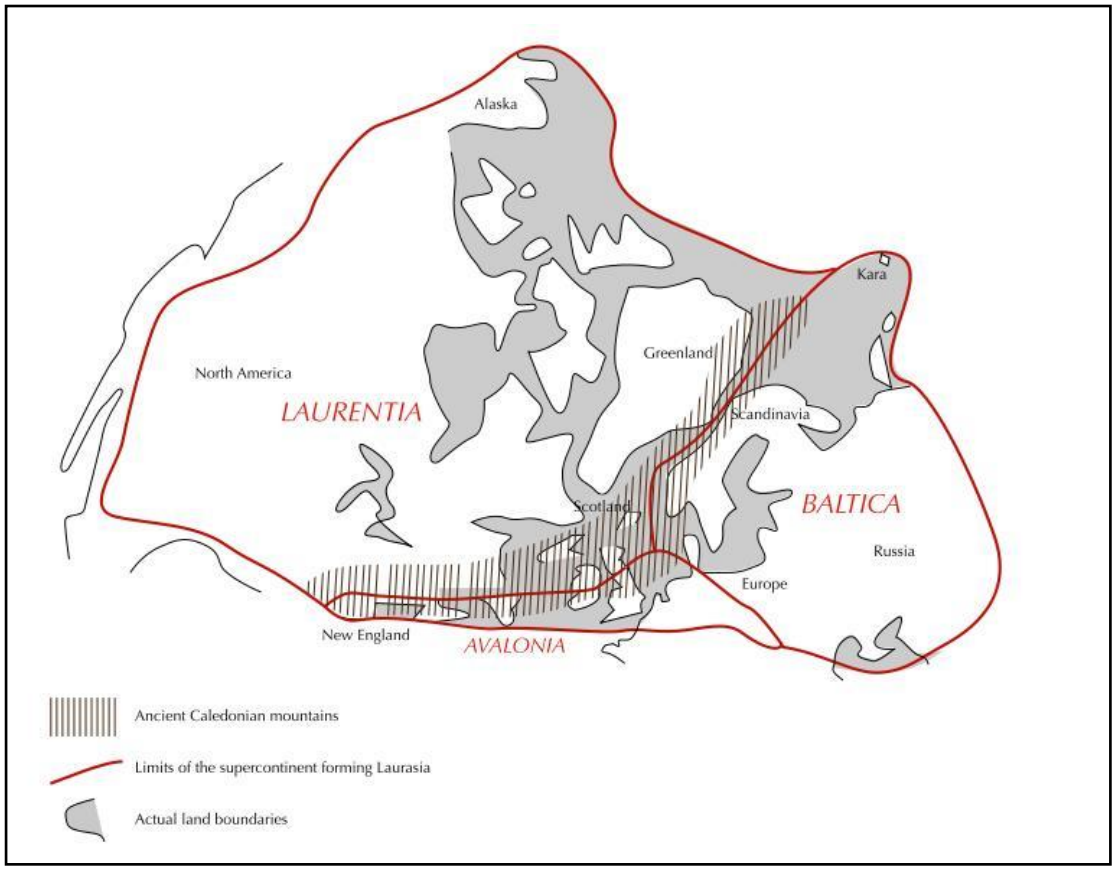


Figure 4. Palaeogeographic reconstruction showing positions of Laurentia, Baltica and Avalonia during Devonian (Robert, 2007).

Opening and closure events led to several tectonic regimes that has continuously affected the Trondheimfjord area. These tectonic regimes occurred during Paleozoic time and are characterized by sinistral-strike shear movements (Grønlie & Roberts, 1989). These tectonic regimes include: development of secondary dextral strike-slip in western Norway including MTFZ (David Roberts, 1983); Devonian fold structures in the Stjørnfjord-Hjellebotn (D Roberts & Sturt, 1980) and; Variscan Orogeny during Devonian to Carboniferous due to assemblage of the Gondwana and Baltica-Laurentia supercontinents (Ziegler, 1981) which led to formation of the Pangea supercontinent (Figure 5) during Carboniferous (Torsvik & Van Der Voo, 2002).

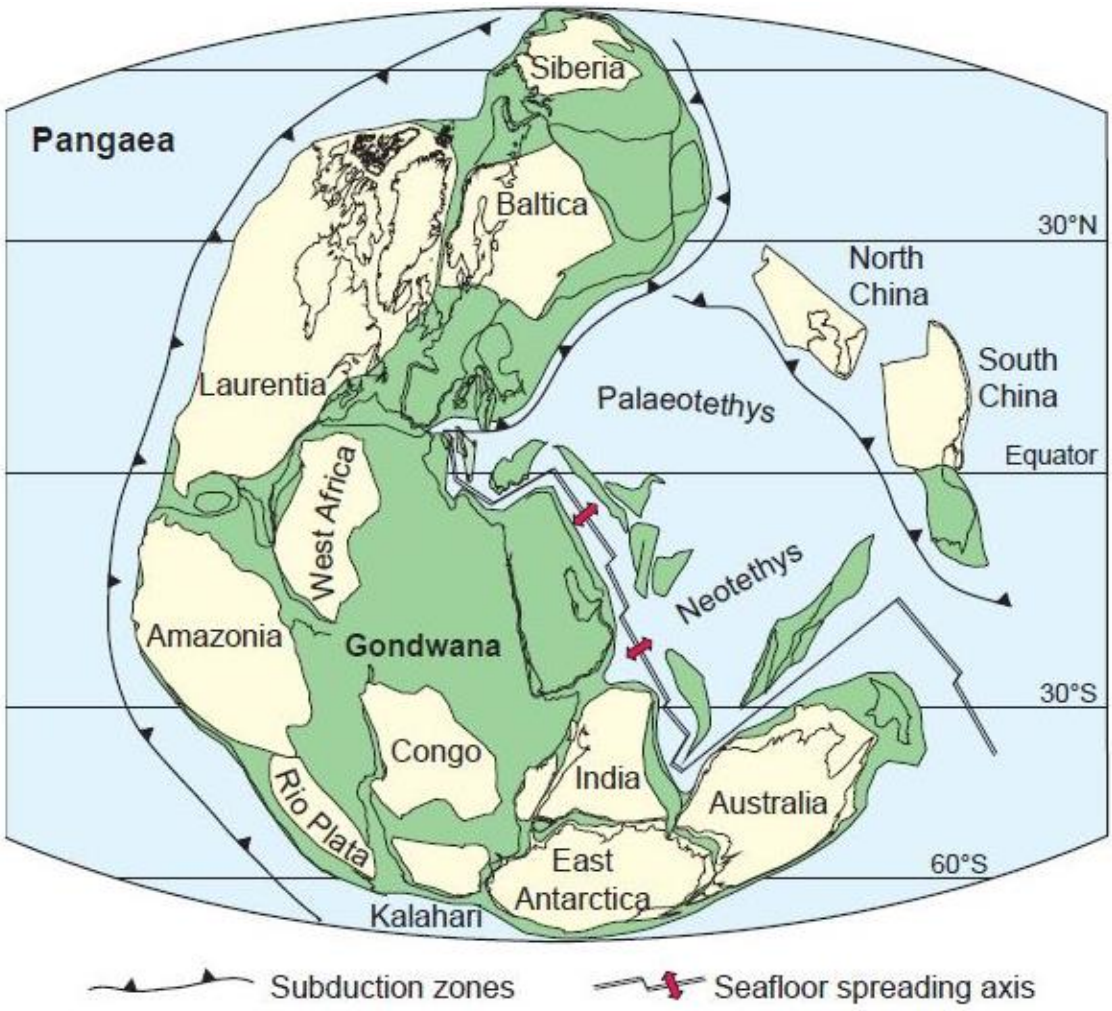


Figure 5. The Pangaea supercontinent in the Late Permian (Torsvik, 2003).

Paleozoic time was dominantly characterized by plate accretion followed by an intensified rifting activities in the North Atlantic region (Grønlie & Roberts, 1989). O the other hand, an extension regime during Mesozoic time lead to the fragmentation of the Pangea supercontinent and consequently opening of the Atlantic Ocean that began from the Arctic rift system and propagated southward (Coward, 1995). These tectonic processes led to re-activation phenomenon of earlier formed faults from sinistral strike-shear movement to dextral strike-slip movement (David Roberts, 1983). Timing of these tectonic episodes within the Trondheimfjord area was best derived using Palaeomagnetic and radiometric dating of fault rocks (Sturt et al., 1987). The results indicate different stages of rifting, magmatism and hydrothermal activity (Grønlie & Torsvik, 1989) which include: intrusion of Ytterøya Lamprophyre dyke which marks the first stage of igneous activity during the Permian time (Carstens, 1961), Na-metasomatism as well as precipitation of iron-carbonate as well as K-metasomatism controlled

by thorium enriched breccias (TE-breccias) during the Late Jurassic/Early Cretaceous and deposition of the minerals quartz, calcite and fluorite in the joints (Grønlie & Torsvik, 1989).

### 1.3.2 Geology of Ytterøya

Ytterøya Island is in the central part of the Northern Trondheimfjord area (Grønlie & Torsvik, 1989). It is dominated with schistose greenstone that are variably deformed and dip in the Northeast (Figure 3). The island contains variable mineral assemblages of dark amphibole-rich types to pale green and chloritic schist (David Roberts & Tucker, 1998). The greenstone succession is sub-divided into three parts that form a part of Trondheim Nappe Complex (e.g. Wolff, 1979. These include a layer of metalimestone 30 – 60 m thick in the south west of the island (e.g. Trønnes, 1993 in David Roberts & Tucker, 1998), the meta-gabbro in the northeast at Oterstein and plagiogranitic (trondhjemite) sheets in the northwest (David Roberts & Tucker, 1998). Ultrapotassic lamprophyre dykes cuts metalimestone (Carstens, 1961). Regional mapping and lithostratigraphic correlation suggest an Ordovician age of both greenstone, metalimestone and metatrondhjemite sheets (Carstens, 1961; Mitchell & Roberts, 1986a). The age of other associate rock types (i.e. mafic volcanites and limestone) was reported relatively by the lamprophyre dyke that can be either Devonian or Permian (cf. Torsvik et al., 1994).

Based on petrographic study, foliated metatrondhjemite is mainly dominated with quartz and plagioclase as a major mineral. K-feldspar, muscovite and clinozoisite constitute minor composition of the rock whilst apatite, zircon, sphene and chlorite form the accessory minerals. The metalimestone is composed of bands and schistose which dips at ca.30$^{o}$ toward NE/NNE. The base of the metalimestone have been continuously arranged into the schistose greenstone with diverse transitional units of phyllite, banded tuff and thin ribs of limestone (David Roberts & Tucker, 1998). The upper contact of the succession is dominated with shear bands of phyllonite and protomylonites which indicate a contractional oblique-slip movement. In addition, calc-phyllite, dark-grey phyllites, greenschists, tuffs and thin bands of limestone have been found to occur above the contact passing up into the greenstones. The island also contains several limestones that occur in the Støren Nappes, for example those of Hølonda, Meldal and Tautra areas were reported to contain no any fossils or microfossils (Robert and & Tucker, 1998).

In general, supracrustal rocks within the island were reported to have been affected by deformation and metamorphic processes during the Scandian Orogeny. The whole processes are considered to take place during the Late Silurian to Early Devonian time (David Robert & Tucker, 1998).

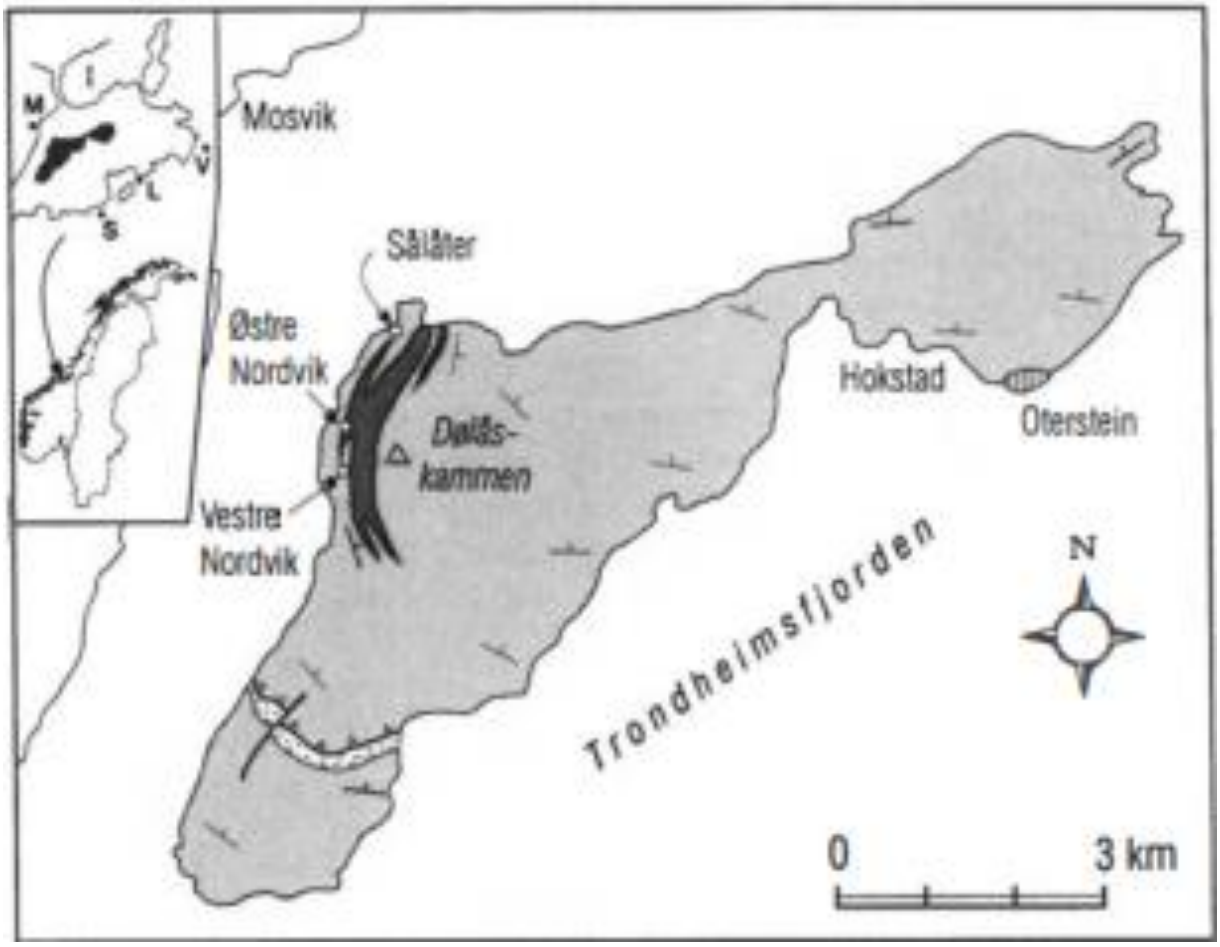


Figure 6. A simplified geological map of Ytterøy showing the metatrondhjemite (dark grey) and schistose greenstone (pale grey). The orientation of the compositional banding/foliation is shown by the strike-dip symbols (David Robert & Tucker, 1998).

# Chapter 2

# Theory

## 2.1 Thorium

Thorium is a chemical element in the periodic table with **Th** symbol and atomic number 90 (Barthel & Tulsidas, 2014). It is soft, silver-grey, very ductile, heavy and metallic element which form the actinides series in the periodic table (GSQ Report, 2014). The element is slightly radioactive and occur naturally in a single isotope $^{232}Th$ with half-life of ca. 14 Ga (Hazen et al., 2009). Thorium occur in small amounts in the Earth's crust where it accounts up to three times than uranium and the total potential energy of thorium is more than potential energy of uranium and fossil energy if combined (Encyclopedia Britannica, 2009). This can be used as a replacement of uranium in the nuclear power generation. In most cases, Th occur as an oxide (thorianite) or a silicate (thorite). It is incorporated in several minerals such as hydroxides, phosphates (monazite) and carbonates (rare) but more widely distributed in accessory minerals such as monazite, brockite, xenotime and euxenite (Van Gosen et al., 2009). Thorium is commonly known to have high radioactive properties of which could

The major ore minerals of Th are often isochemical and contains a series of solid-solution between end members, for example thorianite ($ThO_2$), cerianite ($CeO_2$), and uraninite ($UO_2$); thorite ($ThSiO_4$), coffinite ($USiO_4$) and zirconium ($ZrSiO_4$) as well as monazite (Ce, La, Th, U) $PO_4$ (Blundy & Wood, 2003; Hazen et al., 2009). However, thorougummite has been reported to contain high concentration of thorium. The mineralization form as a result of hydrothermal alteration of thorite (Piilonen et al., 2014). It is highly concentrated in silica-rich rocks such as granites (Kara & Committee, 2008) as well as in alkaline igneous rocks (example; nepheline syenite), carbonatites, placers and vein types (Van Gosen et al., 2009; Barthel & Tulsidas, 2014).

Like uranium (U), it is radioactive with similar crystal chemistry (size and charge that possess a tetravalent state ($Th^{4+}$). Due to similar ionic size and charge, both thorium and uranium substitute other minerals forming thorutite; [(Th, U, Ca) $Ti_2$ (O, $OH)_6$], huttonite; [(Th, U) $SiO_4$] and Cheralite [(Ce, Ca, Th, U) (P, Si) $O_4$] (Hazen et al., 2009). $Th^{4+}$ and $U^{4+}$ form a solid-solution but behave differently in the aqueous fluids because of different incorporated complexing agents such as $F^-$, $Cl^-$, and $CO_3^{2-}$ (Keppler & Wyllie, 1990; Hazen et al., 2009). Complexing agents controls the solubility behavior of $Th^{4+}$, $U^{4+}$ and $U^{6+}$ ions within

hydrothermal solution, however, weathering and other geological processes are also important. Hydrothermal fluids rich in chloride and/or carbonate as complexing agent favors $U^{4+}$ and $U^{6+}$ whilst $Th^{4+}$ form insoluble solution except when it occurs as Th-fluoride complexes (Hazen et al., 2009). In addition, Th and U show distinct geochemical associations under weathering and near-surface geological processes. For example, uranium oxidizes to $U^{6+}$ to form soluble and mobile uranyl $(UO_2)^{2+}$ ions which precipitate in reducing condition whilst less mobile thorium concentrate in placers (Kara & Committee, 2008). In magmatic process $U^{4+}$ forms more stable mineral complexes than $Th^{4+}$ at elevated temperature and pressure (Keppler & Wyllie, 1990). Both $Th^{4+}$ and $U^{4+}$ ions have a strong affinity with phosphates, niobates, tantalates and titanites in which they substitute REE (Finch & Murakami, 1999; Van Gosen et al., 2009). This is attributed to the incompatible nature of Th and U during primary fractionation of igenous melts.

## 2.2 Metasomatism processes

International Union of Geological Sciences (IUGS) defines *metasomatism* as "a metamorphic process whereby the chemical composition of a rock or rock portion is altered in a pervasive manner and involves the introduction and/ or removal of chemical components because of the interaction of the rock with aqueous fluids (solutions)". During metasomatism the rock remains in a solid state (Yardley, 2013). The most important sources of metasomatic fluids are sedimentary basin brines and magmatic fluids; however, mantle and metamorphic fluids are also important. It is associated with brines whereby highly concentrated brines are very effective metasomatic agents (Yardley, 2013). Robb, 2005 reported four main types of aqueous fluids that interact with rocks owing to addition or removal of chemical components. These includes; sea water, meteoric water, connate water and metamorphic water. *Sea water*, is weakly saline and constitute the largest reservoir on the Earth's surface (70%). It is extensively circulating throughout the ocean crust and is responsible for widespread alteration and metal redistribution (Robb, 2005). Major dissolved components are the cations $Na^{+}$, $K^{+}$, $Ca^{2+}$ and $Mg^{2+}$ and anions $Cl^{-}$, $HCO_3^{2-}$ and $SO_4^{2-}$ (Holland, 2003; Pirajno, 2009). *Meteoric water*, comprises the hydrological cycle and has been through the atmosphere. It is stored as groundwater in soil profiles and the upper crust, in lakes and in glaciers including the polar ice caps (Robb, 2005). Meteoric water may penetrate the earth's crust through fractures to deeper levels where it may be involved in the formation of hydrothermal ore deposits.

Ore deposits typically formed at relatively low temperatures which include sandstone-hosted uranium ores and Mississippy ValleyType Zn-Pb deposits (Robb, 2005). *Connate water* fills the pore-spaces of unconsolidated sediments. It undergoes significant modification when the sediments are buried, compacted and lithified. Various stages of diagenesis that results in transformation of uncompacted particles of sediments into sedimentary rock produce large volumes of aqueous fluid. These aqueous fluids usually evolve with time and depth through sedimentary sequences (Robb, 2005). *Metamorphic water*, forms during dehydration reactions of hydrous minerals to less hydrous or anhydrous phases; for example kaolinite → Pyrophyllite (300$^{o}$C) and muscovite and chlorite → Biotite (400$^{o}$C) (Robb, 2005). This takes place through burial processes and temperatures that exceed 200$^{o}$C producing minerals with less volatiles than before. Several aqueous species are associated with metamorphic fluids including; $H_2O$, $CO_2$ and $CH_4$ (Robb, 2005). *Magmatic fluids*, are fluids which form during emplacement and crystallization of igneous melts. They comprises incompatible elements partitioning from the melt (Yardley, 2013) or extracted during fluid-rock interaction processes (Pirajno, 2009).

Metasomatism is distinguished from other endogenic processes (e.g. Zharikovf, 1998 in Zharikovf, 2007) as follows:-

1) From ion-by-ion replacement in minerals, a mechanism in which mineral dissolution occurs simultanously with precipitating of new minerals under the maintenance of a constant volume.
2) Infilling of cavities or cracks, magma crystallization, and magma-rock interactions, through a preservation of the rock.
3) From magmatism and metamorphism by the formation of a regular set of zones. These zones form a characteristic pattern (metasomatic zones) across the metasomatic body. The zonal pattern represents chemical equilibration between two rocks or between a rock and a filtrating fluid (solution).

Based on the nature of mass transport, metasomatism is grouped into two main types which include, diffusional and infiltrational metasomatism (Korzhinskii, 1957; Bach et al., 2013). *Diffusional metasomatism* refer to a process whereby the solutes diffuse through a stagnant solution (fluid) and is driven by chemical potential gradients in the rock and/or fluid. *Infiltrational metasomatism*, is fluid infiltration driven by pressure and concentration gradients. However, other types of metasomatism such as autometasomatism, boundary metasomatism,

bimetasomatism and near-vein metasomatism can be recognized during magmatic and postmagmatic stages (Korzhinskii, 1957).

## Types of metasomatism

## Hydrogen ion ($H^+$) metasomatism

This involve the liberation of H+ ions during decomposition process, for example decomposition of potassic minerals by hydrothermal solution (Pirajno, 2009). Production or consumption of $H^+$ changes the pH of the hydrothermal solution especially at processes involving a conversion of anhydrous silicates to hydrous one (e.g. mica or clay) or vice - versa.

## Sodic metasomatism

This take place by a replacement of alkali feldspar with albite (albitisation or Na-feldsphathisation) (Pirajno, 2009). The replacement process proceed from a pre-existing perthite or through a direct replacement of alkali feldspar to form albite (Pollard, 1983). Sodic metasomatism (albite-rich rocks) are usually associated with rare elements (Nb, Ta, Sn, W, Be, Li) and formaton of Th, U, Zr, Fe and HREE deposits (Pirajno, 2009). Many of the albite-rich rocks are leucocratic and are identified by their mineralogy. Based on mineralogy, albite-rich rocks are dominated by albite and quartz with some residual primary feldspars (Pirajno, 2009).

## Potassic metasomatism

This involves potassium (K) for Sodium (Na) exchange of mineral reactions and represent the replacement of albitic plagioclase by microcline or orthoclase (Pirajno, 2009). Exchange process of K for Na results into growth of mica with a composition ranging from annite forming from decomposition Fe-rich members and amphibole (Bowden, 1985). K-feldspathisation is generally confined to the roof zones of granitic intrusion, and it is related to initial high T stages of vapor separation from the silicate melts (Pirajno, 2009).

## Hydrothermal/Hot fluids

Hot aqueous fluids have the ability to carry metals and ions in solution that are derived from a silicate melt or leaching of infiltrating lithologies. Hydrothermal fluids react with wall-rocks and /or country rocks causing a change in physio-chemical condition through addition or

removal or redistribution of constituents (metals and ions) (Lagat, 2007). Fluid interaction that result into the addition/removal and redistribution of constituents in the wall-rocks is known as hydrothermal alteration (Lagat, 2007; Pirajno, 2009). Alteration take place because mineral assemblages within rocks are in a physio-chemical disequilibrium with the hydrothermal fluids. Rocks that are altered with hydrothermal fluids tend to re-equilibrate by forming new minerals that are stable at the new conditions (Pirajno, 2009). The entire process occurs depending on several factors such as chemical composition of both fluids and the rocks, nature of the fluid, pressure and temperature (Lagat, 2007). Hydrothermal systems comprises two major components, the *heat source* which provide the necessary heat energy (e.g. magmatic, geothermal gradient, radiogenic decay and metamorphism) and *a fluid phase* comprising solutions derived from magmatic/juvenile, meteoric fluids, metamorphic fluids and connate waters or sea waters (Pirajno, 2009). It may be an actively convective hydrothermal system consists of a recharge, circulation and discharge systems where most of carried metals and ions are deposited as a mineral either in a single conduit or a channelways, or a fine network of fractures (Pirajno, 2009). Generally, the hydrothermal fluids are controlled through faults, fractures and permeable lithologies towards the deposition sites (Pirajno, 2009; Yardley, 2013). Hydrothermal systems (Cox, 2005; Pirajno, 2009) may also be considered in terms of fluid flow whereby the development of hydrothermal mineral systems is transported from a large-volume reservoir through a progressively smaller network to the depositional site (i.e. faults, fractures and shear zones) (Pirajno, 2009).

## Style of hydrothermal alteration

Style of alteration describe the intensity, form and behavior of the hydrothermal alteration. Major styles of alteration are pervasive, selective pervasive and non-pervasive alteration (Pirajno, 2009), respectively. The styles describe the state of preservation of the original rock, for example; how far the hydrothermal process has affected the minerals/rocks at both the single mineral and regional scale and the overall geometry and appearance of the alteration halo etc. Pervasive alteration take place by replacement of most or all original rock-forming minerals and result into destruction of original textures. Selective pervasive alteration occurs through replacement of specific mineral(s) within a rock and is characterized by the preservation of original texture, for example; chlorite replacing biotite.

# Types of hydrothermal alteration

**Potassic alteration**.

Potassic alteration forms a mineral assemblages of K-feldspar and/or biotite accompanied with minor amounts of sericite, chlorite and quartz (Robb, 2005). It represents high temperature (500-600$^{o}$C) alteration typically associated with porphyry Cu-deposits and epithermal mineralizing systems (Robb, 2005; Pirajno, 2009).

**Propylitic alteration**.

Propylitic alteration describe the alteration process that take place in mafic rocks and is accompanied with addition of $H_2O$ and $CO_2$ as well as S with minor amount of $H^+$ metasomatism (Pirajno, 2009). It is characterized by mineral assemblages of epidote, chlorite, carbonates, albite, K-feldspar and pyrite (Lagat, 2007; Pirajno, 2009) and typically acts at 300-450 oC.

**Phyllic (Sericitic) alteration and Greisenisation**

Phyllic or sericitic alteration, involves hydrolysis of feldspars to form sericite (white mica) and quartz + minor chlorite and pyrite (Robb, 2005; Pirajno, 2009). This is the most common type of hydrothermal alteration of quartzo-feldspatic rocks (Robb, 2005) and typically occur at 300-400 oC.

**Argillic alteration**

Argillic alteration generate clay-minerals suc as kaolinite, illite and smectite (Lagat, 2007) due to strong $H^+$ metasomatism, acid leaching and very high fluid/rock ratios. This type of alteration occurs between 100ºC and 300ºC and it is commonly associaed with batholitic granitic systems (Pirajno, 2009). Argillic alteration is sub-divided into intermediate and advanced alteration depending on the intensity host rock decomposition (Robb, 2005). *Intermediate argillic alteration* mainly affects plagioclase (Robb, 2005) and it is characterized by montmorillonite, illite, and other clay minerals (kaolinite, dickite, halloysite, hallophane) and minor sericite (Pirajno, 2009). *Advanced argillic alteration* occurs due to very low pH resulting into more or less complete leaching of the alkali ions. The process results into complete destruction of the feldspars and mafic silicate phases (Pirajno, 2009). This type of alteration is dominated by a

mineral assemblages of dickite, pyrophyllite, barite, alunite, diaspore, kaolinite, quartz, hematite and limonite (Lagat, 2007; Pirajno, 2009).

**Carbonatization**

Carbonatization imply the formation of carbonate minerals such as calcite, dolomite, magnesite, siderite and ankerite during alteration of the host rock (Robb, 2005; Pirajno, 2009). It is characterized by high ($P_{CO_2}$) and neutral to alkaline pH. The alteration process is also associated with minerals such as talc, chlorite, sericite and albite (Lagat, 2007).

**Silication and Silicification**

In silication and silicification the former involves the conversion of carbonate minerals to form calc-silicate minerals. It occurs when fertile and acidic magmatic fluids infiltrate carbonate rocks to form polymetallic skarn deposits during the prograde stage at high T (>450 $^{o}$C). Silicification occur through the formation of new quartz or amorphous silica in a rock during alteration (Robb, 2005) typically at low and intermediate temperatures (c. 200 – 400 $^{o}$C).

## 2.3 Lamprophyre

Lamprophyre refers to an ultrapotassic rocks that are chemically classified as lamproites, Kamafugites and plagio-leucites (i.e. Group I, II and III respectively) (S. Foley, 1992). In terms of major elements, ultrapotassic rocks are defined by $K_2O/Na_2O$ >3 wt%, $K_2O$ >3wt % and MgO >3wt % (S. F. Foley et al., 1987). These groups of rocks are differentiated from a common alkaline rocks. The Kamafugites group (S. Foley, 1992) is characterized by low $SiO_2$, $Al_2O_3$, $Na_2O/Al_2O_3$, $Na_2O$ and high CaO contents. These rocks occur in association with carbonatite within continental rift environments (Nixon & Hornung, 1973). The main rock types associated with lamprophyre include; olivine melilitites, perovskite and Kalsilite characterized by low silica content (i.e. $CO_2$ rich environment) (S. F. Foley et al., 1987; S. Foley, 1992).

The rocks are enriched in incompatible trace elements (Ba, Rb, Sr, Zr, Nb, Y, La, Ce, Nd, Sc, V, Ni and Cr), high $K_2O$ and $K_2O/Na_2O$. Enrichment of these elements indicate a close relationship to partial melting of garnet peridotite mantle which have been affected by metasomatic processes (S. F. Foley et al., 1987; Edgar & Vukadinovic, 1992). On experimental studies Edgar and Vukadinovic (1992) reported that the magma, which form ultrapotassic rocks

occur prior to partial melting of a metasomatic enriched-mantle sources at depth of c. 100km. These processes of mantle enrichment and partial melting facilitated the chemical variations among other related rocks such as lamproite and plagio-leucite (S. F. Foley et al., 1987). Lamproitic and Kamafugite magmas are derived from partial melts associated with phlogopite-harzburgite (with $H_2O$ and F volatiles) and wehrlitic mantle sources (with $H_2O$, $CO_2$ and/ or F as dominant volatiles) respectively (Edgar & Vukadinovic, 1992). Type of magma and incompatible element composition that form prior to partial melting (i.e. either Lamproitic or kamafugite) depend much on the composition and nature of the fluids (S. F. Foley et al., 1987). Experiments done by Schneider and Eggler (1984) show that $H_2O$-rich phases can carry more solute compared to $CO_2$-rich phase. However, $CH_4$-$H_2O$ carry small amount of solute due to $CH_4$ having low ability to dissolve appreciable amounts of solutes (e.g. Taylor, 1985 in S. F. Foley et al., 1987). Schneider and Eggler (1984) reported that most of these vapor phases play a major role by removing some of the material brought in with melts during crystallization processes. S. F. Foley et al. (1987) reported similar observation where by water rich fluids transport silica and incompatible rich signatures that led to the formation of $SiO_2$ rich rocks. Introduction of various vapor phases (C-H-O-F) into a peridotite facilitate less stability of polymerized phases. Phases such as $CO_2$ and $H_2O$ result in depolymerisation of the melt (Edgar & Vukadinovic, 1992; S. Foley, 1992) by breakage of Si-O bonds forming small networks of aluminosilicates. A fluid phase dominated by $CO_2$ would facilitate the formation of silica poor but $CO_2$ rich phases as opposed to fluids dominated by $H_2O$ where OH-rich phases would predominate (S. F. Foley et al., 1987). In general, the composition of various volatiles species and the nature of the source region determine the final lamprophyre type forms (Edgar & Vukadinovic, 1992)

# Chapter 3

# Methodology

## 3.1 Field work

After a detailed review on the formation of the Møre-Trøndelag Fault zone (MTFZ) as well as hydrothermal activities that led to thorium alteration in veins and breccia (Grønlie &Torsvik, 1989), field work on the Ytterøy island in the northern Trondheimfjord area was implemented. Twelve samples were selected using the Geiger Muller counter, sampled and collected directly from fresh rock surfaces. All samples were submitted to the laboratory for further investigation with help of microscopy, XRD, SEM and ICP-MS and EPMA.

## 3.2 Lab analysis and Software

All samples from the field work were analyzed at NTNU Laboratories, Department of Geosciences and Petroleum Engineering and in Sweden at the ALS Chemex. **ioGAS** and **Andy Tindle Software** were employed to geochemical analyses and calculation of mineral formulas respectively. ioGAS Software uses the analytical data analyzed using either XRF, ICP – MS or EPMA instruments. During the analyses, analytical data are either transformed into figures, plots or any other shapes of interest. Andy Tindle Software also uses analytical data obtained from diverse analytical instruments. The software contains various excel sheets with different minerals such as carbonates, oxides, silicates etc. in which the analytical data are computed into mineral formula.

## 3.3 Sample preparation

The samples were cut into half, one part was submitted to the thin section lab at the Dept. of Geoscience and Petroleum Engineering at NTNU for thin preparation. Polished thin sections were made for all samples (see table 2). At the thin section lab, the sample was cut using a diamond blade to have a sample size for thin section preparation (about 30µm thickness) (Dyar et al., 2008). A portion of each sample was sent to the crushing and grinding lab section at the laboratory. The crusher and hummer were used to reduce the sample size for final grinding using Tungsten Carbide disk mill. During the entire process, cleaning using ethanol and air compressor were employed for every sample being prepared. The final powdered sample was split, weighed and packed for chemical and mineralogical analysis.

## 3.4 Thin section scanning

Twelve thin sections were scanned by using Epson Perfection V600 (J 252A) photo scanner in crossed polarized light (Figure 7) employed with polarizing film. The scanned photo was used as a reference when working on SEM and EPMA instruments.

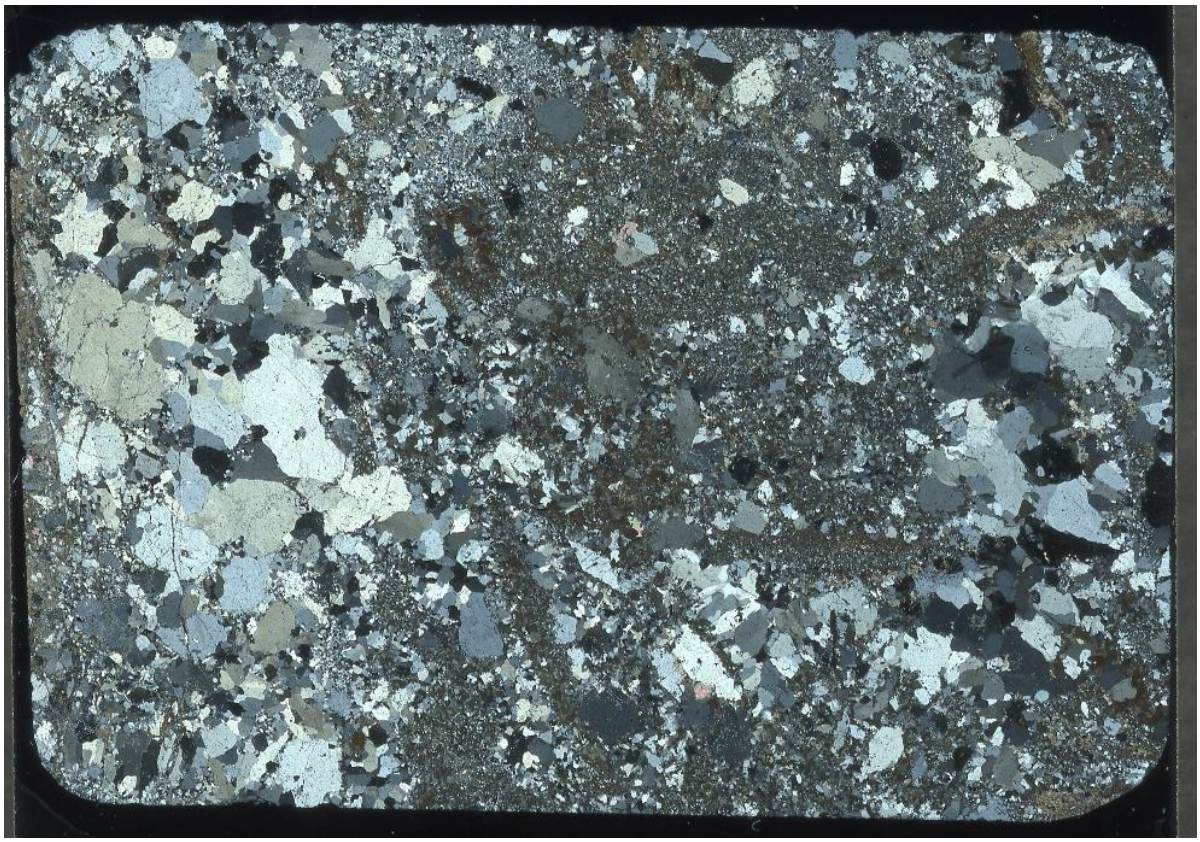

Figure 7. Photo of scanned thin section (AM-16-003B) in a crossed polarized light.

## 3.5 Optical Microscopy

The microscope is installed with two polarizers, lower polarizer and upper analyzer that are normally oriented in a way that their polarization direction is perpendicular to one another (Figure 9). The light from the source is initially unpolarized (Figure 8), when it enters in the lower polarizer it becomes polarized in a right-left direction referred to as east-west direction. The light passes through a hole of a rotatable microscope stage and enters the lower lens. The analyzer normally is oriented perpendicular to the lower polarizer in the south-north direction. If the analyzer is in, then the plane polarized light coming from the lower polarizer will be perpendicular to the analyzer and no light will be transmitted through the ocular lens (www.tulane.edu/~sanelson/eens211). All these properties are used to distinguish minerals

under microscope that have isotropic or anisotropic characteristics. Properties such as color, shape, habit, cleavage, twinning, extinction, birefringence, pleochroism, extinction angle, and interference figure, are also used for both transparent and opaque minerals.

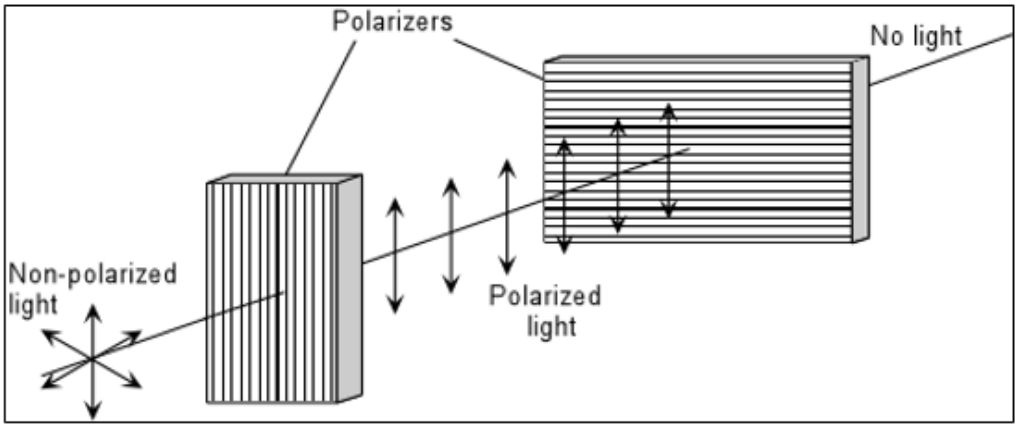


Figure 8. Orientation of polarizer and analyzer (Nelson, 2016).

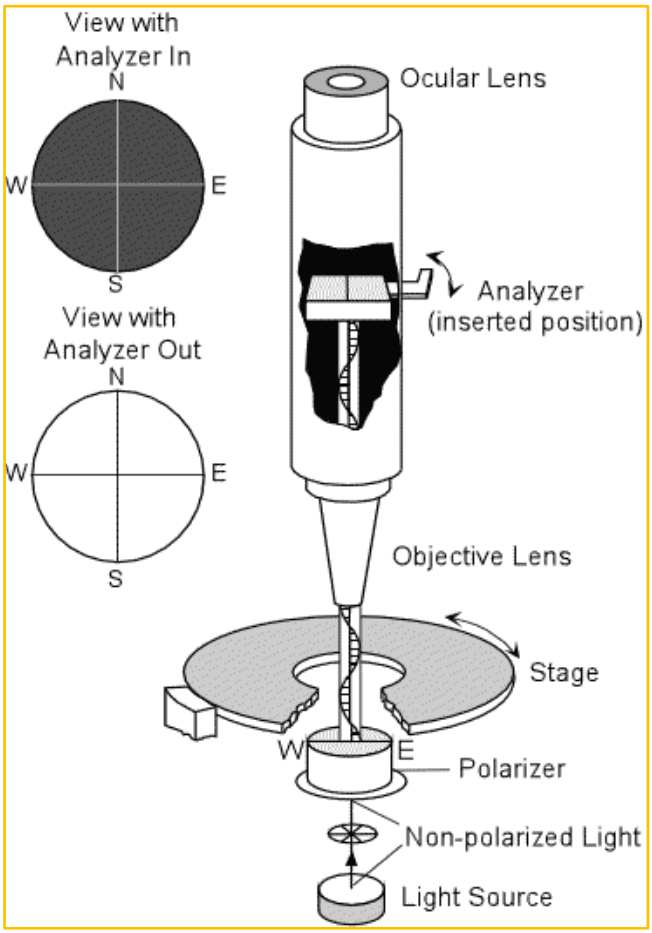


Figure 9. Polarized microscope set-up (Nelson, 2016).

## 3.6 X-ray Difraction (XRD)

An X-Ray Diffractometer (model Diffrac.EVA) with Cu X-ray tube, 1.54056Å, 2Θ = 3°- 65°, acceleration voltage 40 Kv, current 40mA was used to investigate a powdered sample. The quantification was based on TOPAS-Rietveld. The technique is used for mineral identification (i.e. qualitative and quantitative). A fine powdered sample <44 μm with 10-20g is required for analysis. A portion of the powdered material is compacted and mounted in the sample holder and subsequently scanned with an X-ray beam. After, scanning through an angle θ of incident X-ray beam form an angle of diffraction (0° to 90°) which correspond to different d-spacing of atom in the powdered sample (Bragg's Law: $n\lambda = 2d \sin \theta$) (Figure 12).

The X-rays produces different wavelengths, which are characteristic for specific minerals present in the sample. X-rays emitted from the sample are excited and detected with an electronic detector (Figure 10). The goniometer keeps track on the change of the angle θ whilst the detector records the X-rays arriving from the other side of the sample. The informations are sent to the computer for interpretation. After a scan, X-ray intensities are plotted against the angle θ producing spectral lines which correspond to different minerals present in the sample (Figure 12). Mineral composition in the samples are identified automatically using XRD computerized software packages that employ the search-match technique.

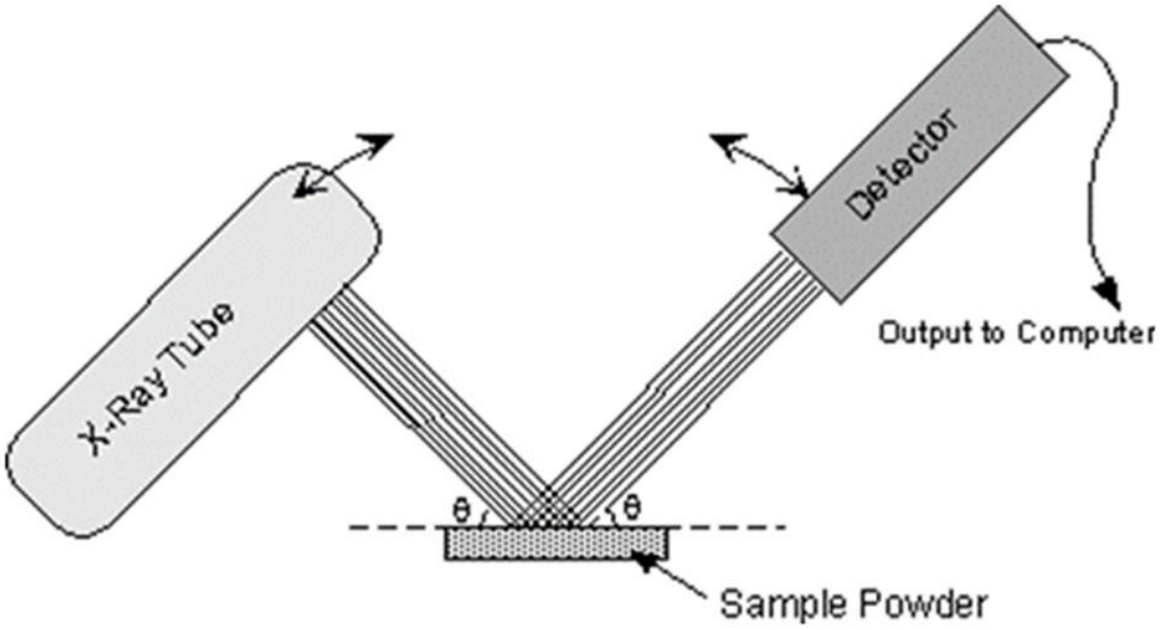


Figure 10. An array of X-ray tube, sample holder and detector (Nelson, 2016).

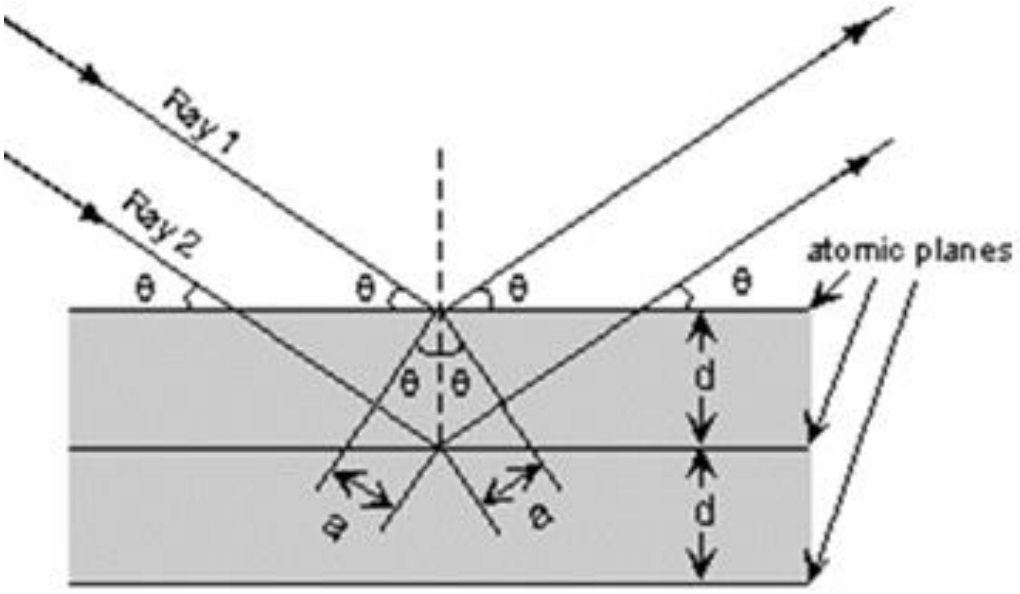


Figure 11. Reflection and diffraction angles produced from a mineral grain surfaces (Nelson, 2016).

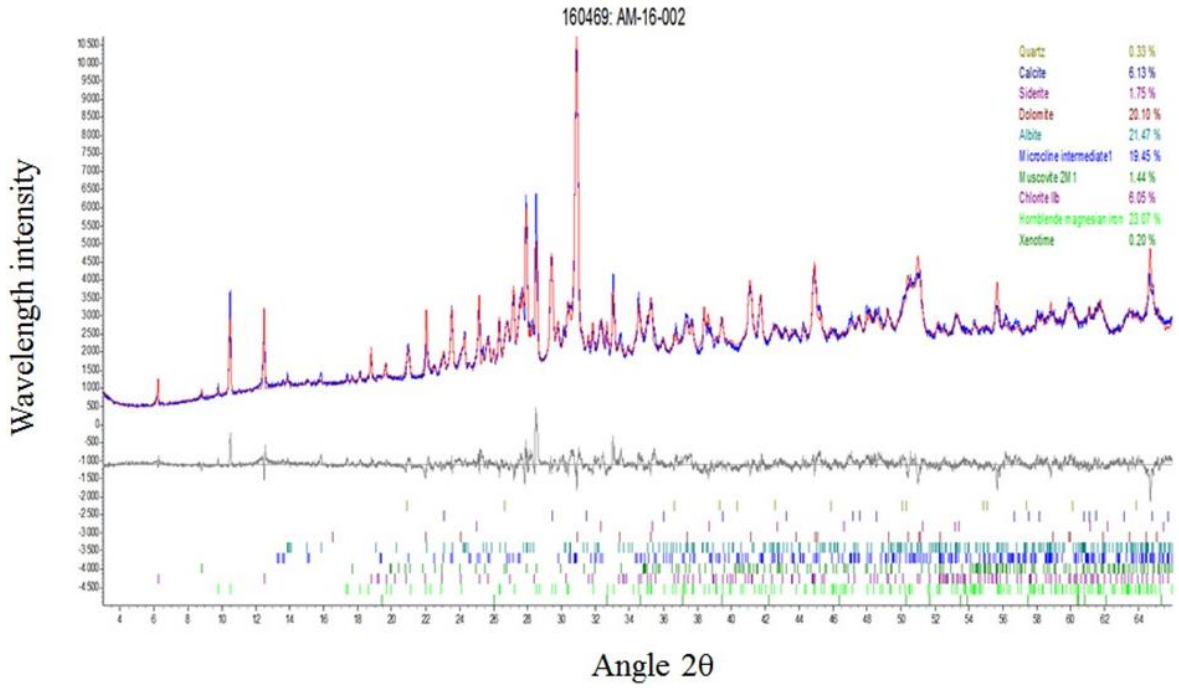


Figure 12. X-Ray intensity VS diffraction angle (2θ).

## 3.7 Scanning Electron Microscope (SEM)

This is applied in mineralogy to analyze polished, thin sections and unmounted mineral grains. The samples were coated with a layer of carbon to prevent charging on its surface. All samples were examined using a Bruker S8. An acceleration voltage of 15 to 20kv and suppressor voltage ~ 300V were set for the electron beam. Also, free movement of a microscope stage and the lens were set at 15mm as a working distance, 3 inches for microscope stage rotation under standard mode and 15X for normal analysis.

SEM produce electrons in high vacuum (~300V) where an electron accelerates from an electron gun and imopacts the sample surface. This results into emission of backscattered electrons (BSE), secondary electrons (SE), X-rays and other X-ray signals (Figure 13a). An individual signal from each mineral is detected using a specific detector such as BSE, SE and EDS being installed with SEM. All these signals have a specific application relative to mineral identification. Minerals are identified by focusing an electron beam on a specific particle/mineral phase where X-rays signals are collected. The detected electrons are converted

into signals, amplified and visualized on a monitor as surface image. This is referred to as Grey level images showing the distribution of minerals in the sample (Petruk, 2000).

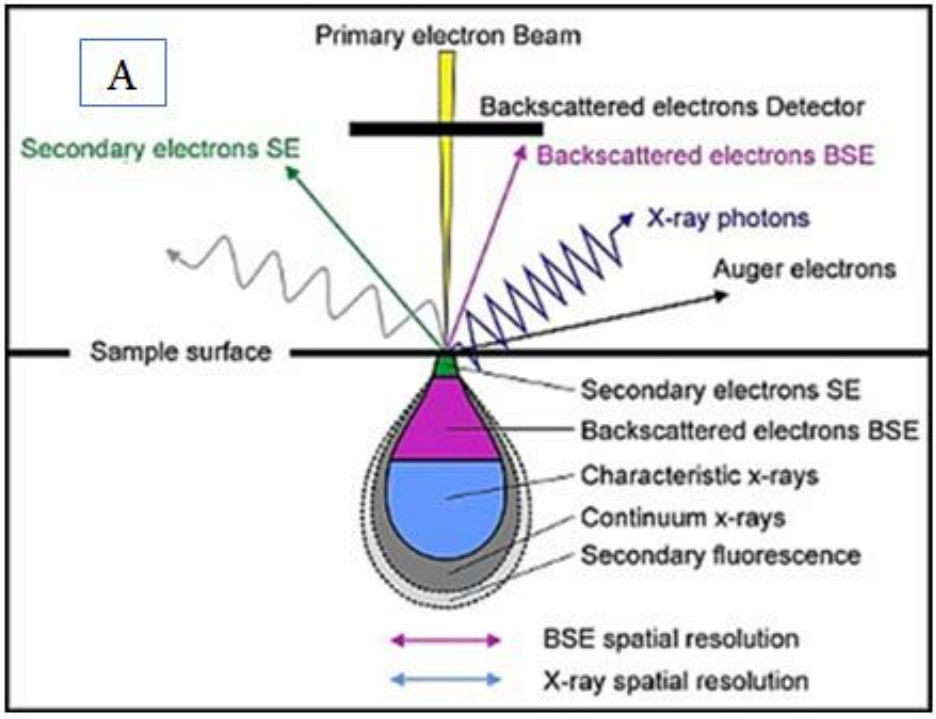


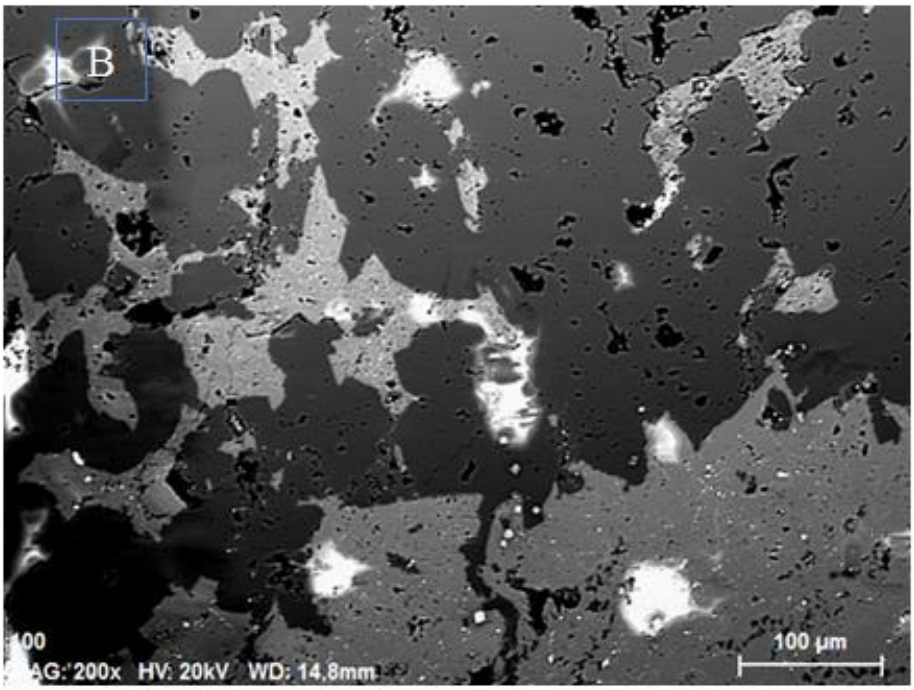


Figure 13. (A) An illustration of SEM and its parts (Heinig, 2017) (B) Backscattered photo detected by using BSE detectors in SEM (Observed form a thin section AM-16-007).

## 3.8 Inductively-Coupled Mass Spectrometry (ICP-MS)

This is an analytical instrument used in elemental determination. It combines inductively coupled plasma (ICP) and mass spectrometry (MS) instruments (Dyar et al., 2008). Both are simultaneously applied during analysis by measuring most elements in the periodic table and determine their concentration down to the part-per-trillion (ppt) level. Samples for analyses were grinded into fine powder (about 40 µm) packed and shipped to the accredited testing laboratories with Reg. No. 173T in Sweden. The powdered rock samples were pulverized, splitted and sieved using a mesh size < 75 µm. Each sieved sample was dissolved in acids to form a solution (aerosol). The aerosols were swept with argon gas into the excitation region of a plasma. The excited electrons emits wavelength that are characteristic of elements present in the sample (Dyar et al., 2008). An installed mass analyzer in the mass spectrometer is used to separate ions based on their atomic/charge ratio. The wavelength intensity of an individual element is generated based on their mass (peak intensity of an element is directly proportional to its initial concentration). The proportionality of the isotopes were determined by using a standard of known concentrations of the element. Several analytical procedures (table 1) were employed prior to chemical analysis.

Table 1.The analytical procedures performed during sample analysis.

| **ALS CODE** | **Description** | **Instrument** |
|---|---|---|
| ME-ICP06 | Whole rock package – ICP-AES | ICP-ASE |
| C-IR07 | Total Carbon (Leco) | LECO |
| S-IR08 | Total Sulfur (Leco) | LECO |
| ME-MS81 | Lithium Borate Fusion ICP-MS | ICP-MS |
| ME-MS42 | Up to 34 elements by IPM-MS | ICP-MS |
| OA-GRA05 | Loss on Ignition at 1000°C | WST-SEQ |
| TOT-ICP06 | Total calculation for ICP06 | ICP-AES |
| ME-4ACD81 | Base Metals by 4-acid digestion | ICP-AES |

## 3.9 Electron Probe Micro Analysis (EPMA)

An electron probe micro analysis (EPMA) uses principals similar to the X-ray Fluorescence (XRF) instrument except that, the former use a beam of electrons to excite the atom from the specimen rather than X-rays employed in the XRF instrument (Dyar et al., 2008). The set-up of the instrument are based on (Petruk, 2000) and (V et al., 1995). Like SEM, it is a microbeam technique that uses Wavelength Dispersive X-ray Spectrometers (WDS) to detect X-ray counts radiated from the sample surface (Petruk, 2000). An instrument is equipped with SE, BSE and EDS detectors for easy and fast mineral identification. The accuracy and precision of all detectors differs relative to elements present in the sample. Major, trace and/or minor elements are detected by using EDS and WDS, respectively. WDS can be used to detect X-ray counts from a sample with few major elements.

Twelve thin sections were analyzed using electron microprobe instrument JEOL (JXA 8500F) with an installed PROBE software. Different standards were used for different minerals under investigation. The electron beam was accelerated from the source and focused down to a spot size of about 1μm on sample surface. The beam of electrons strikes on a sample surface and excite X-rays to a lower state (unstable). When the excited electrons fall back to the ground state, the electrons fluoresce X-rays with wavelengths or energies that are characteristic of the element present in the sample (Dyar et al., 2008). A crystal diffracts X-rays from the sample surface into the detectors at different diffraction angle θ for determination. At least three (3) series of spectrometers are installed in the probe which help to determine more than one element at a time. Like XRF, standards are measured to determine the proportionality constants or calibration curves and equation.

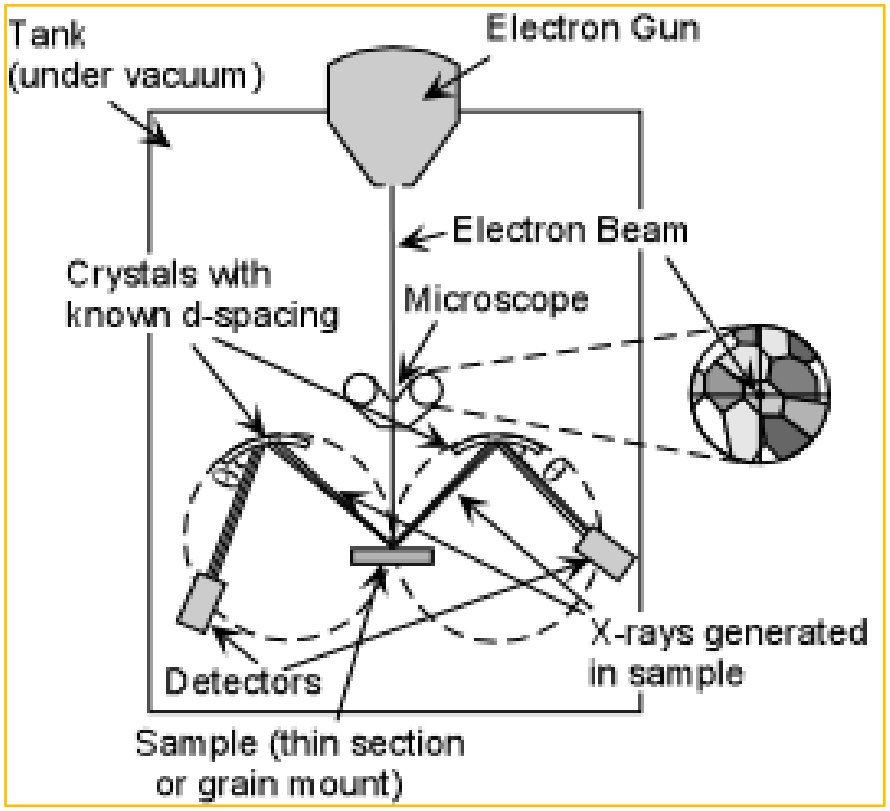


Figure 14. Basic component of Electron Micro Probe analyzer (Nelson, 2016)

# Chapter 4

## Results

Different techniques were employed during the entire process of data collection. Field mapping, Optical microscopy, X-ray Diffractometry (XRD), Scanning Electron Microscope (SEM), Inductively- Coupled Mass Spectrometry (ICP-MS), Electron Probe Micro Analysis (EPMA), **Andy Tindle** and ioGAS Geo-software are techniques employed in this study. Different results were obtained and reported with aid of figures, table and diagrams for a detailed illustration and better understanding.

## 4.1 Sample location

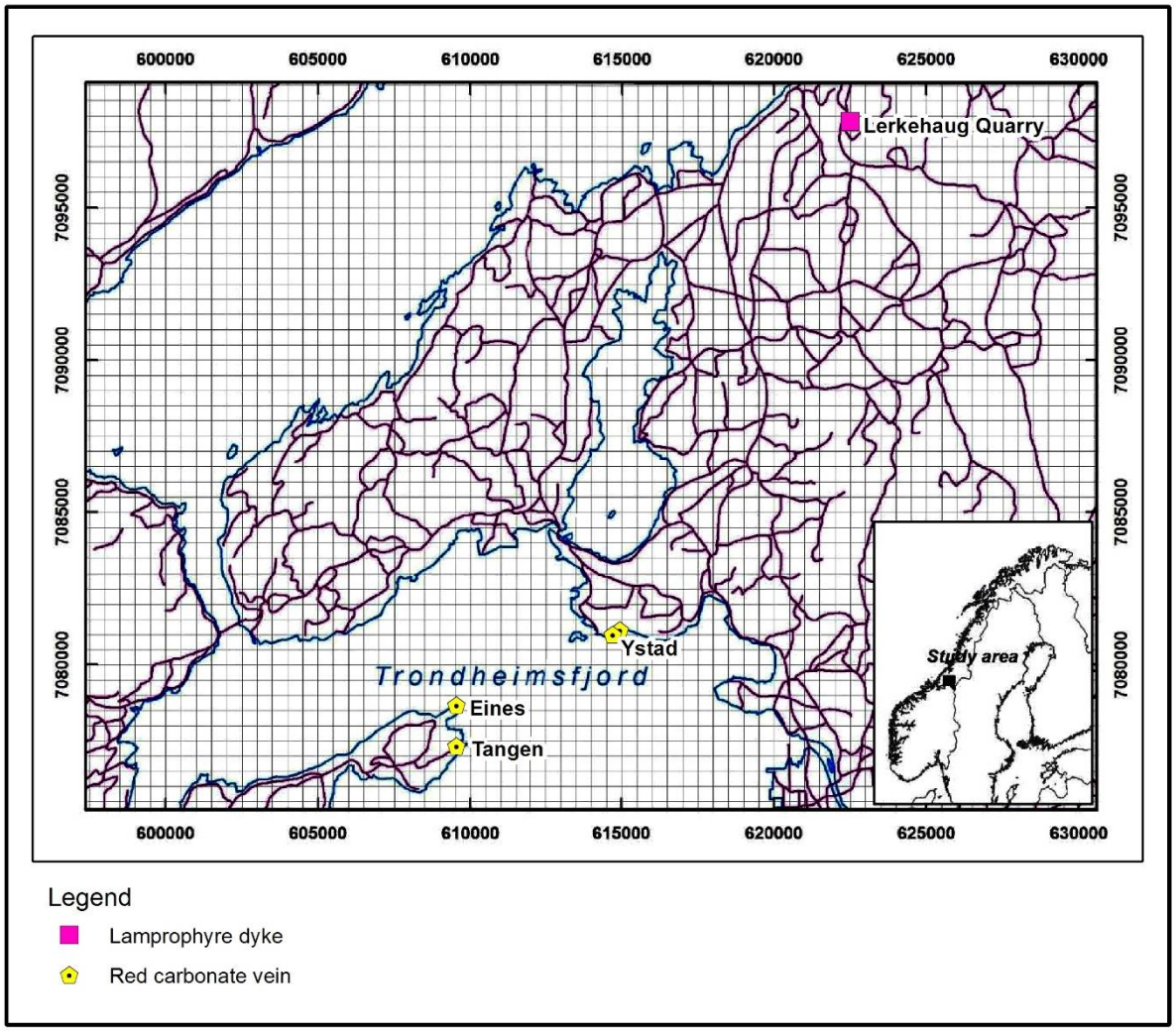


Figure 15. Map showing the sample location

## 4.1.1 Sample description

Table 2. Show sample name, location and its descriptions

| **Sample No.** | **Sample name & Location** | **Description** |
|---|---|---|
| AM-16-001A | Red-carbonate vein | -Fine- to medium-grained rock samples characterized with an alternating red carbonate and quartz veins of variable thickness (1.5 – 12 cm thick). |
| AM-16-001B | 0614926 (E), 7081106 (N) – A & B | -Both samples contain low Th content (0.28 – 0.32 µsv/h) on a Geiger Muller reading. |
| | **Ystad locality** | -Both veins trend in NE-SW with ca. $50^{o}$strike. |
| AM-16-002 | Red-carbonate vein | -Fine grained sample dominated with red carbonate and quartz veins of variable size ranging from 5cm wide. |
| | 0614926 (E), 7081110 (N) | -Contain low Th content (1.05 µsv/h) on a Geiger Muller reading. |
| | **Ystad locality** | |
| AM-16-003A | Red-carbonate vein | -Medium- to coarse-grained rock sample characterized with alternating red carbonate and quartz veins. |
| AM-16-003B | 0614691 (E), 7080968 (N) – A & B | -They have low Th content (0.96 – 1.21 µsv/h) on a Geiger Muller reading. |
| | **Ystad locality** | |
| AM-16-004 | Red-carbonate vein | -Fine-grained sample with red carbonate vein striking $040^{o}$ NE. No Geiger Muller reading was recorded. |
| | 0614691 (E), 7080968 (N) | |
| | **Ystad locality** | |
| AM-16-005 | Lamprophyre dyke | -Fine-grained, greenish to dark in color. |
| | 0622487 (E), 7097822 (N) | - Dominated by fractures (fig.17), which trend toward the NW-SE. No Th content was recorded. |
| | **Lerkehaug quarry locality** | |

| | | |
|---|---|---|
| AM-16-007 | Red-carbonate vein<br>0609555 (E), 7078652 (N)<br>**Eines locality** | -Both samples are medium- to coarse-grained.<br>-They are characterized by red carbonate and quartz veins that trend in the NE – SW<br>-High Th content (4 – 8 µsv/h) was recorded on a Geiger Muller reading |
| AM-16-008 | Red-carbonate vein<br>7078652 N, 0609555E<br>**Eines locality** | |
| AM-16-009 | Red-carbonate vein<br>7077310 N, 609550 E<br>**Tangen locality** | -Fine- to medium-grained rock sample<br>-It has low Th content (1.00 µsv/h) on a Geiger Muller reading |
| AM-16-010A | Red-carbonate vein<br>7077310 N, 609548 E<br>**Tangen locality** | -Medium- to coarse-grained rock sample<br>-Both contains low Th content and Th-rich veins were found positioned at the center of quartz vein. |
| AM-16-010B | | |

## 4.1.2 Description of the study area

The area is dominated by metasediments that originated from volcanic rocks and now occur as greenschists. Ytterøya island (Figure 2) is dense covered by vegatation and fields and most of the outcrops occur only along the shore line (Fig 16 – D). Different veins swarms of variable sizes from 5 to 50 cm dominates the host rock along Ytterøy island. Major dominant veins include quartz and red- carbonate veins (Fig.16 - A, B & C). At Ytterøya Island most of these veins show similar orientation (040° to 220°- strike).

Th radiation was measured in the red-carbonate veins using Geiger Muller as an instrument. Most of the Th-rich veins were observed positioned at the center of quartz vein. Some of these veins at Eidnes locality (Figure 2) show high Geiger Muller readings (i.e. 4 - 8 µsv/h, (0609555 E, 7078652 N) compared to quartz and red-carbonate veins measured at the Ystad locality (0.28 – 1.21 µsv/h, (0614926 E, 7081106 N). Field observation has documented K-feldspar, quartz, fluorite, carbonate and radioactive minerals (as per Geiger Muller readings) as major mineral assemblages in the rocks. In addition, an ultrapotassic Lamprophyre dyke (Fig.17) was found at Lerkehaug quarry (0622487 E, 7097822 N) with NW-SE orientation. (See chapter 2.3 for a detailed explanation.

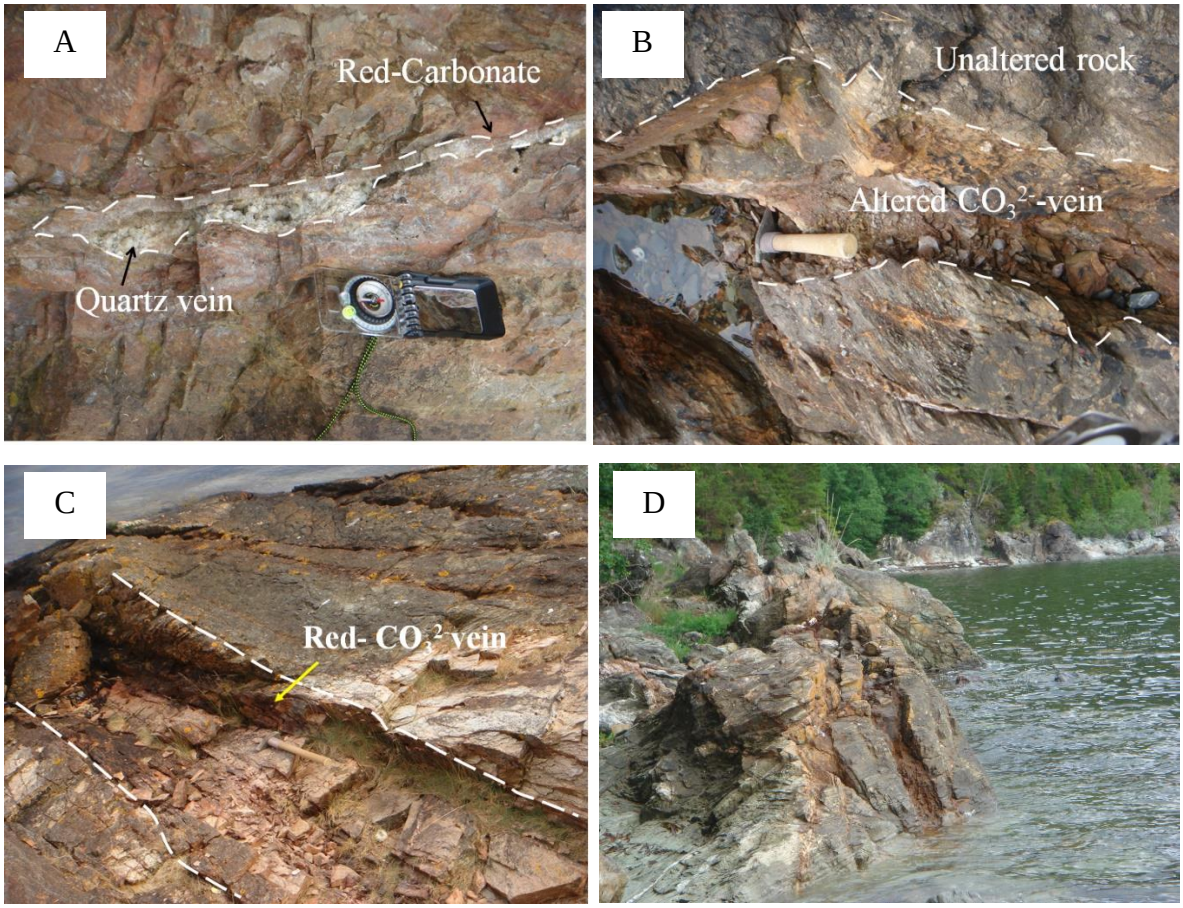


Figure 16. A) Quartz veins alternating with red-carbonate B) Altered red-carbonate vein rich in thorium at Ystand C) Red-carbonate vein rich in thorium at Eidnes at Ytterøy Island D) An overview of red-carbonate veins along the coast.

Figure 17. An overview of Lamprophyre dyke at Lerkehaug quarry locality. The dykes comprises the lineaments going from lower right to upper left corner of image.

## 4.2 Petrographic studies

Various procedures (see Chapter 3 (3.5)) were employed during mineral identification under the microscope. This was done purposely to gather all important petrographic properties for each rock sample.

### 4.2.1 Samples AM-16-001A & B

**Main minerals** : Quartz (20 – 30 %), Calcite (1 – 3 %), Microcline (20 – 30 %), Dolomite (30 – 35 %). **Accessory mineral**: Thorogummite (1 – 3 %), Pyrite > 1%, Fluorite > 1%, Apatite >1%

Medium- to coarse-grained rock mainly dominated by an assemblages of quartz, calcite, microcline and dolomite whilst thorogummite, pyrite and fluorite occur as accessory minerals.

Subhedral to euhedral quartz display dark-grey and colorless under cross- and plane-polarized light microscope respectively. Quartz grain ranges from 2 – 4 mm size and it is sparsely distributed in the sample. Subhedral microcline is observed with undulating twinning displaying pale-dark to pale-yellow anisotropy colours. The mineral grains are sparsely distributed in the rock sample with 2 – 3 mm size. Anhedral dolomite is reddish-brown under cross-polarized light and features a dusty appearance in normal light. The grain-size is 0.02 – 2 mm, sparsely distributed and pervasively altered by quartz and microcline (Fig.18 – B). Calcite is 0.02 mm in size, occur as granular minerals and show twinning lamellas. A fine-grained thorogummite (Fig.18– A&D) with irregular shape display a reddish-brown and dark colors in plane polarized light whilst appear dark in cross-polarized light. It is normally associated with fluorite and apatite (Fig.18 – C).

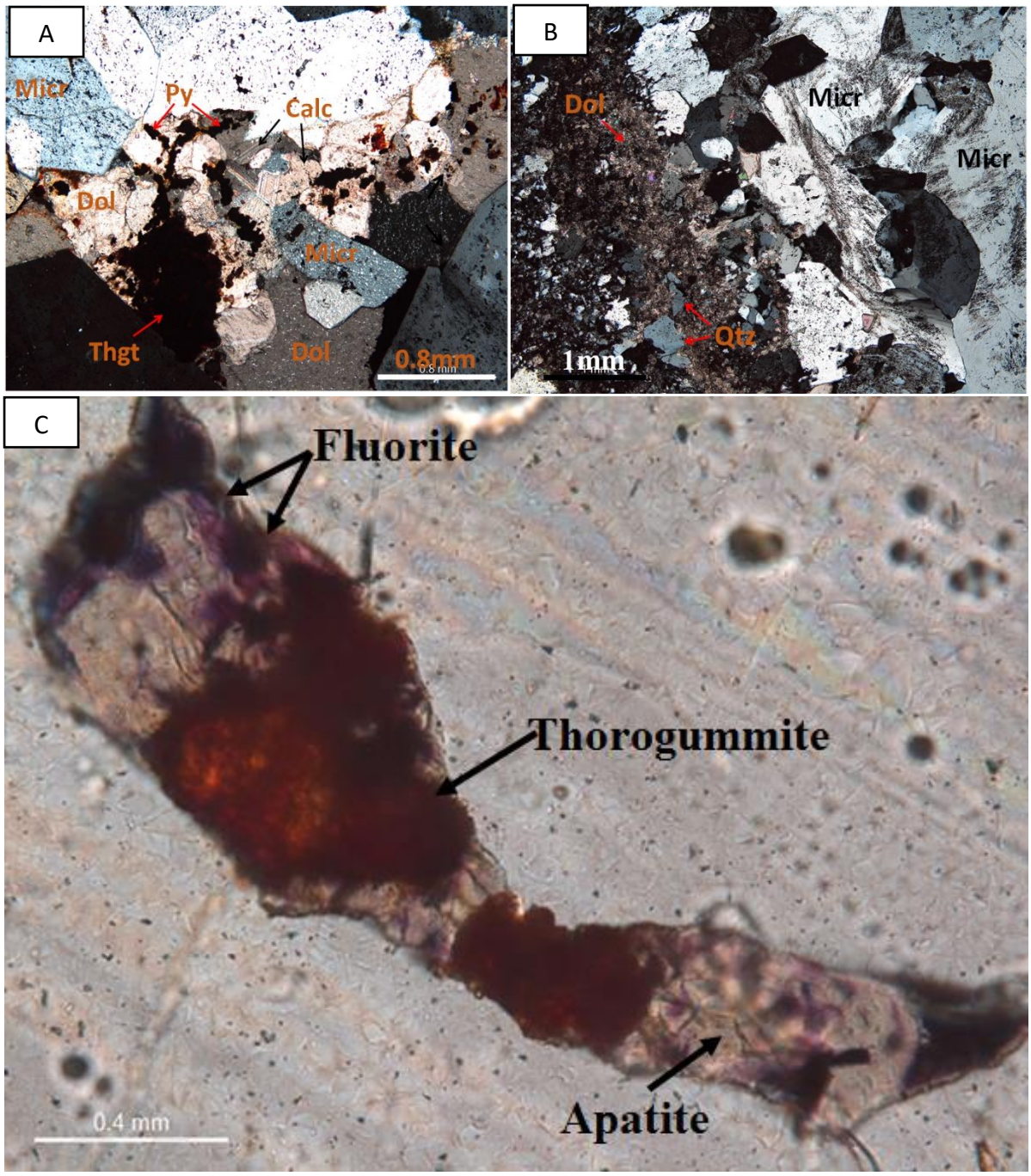


Figure 18. Microphotographs of two rock samples. Both A & B were observed in thin section AM-16-001A, xpl. A) Thorogummite and pyrite replacing the host rock minerals. B) Altered dolomite. C) Thorogummite intergrown with fluorite and apatite, observed in thin section AM-16-001B.

## Samples: AM-16-002

**Main mineral:** Hornblende (20 – 30 %), Quartz (3 – 5 %), Microcline (5 – 10 %) and Dolomite (5 – 10 %). **Accessory mineral:** Pyrite <1 – 2 %, Fluorite <1%, Biotite <1%

Fine-grained red-carbonate vein is mainly dominated by mineral assemblages of hornblende, quartz, microcline and dolomite whilst pyrite and fluorite occur as accessory phases. Hornblende is fine-grained and subhedral with elongated crystals. Hornblende displays a range of colors from pale, dark-yellow-purple on rotation of a microscope stage and appear colorless under plane polarized light. The crystals are 0.02 – 1 mm size and were observed interrgrown with dolomite/ankerite crystals (Fig.19 – A). A fine-grained microcline is 0.02 - 0.04 mm size and occur as an elongated and fractured crystals. Quartz is fine-grained and intersected by dolomite veinlets. Both minerals are fine-grained, 0.5 - 1 mm, sparsely distributed. Fine-grained dolomite were observed and occur in association with quartz. An elongated and irregular crystal of fluorite (Fig.19 – C) occurs as a fine-grained with 0.2 - 0.5 mm size. Pyrite was observed and display a pale-yellow coloration in reflected light.

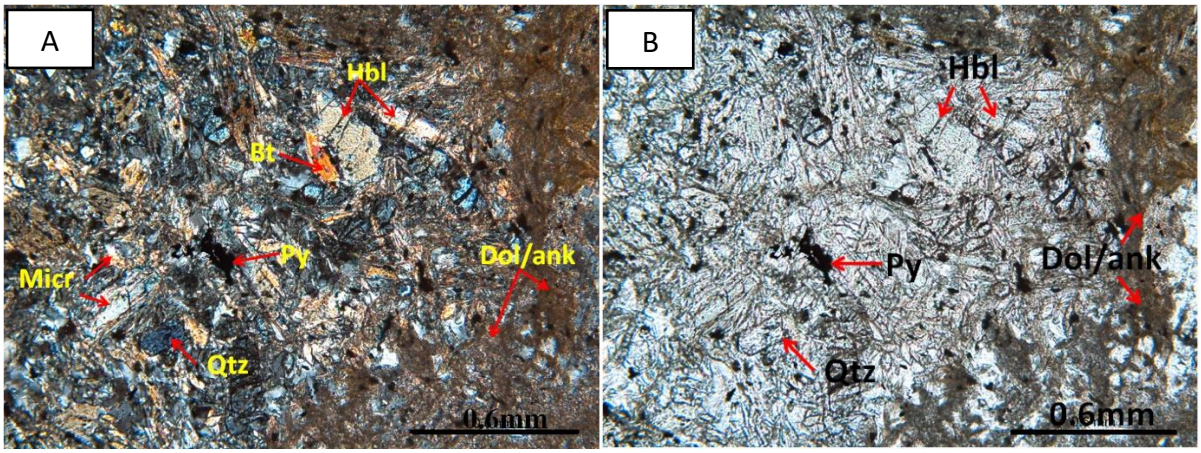

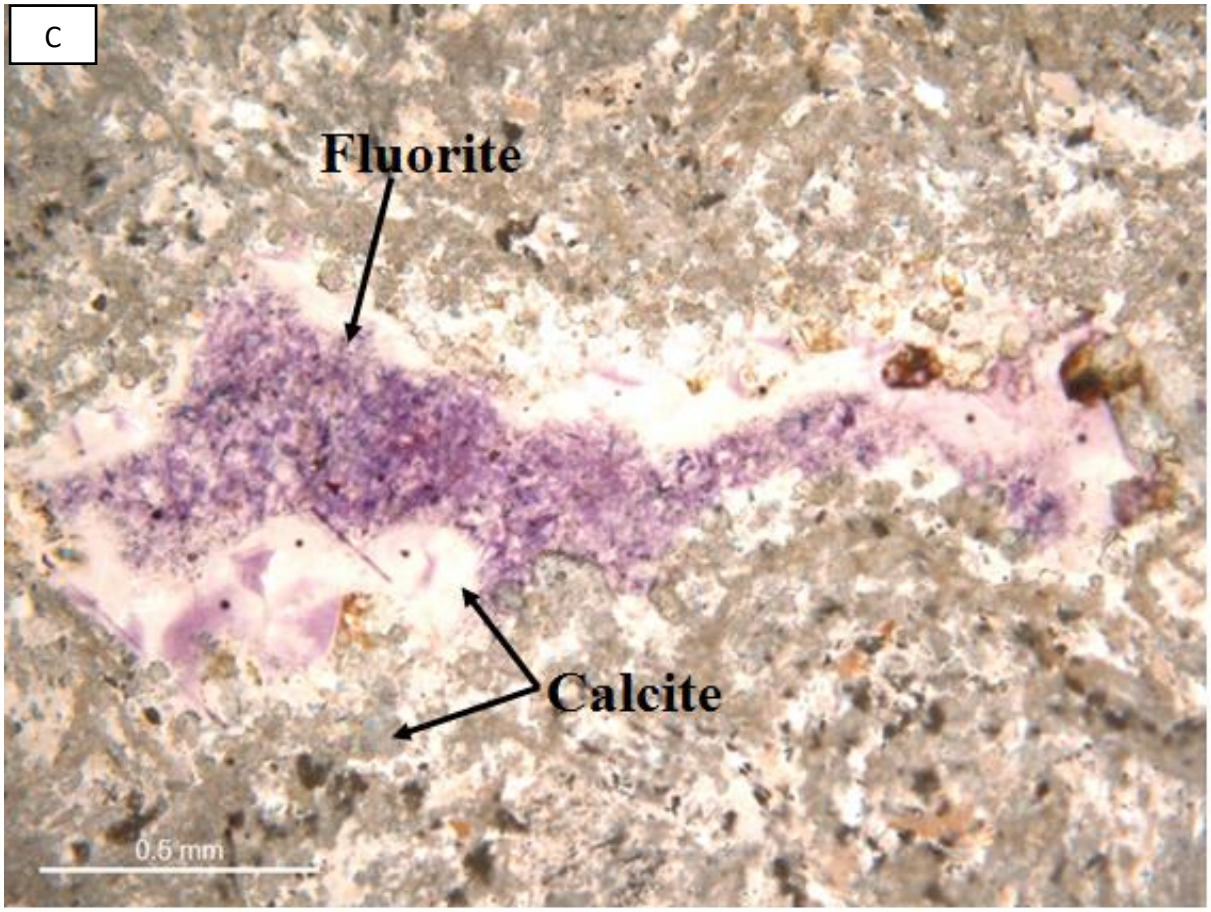


Figure 19. Microphotographs of a rock sample AM-16-002. A&B) Elongated hornblende crystals obscured within dolomite/ankerite, observed on xpl and ppl. C) Irregular crystal of fluorite in association with calcite on a ppl.

## Sample: AM-16-003A & B

**Main minerals:** Microcline (20 – 30 %), Barite (1 – 3 %), Dolomite (3 – 5%), Quartz (35–40%). Medium- to coarse-grained microcline, barite, dolomite and quartz with less/no accessory phases are observed to dominate in the rock sample. Mineral grains of microcline grains are irregular, 0.5-2mm of size, fractured and are densely distributed throughout the rock sample (Fig.20 – A&B). Dolomite occurs as anhedral to subhedral crystal shape with 0.2-1mm size, sparsely distributed and is replaced by microcline and quartz (Fig.20 – A). Coarse-grained and fractured crystals of barite were observed and are normally association with dolomite, quartz and microcline (Fig.20 A – D).

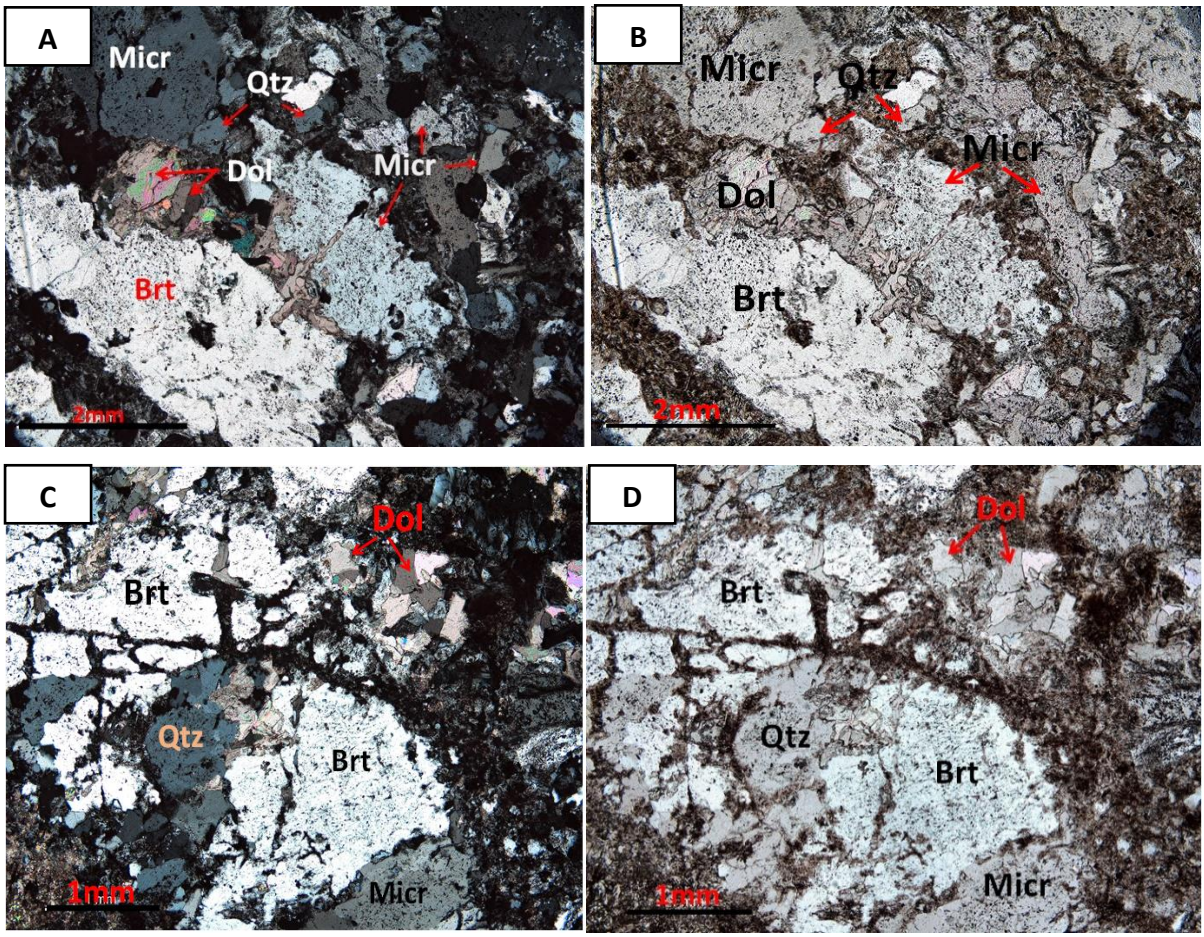


Figure 20. Microphotographs of two rock samples. A&B) Coarse-grained barite in association with other host rock minerals in sample AM-16-003A on a xpl and ppl respectively. C&D) Fractured barite observed in thin section AM-16-003B on a xpl and ppl respectively.

## Sample: AM-16-004

**Main mineral** : Microcline (20 – 30 %), Quartz (30 – 40 %), Dolomite (0 – 5 %), Calcite (1 – 3 %), Barite (0 – 5 %).

**Accessory mineral**: Opaque (Pyrite, <1%)

A fine- to medium-grained red carbonate vein is mainly dominated by mineral assemblages of microcline, quartz, dolomite, calcite and barite whilst pyrite occurs as an accessory phases. Anhedral to subhedral microcline is sparsely distributed in the rock sample with 0.5 – 2 mm size and occur in association with dolomite, quartz and calcite (Fig.21– A&C). Subhedral quartz grains is 0.02 - 0.06 mm size and has a distinctive boundary between neighbouring mineral phases. Dolomite is present in the rock sample with an euhedral shape with 0.02-0.04 mm size. The grain boundaries are replaced by microcline though they form a clear crystal

shape when are in association with quartz. Calcite is present in small quantity and display parallel cleavages, rhombohedral shape and clear crystal with 0.25mm size (Fig.21– C&D). Barite is fine - grained, 0.02-0.05mm size and occur in small quantity with an elongated crystal shape.

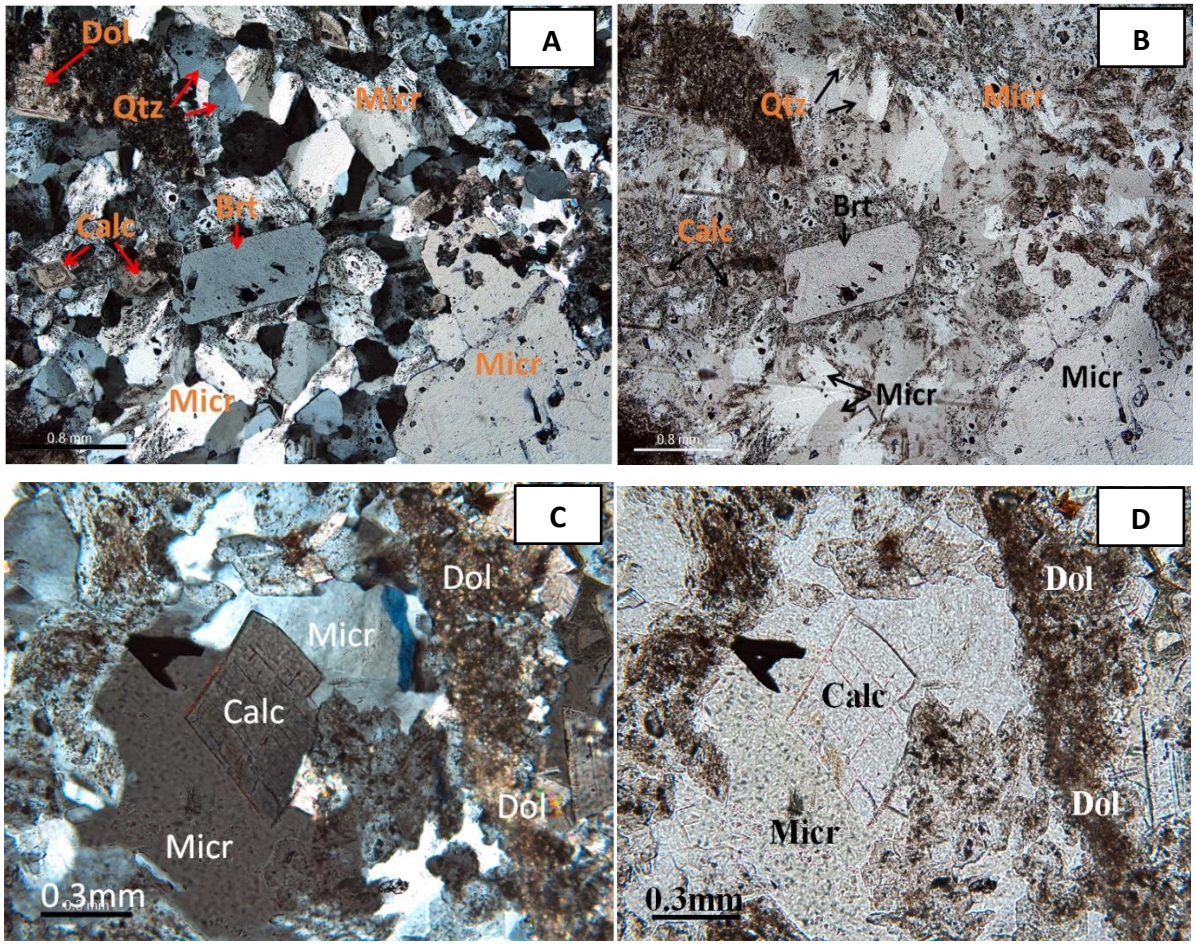


Figure 21. Microphotographs of a rock sample. A&B) Elongated crystal of barite observed on xpl and ppl respectively. C&D) Calcite with a rhombohedral crystal shape, observed on xpl and ppl respectively.

## Sample: AM-16-005

**Main mineral**: Hornblende (40 – 50 %), Epidote (10 – 15 %), Microcline (5 – 10 %)

**Accessory mineral**: Pyrite/pyrrhotite (<1%), Titanite (<1%), Biotite (<1%), Calcite (<1%).

A fine-grained lamprophyre dyke is mainly dominated by mineral assemblages of hornblende, epidote and microcline whilst pyrite, titanite, biotite and calcite occur as accessory minerals

(Fig.22- A – D). Fractured, altered and elongated crystals of hornblende are densely distributed in the sample (Fig.22- A&B). Hornblende were observed enclosing epidote crystal forming a rounded shape. The grains vary between 0.02-0.06 mm size and are normally associated with biotite, epidote, microcline and titanite (Fig.22 - A&C). Subhedral to euhedral mineral grain of epidote is present and occurs as a fine-grained and rounded with a distinct grain boundaries (Fig.22- C&D). Mineral grains vary between 0.02-0.06mm size and are sparsely distributed in the sample. Microcline is present and occur as anhedral to subhedral crystal shape with 0.03mm size (Fig.22 C). Anhedral to subhedral calcite grains are present and are characterized with twinning lamella. The grains boundaries are altered by the neighboring mineral biotite and hornblende (Fig.22 A). Mineral grains are relatively small with an approximate 0.02mm size and are limited distributed in the sample. Titanite is observed as an accessory mineral in the sample. The mineral exhibit pale-brownish to dark colors on rotation under crossed polars. It is anhedral to subhedral crystal shape with grains that vary between 0.01-0.02mm size (Fig.22 A). Biotite and pyrite are present as accessory mineral, limited distributed and display brownish and dark coloration under crossed polars respectively.

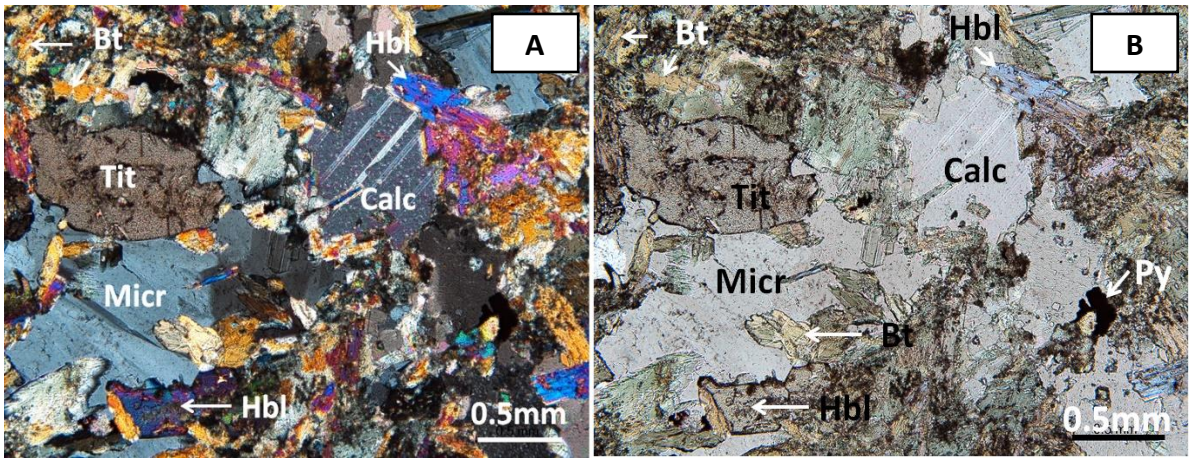

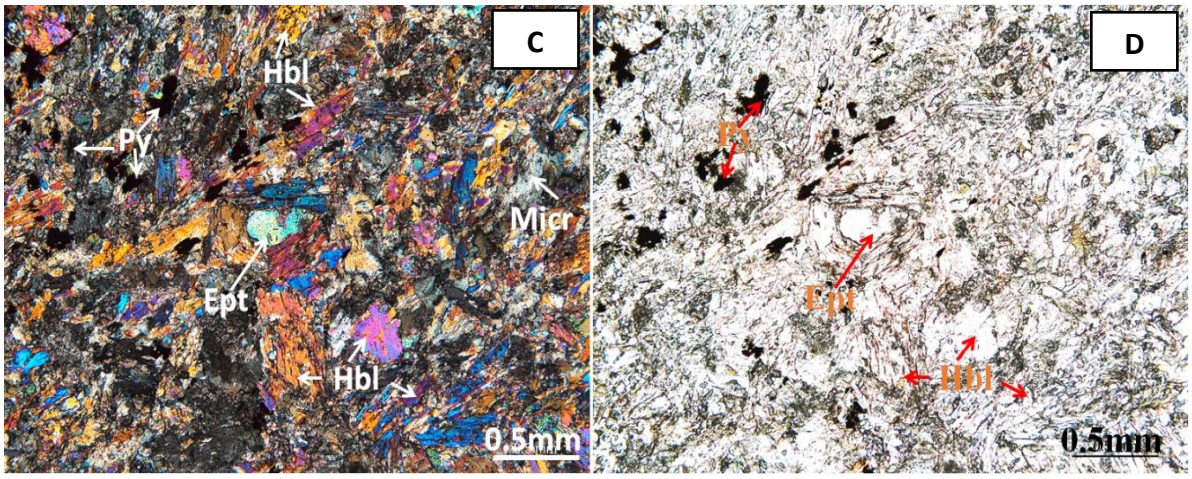


Figure 22. Microphotographs of a rock sample (Lamprophyre dyke). A&B) Altered calcite and titanite observed on a xpl and ppl. C&D) Elongated hornblende enclosing epidote, both observed on a xpl and ppl.

## Sample: AM-16-007

**Main mineral**: Quartz (40 – 50 %), Carbonates (15 – 20 %), Microcline (30 – 40 %)

Medium to coarse-grained red carbonate vein is mainly dominated by mineral assemblages of microcline, quartz and carbonate (dolomite and ankerite) with no observed accessory phases (Fig.23- A&B). Microcline occur as anhedral to subhedral crystal shape, the grains are 0.1-2mm of size, defined crystal boundary and are sparsely distributed in the sample. Quartz is present and occur as subhedral and euhedral crystal shape (Fig.23-A). The grains are sparsely distributed and have variable size ranging from 0.2-0.5mm. Carbonate (dolomite and ankerite) are difficult to distinguish, however, both lacks twinning lamella a common characteristic of calcite (Fig.23-A&B). Dolomite mineral grains are fine-grained (0.02-0.06mm), sparsely distributed and are replaced by quartz and microcline in the sample.

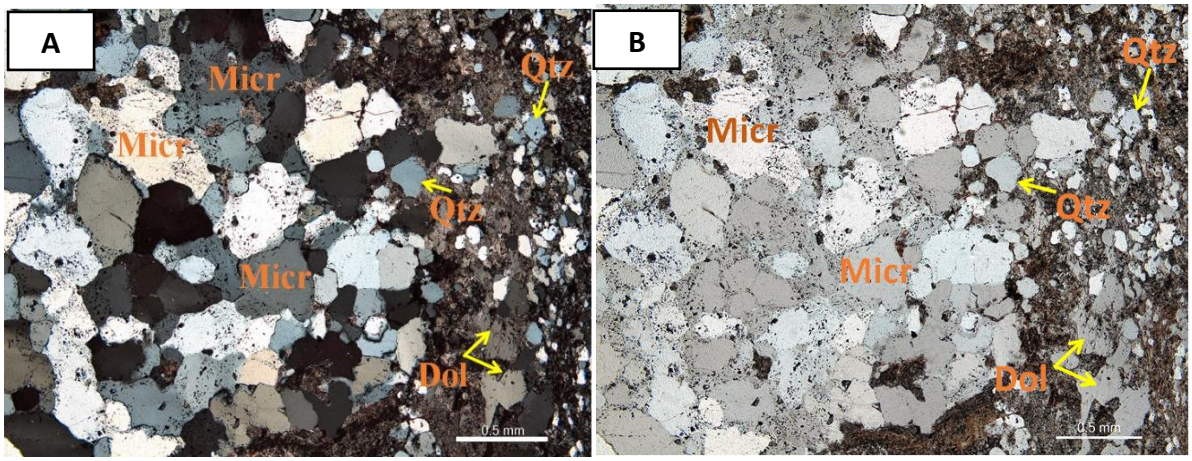


Figure 23. Microphotographs of a rock sample. A&B) Mineral assemblages within a rock sample observed on a xpl and ppl.

## Sample: AM-16-008

**Main minerals**: Microcline (30 – 40 %), Quartz (40 – 45 %), Carbonate (dolomite/ankerite) (10 – 20 %). Accessory minerals: Pyrite (1 – 2 %), Thorogummite (<1%)

The sample is mainly dominated by mineral assemblages of microcline, quartz, carbonate (dolomite & ankerite) whilst pyrite and thorogummite occurs as accessory phases (Fig.24 A-C). Microcline occur as anhedral to subhedral crystal shape and is densely distributed with 0.2-0.5mm in size (Fig.24 A&B). Quartz occur as subhedral crystal shape with grains that vary between 0.2-0.5mm size, however, they are intergrown with thorogummite crystals (Fig.24 C). Anhedral carbonates (dolomite and ankerite) contains grains that vary between 0.02-0.5mm size, limited distributed and are continuously replaced by microcline and quartz. Anhedral pyrite occurs as accessory phase with grains of about 0.5mm size and is limited distributed in the sample. Anhedral thorogummite is also present, 0.5 – 0.6 mm size and sparsely distributed in the sample where replaces carbonates and microcline.

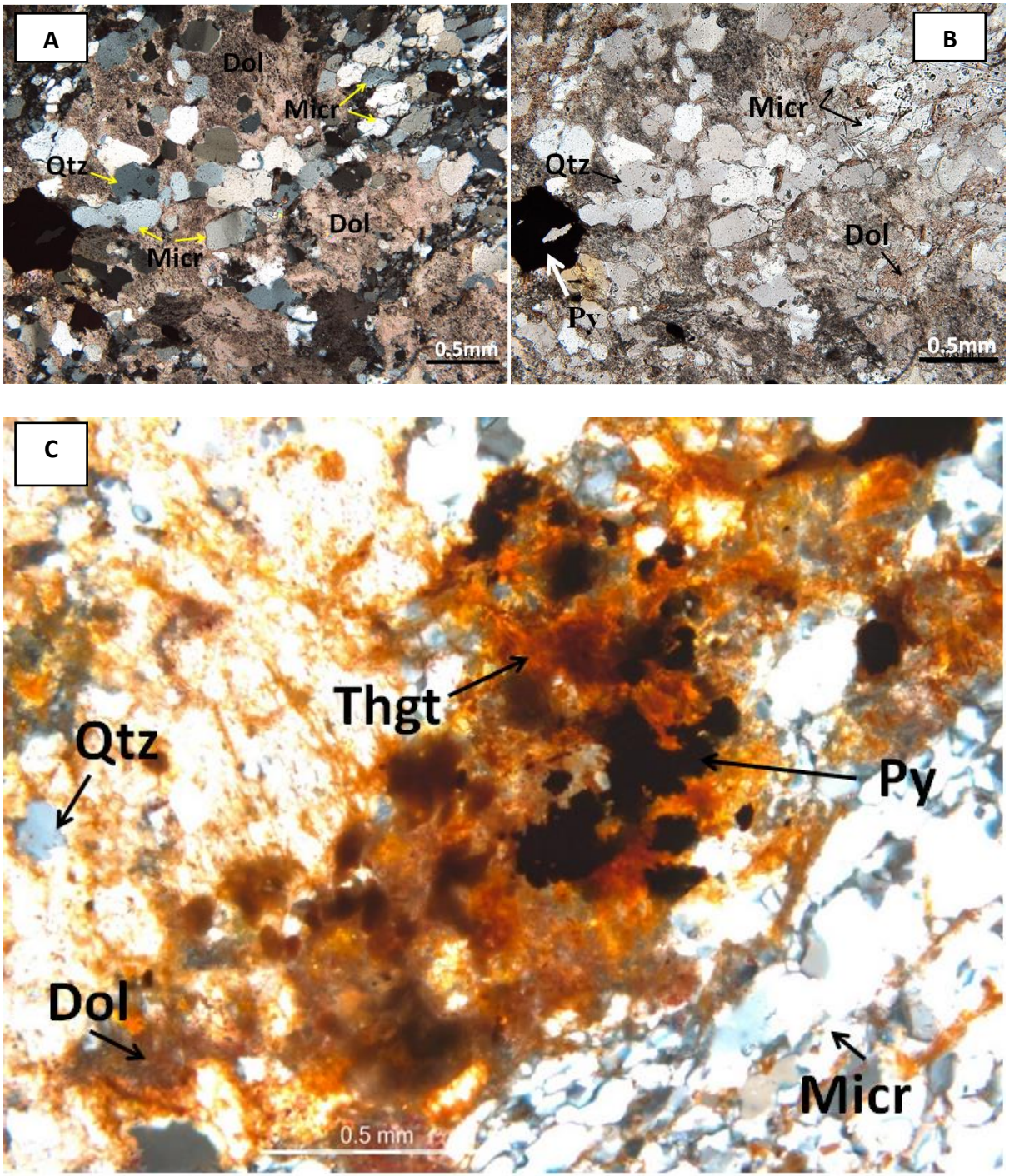


Figure 24. Microphotographs of rock sample. A&B) Mineral assemblages in the sample observed on xpl and ppl. C) Thorogummite intergrown with quartz, microcline, pyrite and dolomite in ppl.

## Sample: AM-16-009

**Main minerals**: Microcline (10 – 20 %), Quartz (5 – 10 %), Carbonate (Dolomite-ankerite) (30 – 40 %). **Accessory minerals**: Barite <1%, Pyrite <1%, Thorogummite <1%.

A fine- to medium-grained red carbonate vein is mainly dominated by mineral assemblages of microcline, quartz, and dolomite. Microcline occur as subhedral crystal shape, sparsely distributed with mineral grains that vary between 0.2-0.4mm size. Carbonate (dolomite-ankerite**)** are present and exhibit anhedral crystal shape that varies between 0.02-0.8mm size. A fine-grained quartz with 0.02-0.06mm of size occur as subhedral crystal and is limited distributed in the samples (Fig.25 A&B).

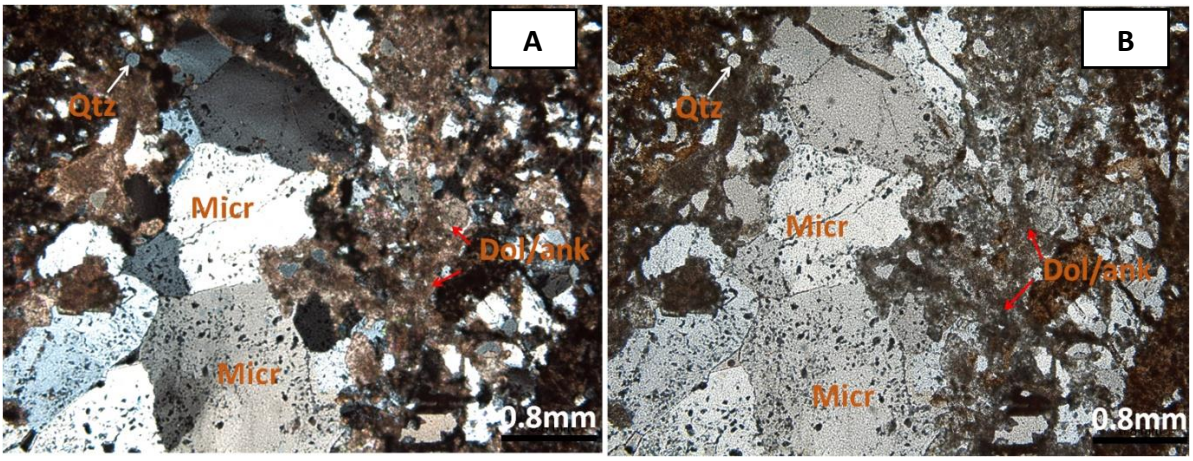


Figure 25. Microphotographs of rock sample. A&B) Mineral assemblages observed on a xpl and ppl respectively.

## Sample: AM-16-010A & B

**Main minerals**: Microcline (25 – 30 %), Quartz (10 – 15 %), Dolomite-ankerite (30 – 40 %)

**Accessory minerals**: Barite <1% and Pyrite >1%

Medium- to coarse-grained red-carbonate is mainly dominated by mineral assemblage of microcline, quartz and dolomite-ankerite whilst barite and pyrite occur as accessory phases (Fig.26 A&B). Microcline occur as anhedral crystals, 0.5-2mm size and is sparsely distributed in the sample. Microcline were observed commonly replacing carbonate minerals. Subhedral quartz were observed with mineral grains that vary between 0.02-0.06mm size, limited

distributed and exhibit minor fractures on its surface. Dolomite-ankerite occurs as anhedral to subhedral with 0.02-0.6mm size and exhibit shades of green, pink and yellow (Fig.26 A). Barite is present as accessory phase, 0.2-0.5mm size, fractured and is limited distributed in the sample. Both pyrite and thorogummite occur as accessory phases.

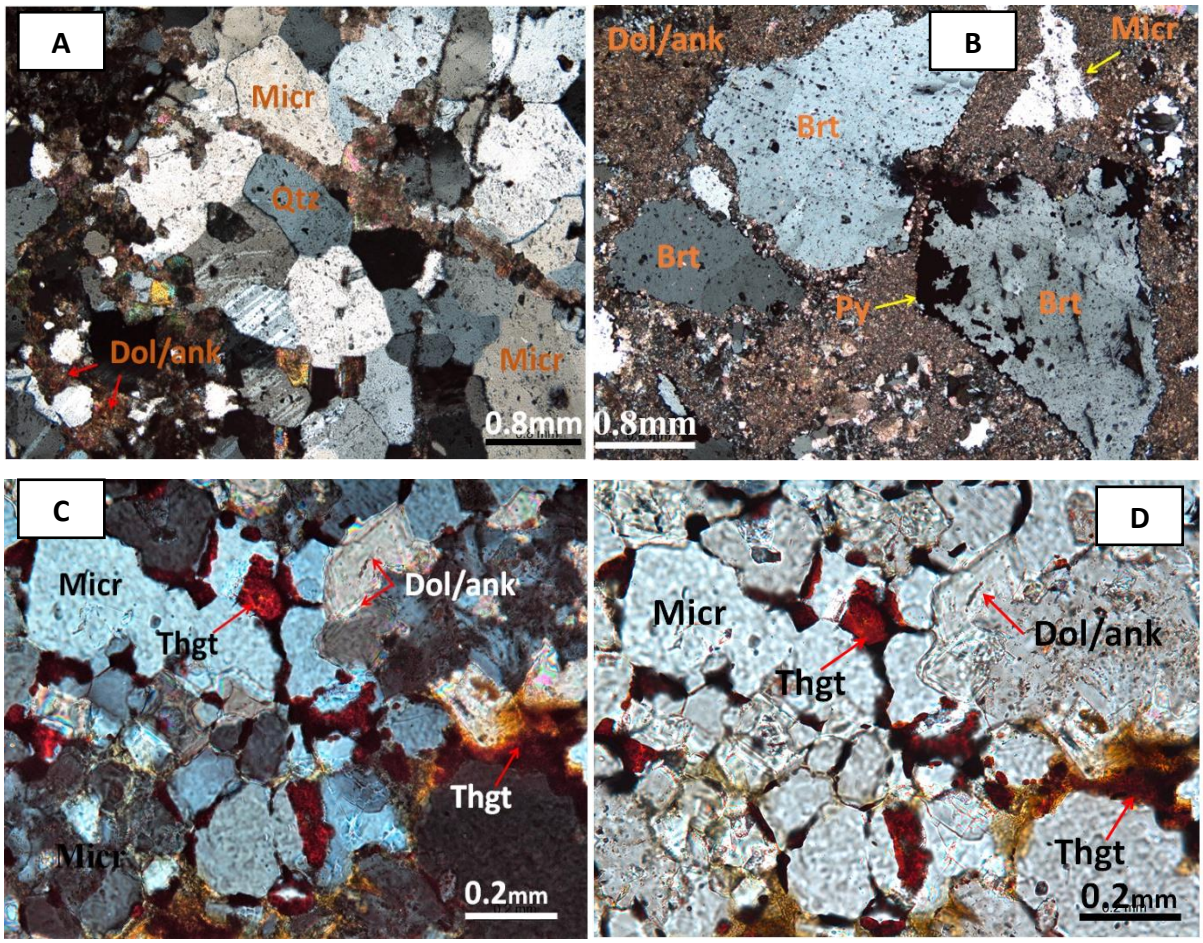


Figure 26. Microphotographs of rock samples. A) Barite crystal surrounded with pyrite and dolomite minerals on a ppl. B) Fine-grained dolomite replaced by microcline and quartz observed on a xpl. C&D) Thorogummite (reddish-brown) in association with other mineral

## 4.3 X-ray Diffraction (XRD)

A powdered and compacted sample were analyzed using X-Ray Diffractometry instrument with an aim of identifying mineral characteristics in the samples (i.e. qualitative and quantitative) (see a detailed illustration of XRD in Chapter 3).

The composition of each sample was determined and measured in weight percent (wt%). The results of each sample are reported by using figures.

## 4.2.1 Sample: AM-16-001A

X-ray wavelengths produced from the powdered rock sample indicate the dominance of dolomite, K-feldspar (Microcline), fluorite and quartz minerals whilst calcite occurs in lesser amounts (Table 3).

Table 3. Mineral composition in the rock sample AM-16-001A

| **Mineral name** | **Mineral proportion** |
|---|---|
| Quartz | 29.81% |
| Calcite | 0.68% |
| Dolomite | 35.17% |
| Microcline Intermediate | 31.94% |
| Fluorite | 2.40% |
| **Total** | **100** |

## 4.2.2 Sample: AM-16-001B

The detected X-rays from a powdered rock sample show quartz, dolomite, and microcline as a dominant mineral phase whilst fluorite and calcite occur in trace amount (Table 4).

Table 4. Mineral proportions in the rock sample AM-16-001B

| **Mineral name** | **Mineral proportion** |
|---|---|
| Quartz | 38.90% |
| Calcite | 0.39% |
| Dolomite | 30.36% |
| Microcline Intermediate | 29.48% |
| Fluorite | 0.87% |
| **Total** | **100** |

## 4.2.3 Sample: AM-16-002

The detected X-rays from a powdered rock sample show the dominance of hornblende (Mg, Fe), Na-feldspar (Albite), microcline, calcite, siderite, and chlorite minerals whilst quartz and xenotime occur in trace amount (Table 5).

Table 5. Mineral proportions in the rock sample AM-16-002

| **Mineral name** | **Mineral proportion** |
|---|---|
| Quartz | 0.33% |
| Calcite | 6.13% |
| Siderite | 1.75% |
| Dolomite | 20.10% |
| Albite | 21.47% |
| Microcline Intermediate | 19.45% |
| Muscovite 2M 1 | 1.44% |
| Chlorite IIb | 6.05% |
| Hornblende Mg-Fe | 23.07% |
| Xenotime | 0.2% |
| **Total** | **99.99** |

## 4.2.4 Sample: AM-16-003A

The X-rays emitted from the surface of powdered rock sample indicate dominance of quartz, microcline, ankerite, diopside, dolomite and barite minerals while xenotime occurs in a small amount (Table 6).

Table 6. Mineral proportions in the rock sample AM-16-003A

| **Mineral name** | **Mineral proportion** |
|---|---|
| Quartz | 46.29% |
| Microcline Intermediate | 31.48% |
| Dolomite | 2.18% |
| Diopside | 5.05% |
| Ankerite Fe0.7 | 10.08% |
| Xenotime | 0.89% |
| Barite | 4.03% |
| **Total** | **100** |

## 4.2.5 Sample AM-16-003B

X-rays emitted from the surface of a powdered rock sample indicated the dominance of quartz, K-feldspar (microcline), ankerite, barite, diopside and dolomite minerals. Xenotime occur in trace amount in the sample (Table 7).

Table 7. Mineral proportions in the rock sample AM-16-003B

| **Mineral name** | **Mineral proportion** |
|---|---|
| Quartz | 63.70% |
| Microcline Intermediate | 18.19% |
| Dolomite | 3.15% |
| Diopside | 3.37% |
| Ankerite Fe0.7 | 7.98% |
| Xenotime | 0.04% |
| Barite | 3.57% |
| **Total** | **100** |

## 4.2.6 Sample AM-16-004

X-rays emitted from the surface of a powdered rock sample indicated the dominance of quartz, microcline, ankerite, dolomite, barite and calcite whereas xenotime and pyrite occur as minor mineral phases in the sample (Table 8).

Table 8. Mineral proportions in the rock sample AM-16-004

| **Mineral name** | **Mineral propotion** |
|---|---|
| Quartz | 43.70% |
| Calcite | 4.89% |
| Pyrite | 0.23% |
| Microcline maximum | 26.90% |
| Dolomite | 2.77% |
| Diopside | 4.12% |
| Ankerite Fe0.7 | 11.67% |
| Xenotime | 0.98% |
| Barite | 4.77% |
| **Total** | **100.03** |

## 4.2.7 Sample AM-16-005

The X-rays emitted from a powdered rock sample show high contents of hornblende, epidote, chlorite, microcline, calcite, diopside and muscovite minerals whereas pyrrhotite occurs in trace amount (Table 9).

Table 9. Mineral proportions in the rock sample AM-16-005

| **Mineral name** | **Mineral proportion** |
|---|---|
| Calcite | 1.84% |
| Microcline maximum | 7.48% |
| Diopside | 4.02% |
| Muscovite 2M 1 | 2.35% |
| Epidote | 18.27% |
| Pyrrhotite 3T | 0.54% |
| Chlorite IIb | 8.98% |
| Hornblende RoundRobin | 56.53% |
| **Total** | **100.01** |

## 4.2.8 Sample: AM-16-007

X-ray spectrum from micronized rock sample showing quartz, microcline, albite (Na-feldspar), ankerite and diopside as major minerals with accessory Mica (Muscovite) (Table 11).

Table 10. Mineral proportions in the rock sample AM-16-007

| **Mineral name** | **Mineral proportions** |
|---|---|
| Quartz | 53.51% |
| Albite | 19.82% |
| Microcline Maximum | 18.96% |
| Diopside | 3.29% |
| Muscovite 2M 1 | 0.37% |
| Ankerite Fe0.7 | 4.05% |
| **Total** | **100** |

## 4.2.9 Sample: AM-16-008

The sample is dominated by quartz, ankerite, microcline and diopside whilst albite occurs in less amount (Table 11).

Table 11. Mineral proportions in the rock sample AM-16-008

| **Mineral name** | **Mineral proportion** |
|---|---|
| Quartz | 51.28% |
| Albite | 2.22% |
| Microcline Maximum | 16.08% |
| Diopside | 3.30% |
| Ankerite Fe0.7 | 27.13% |
| **Total** | **100.01** |

## 4.2.10 Sample AM-16-009

The sample is dominated by ankerite, microcline, and quartz. Minerals such as diopside, barite and albite occur in smaller amounts (Table 12).

Table 12. Mineral proportions in the rock sample AM-16-009

| **Mineral name** | **Mineral proportion** |
|---|---|
| Quartz | 20.04% |
| Albite | 2.09% |
| Microcline Maximum | 26.32% |
| Diopside | 2.59% |
| Ankerite Fe0.7 | 46.53% |
| Barite | 2.42% |
| Total | **99.99** |

## 4.2.11 Sample: AM-16-010A

The sample is dominated by microcline, ankerite, quartz, barite and diopside (Table 13).

Table 13. Mineral proportions in the rock sample AM-16-010A

| **Mineral name** | **Mineral proportions** |
|---|---|
| Quartz | 17.14% |
| Diopside | 2.39% |
| Microcline Maximum | 41.68% |
| Ankerite Fe0.7 | 34.19% |
| Barite | 4.59% |
| Total | **99.99** |

## 4.2.12 Sample: AM-16-010B

The sample is dominated by microcline, ankerite, quartz and barite while diopside is accessory (Table 14).

Table 14. Mineral proportions in the rock sample AM-16-010B

| **Mineral name** | **Mineral proportions** |
|---|---|
| Quartz | 26.80% |
| Diopside | 2.25% |
| Microcline Maximum | 33.94% |
| Ankerite Fe0.7 | 27.80% |
| Barite | 9.20% |
| Total | **99.99%** |

# 4.4 Scanning Electron Microscope (SEM)

Under SEM, different mineral phases in each rock sample were investigated by analyzing several thin sections. The results are presented with an aid of figures for better illustration.

## 4.4.1 Sample: AM-16-001A & B

The sample is dominated by a mineral assemblages of dolomite, microcline and quartz whilst thorogummite, pyrite, apatite, fluorite and barite occur as accessory phases (Fig. 27). Thorogummite and barite occur by replacing the microcline, quartz, dolomite and calcite (Fig. 27. A – D). Thorogummite is always associated with pyrite (Fig. 27. A – B) and fluorite (C), occasionally also occurring with minor apatite, quartz, dolomite, microcline and calcite (Fig.

27. A&D). Microcline is associated with barite on the crystal surface (Fig. 27. E) whilst dolomite and quartz occur along the mineral boundary (Fig. 27. F).

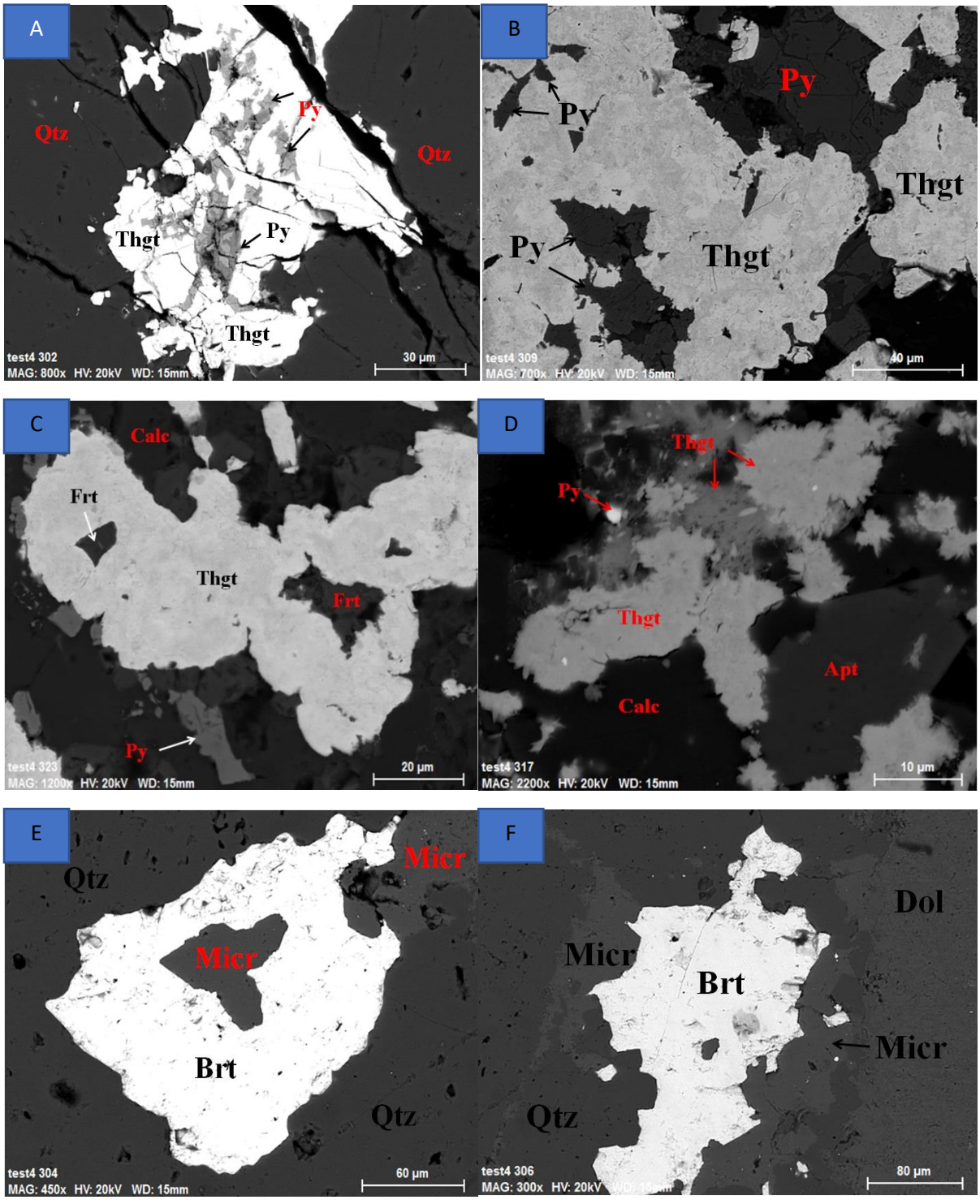


Figure 27. Mineral assemblages and their relationship in the rock sample. A) Thorogummite and pyrite replacing a fractured host rock. B, C &D) Minerals associated with thorogummite. E & F) Barite replacing host rock minerals.

## 4.4.2 Sample: AM-16-002

This sample is dominated by a mineral assemblages of albite, pyrite, diopside, ankerite, fluorite and calcite (Fig. 28). Fluorite and pyrite occur by replacing calcite, diopside and albite respectively (Fig. 28 A&B), fluorite is association with calcite and ankerite along mineral boundary (Fig. 28 B).

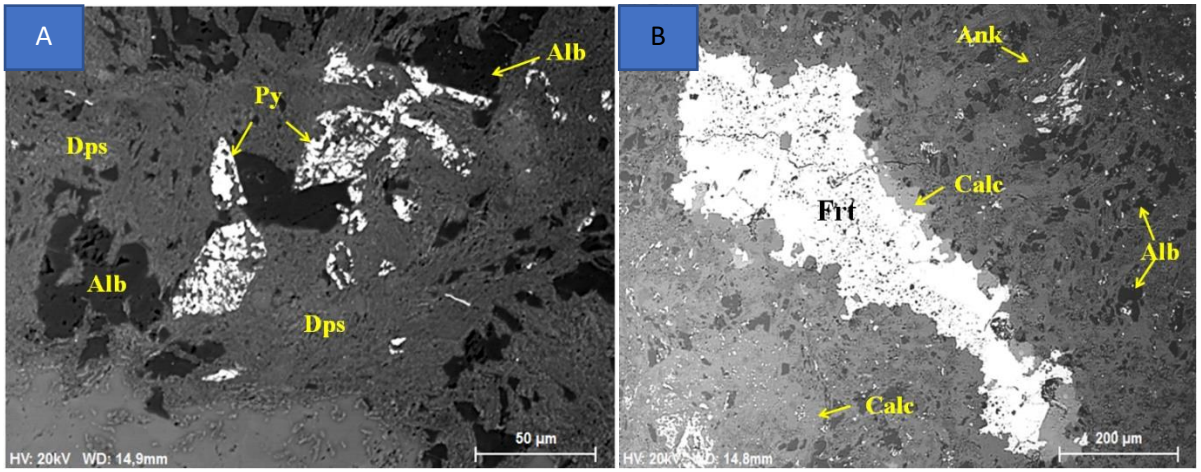


Figure 28. Mineral assemblages and their relationship in the rock sample. A&B) Pyrite and fluorite in association with host rock minerals.

## 4.4.3 Sample: AM-16-003A & B

These samples are dominated by a mineral assemblages of microcline, barite, quartz, calcite, dolomite and apatite (Figure 29). The samples are replaced by barite and apatite which form anhedral and euhedral crystal, respectively (Fig. 29 – D). Barite is associated with microcline at crystal boundaries (Fig. 29 – A) and quartz and calcite occur along mineral boundaries (Fig. 29 – B). Euhedral and fractured apatite was observed in the sample in association with dolomite and microcline. Fractures are filled with microcline and other co-precipitated minerals being dominated with Ca, P, Ti and Zr elements (Fig. 29 C – D).

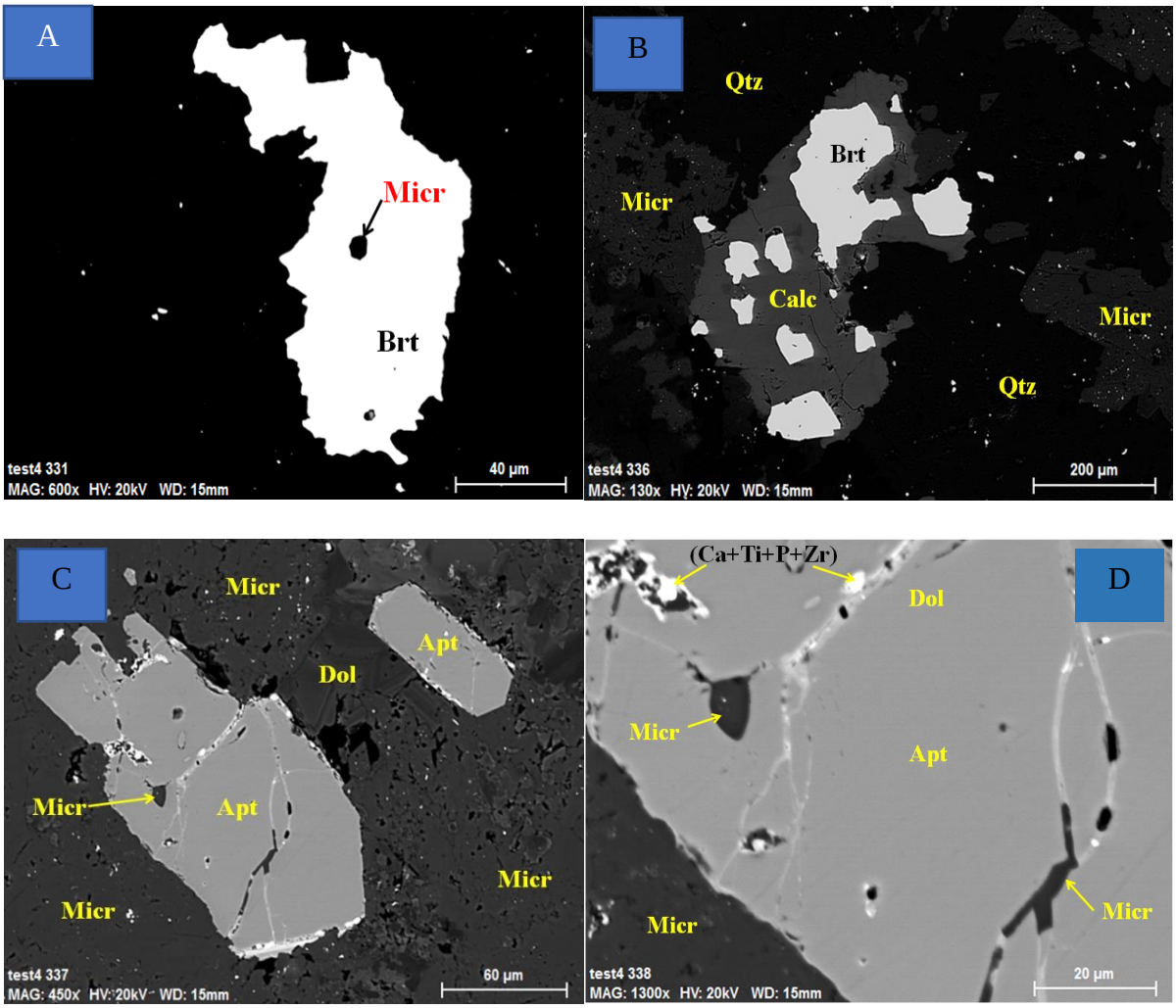


Figure 29. Mineral assemblages and their relationship in the rock sample. A) Observed barite under low contrast. B) Barite in association with host rock minerals. C&D) Fractured apatite crystal precipitated with microcline and fluid-rich dominated with Ca, Ti, P and Zr.

## 4.4.4 Sample: AM-16-004

The sample is dominated by a mineral assemblages of ankerite, quartz, microcline, barite and dolomite (Figure 30). Barite occurs as a secondary phase replacing quartz, dolomite and microcline in the rock sample (Fig. 30 – B). All minerals occur in association with barite along crystal boundaries.

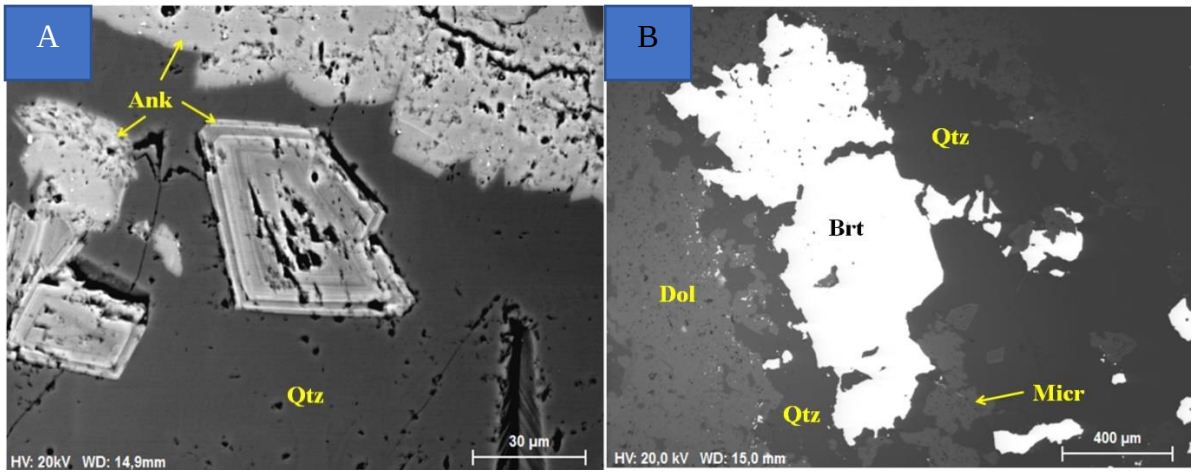


Figure 30. Show mineral assemblages and their relationship in the rock sample. A) Ankerite and quartz. B) Secondary mineral barite in association with host rock minerals.

## 4.4.5 Sample: AM-16-005

The sample is dominated by an assemblages of hornblende, titanite, epidote, calcite, pyrite and quartz (Figure 31). Granular and euhedral crystal of epidote is enclosed within hornblende crystal (Fig. 31 – A) forming an elongated crystal shape.

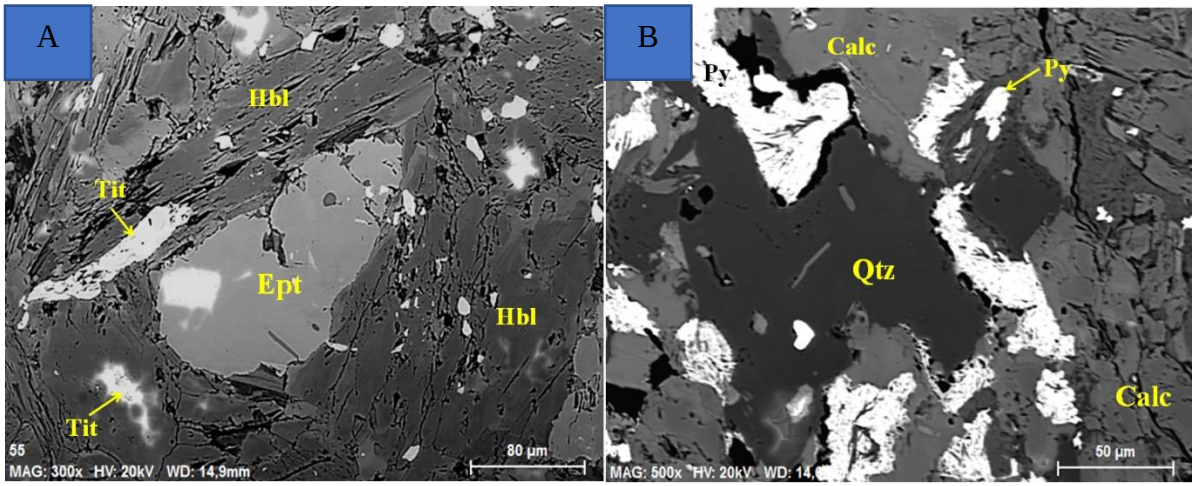


Figure 31. The mineral assemblages and their relationship in the rock sample. A) Epidote crystal enclosed within hornblende mineral. B) Secondary mineral pyrite replacing the host rock minerals.

## 4.4.6 Sample AM-16-007

The sample is dominated by a mineral assemblages of calcite, pyrite and thorogummite (Figure 32). Fractured and euhedral crystal of thorogummite occurs by replacing the host rock minerals and is sparsely distributed in the sample. Thorogummite and pyrite grow in close association (Fig. 32 A&B). Fine-grained pyrite occurs in a fine network of fractures and form irregular crystal shapes.

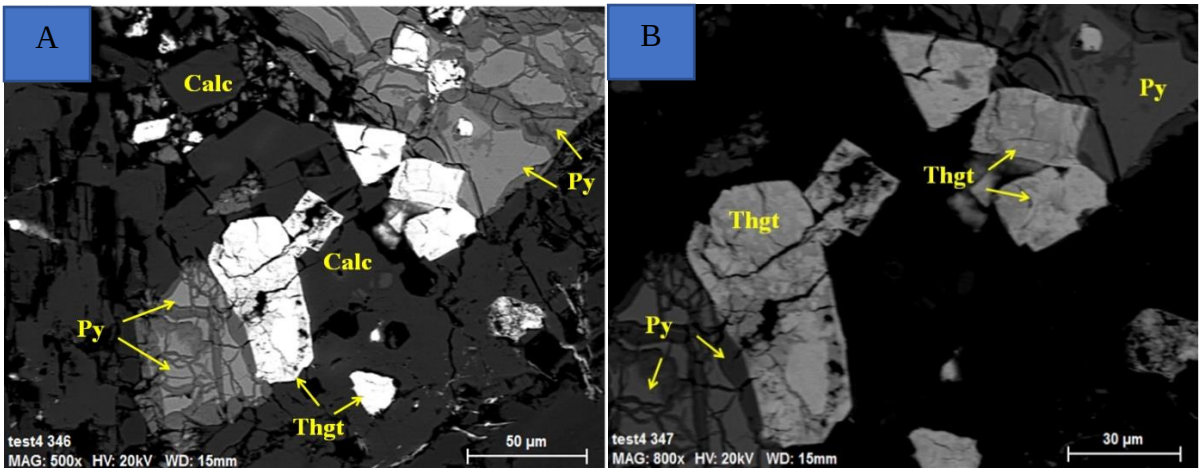


Figure 32. Show mineral assemblages and their relationship in the rock sample. A) Thorogummite and pyrite observed under normal light. B) Thorogummite and pyrite observed under low light contrast.

## 4.4.7 Sample: AM-16-008

The sample is dominated by a mineral assemblages of microcline, quartz, fluorite, pyrite and thorogummite (Figure 33). Again thorogummite and pyrite show a close association (Fig. 33 - C&D). Thorogummite and pyrite also are associated with an intermediate mineral phase mixed with Fe, Si, Al and Ca elements (Fig. 33 - C&D).

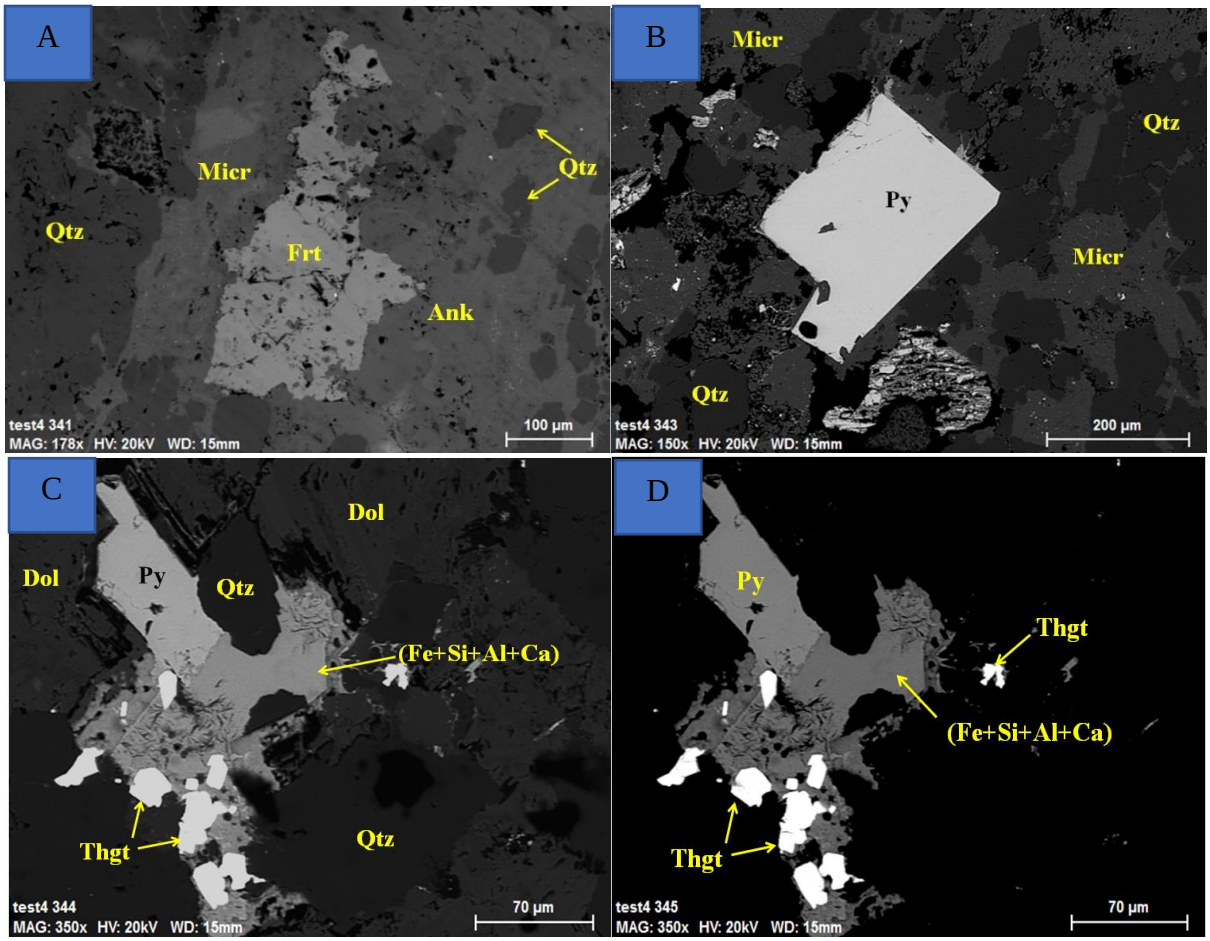


Figure 33. Show mineral assemblages and their relationship in the rock sample. A) Fluorite crystal in association with other minerals in the host rock. B) Euhedral crystal of pyrite replacing mineral in the host rock. C) Thorogummite and pyrite under normal and deem light respectively.

## 4.4.8 Sample: AM-16-009

The sample is dominated by a mineral assemblages of microcline, quartz, pyrite and thorogummite (Figure 34). Thorogummite and pyrite occurs by replacing the host rock and form sub-hedral to euhedral crystals.

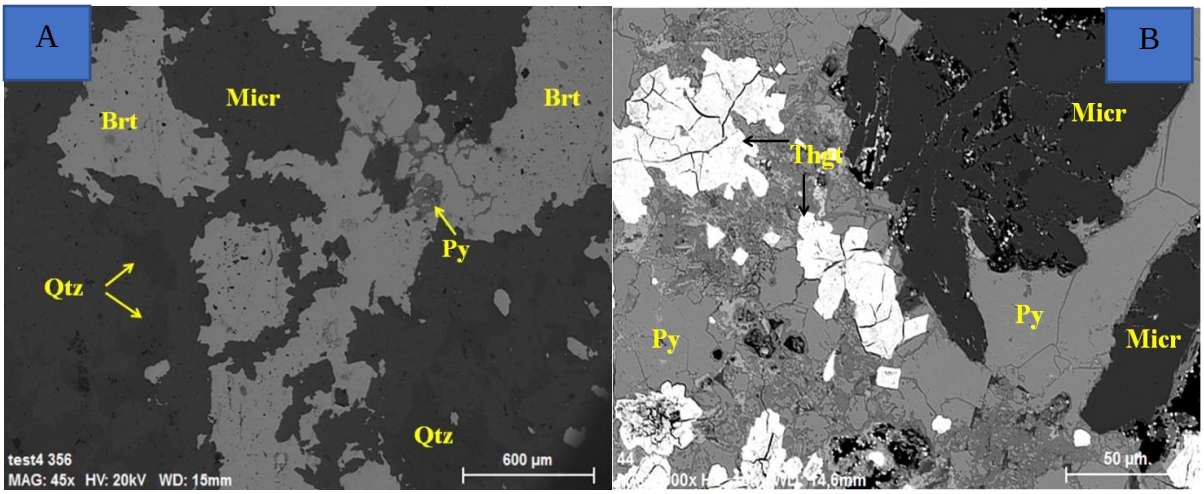


Figure 34. Show mineral assemblages and their relationship in the rock sample. A& B) Thorogummite and pyrite replacing the host rock minerals

## 4.4.9 Sample: AM-16-010A & B

The samples are dominated by mineral assemblages of microcline, ankerite, barite, thorogummite and pyrite (Figure 35). Barite and pyrite occur as a secondary phases replacing the host rock minerals, however, barite and pyrite replace each other along crystal boundaries in the sample (Fig. 35 – B). Pyrite show a close relationship with fine-grained and scattered crystals of thorogummite along crystal surfaces (Fig. 35 – C).

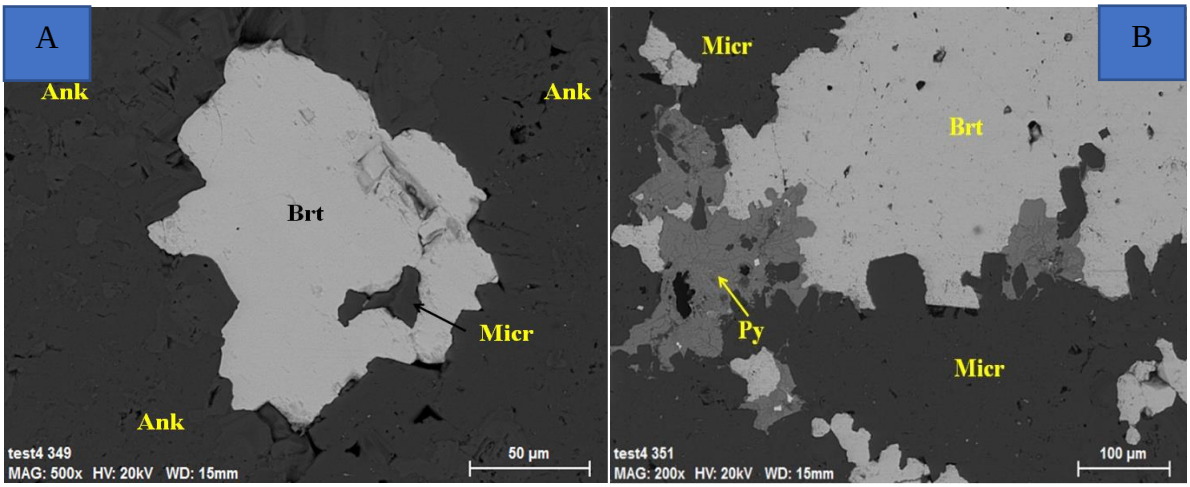

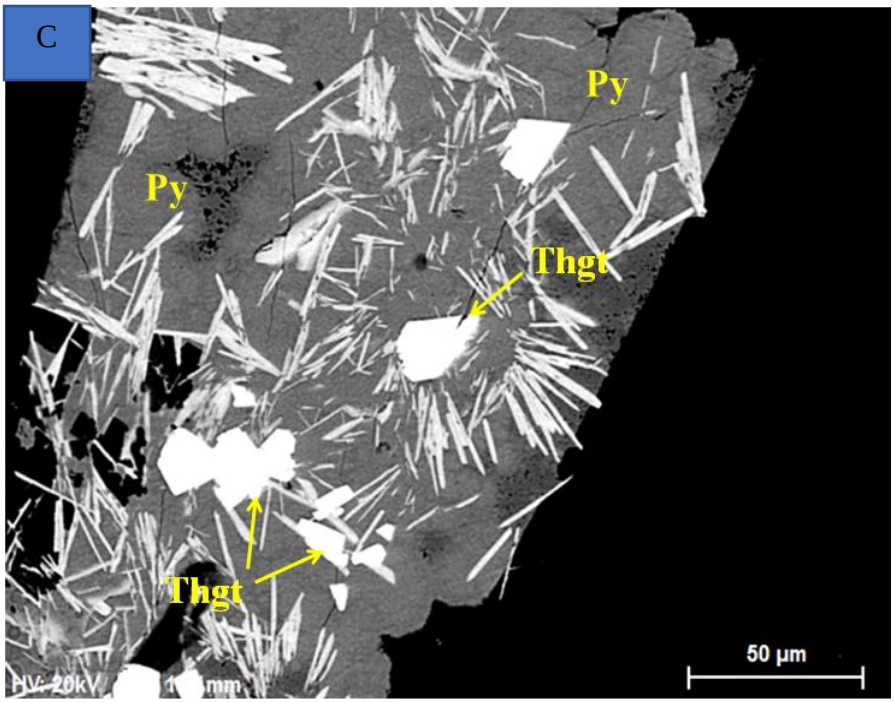


Figure 35. Show mineral assemblages and their relationship in the rock sample. A) Barite replacing the host rock mineral. B) Association of secondary phase pyrite and barite in the sample. C) Relationship of pyrite and thorogummite (needle-like structures) in the sample.

## 4.5 Inductively-Coupled Mass Spectrometry (ICP-MS)

This involves the analysis of powdered samples by using AN ICP-ASE instrument. The obtained results are reported as geochemistry of REE and incompatible trace elements.

### 4.5.1 REE Geochemistry

Rare earth elements (REE) distribution patterns and compositions differs significantly across all samples. Most samples (Fig. 36) features the same chondrite normalized REE patterns with a relative enrichment in HREE compared to LREE. On the contrary, sample AM-16-003B (Red-carbonate) and AM-16-005 (lamprophyre dyke) show the opposite trend with high LREE and low HREE. The REE pattern of Lamprophyre dyke show a slight change in its slope right after La, Ce, Pr, Nd and trends smoothly down to Lu (Fig. 36). A slight difference is observed in sample AM-16-003B where the REE pattern show a constant trend from La-Sm, and the slope changes significantly down to Lu. In addition, AM-16-007 show a similar trend to AM-16-003B and AM-16-005 (lamprophyre dyke) samples but display a negative europium (Eu) anomaly (Fig. 36).

In general, all samples in the Trondheimfjord area are depleted in LREE compared to HREE, with AM-16-005 and AM-16-003B being the exceptions (Fig. 36).

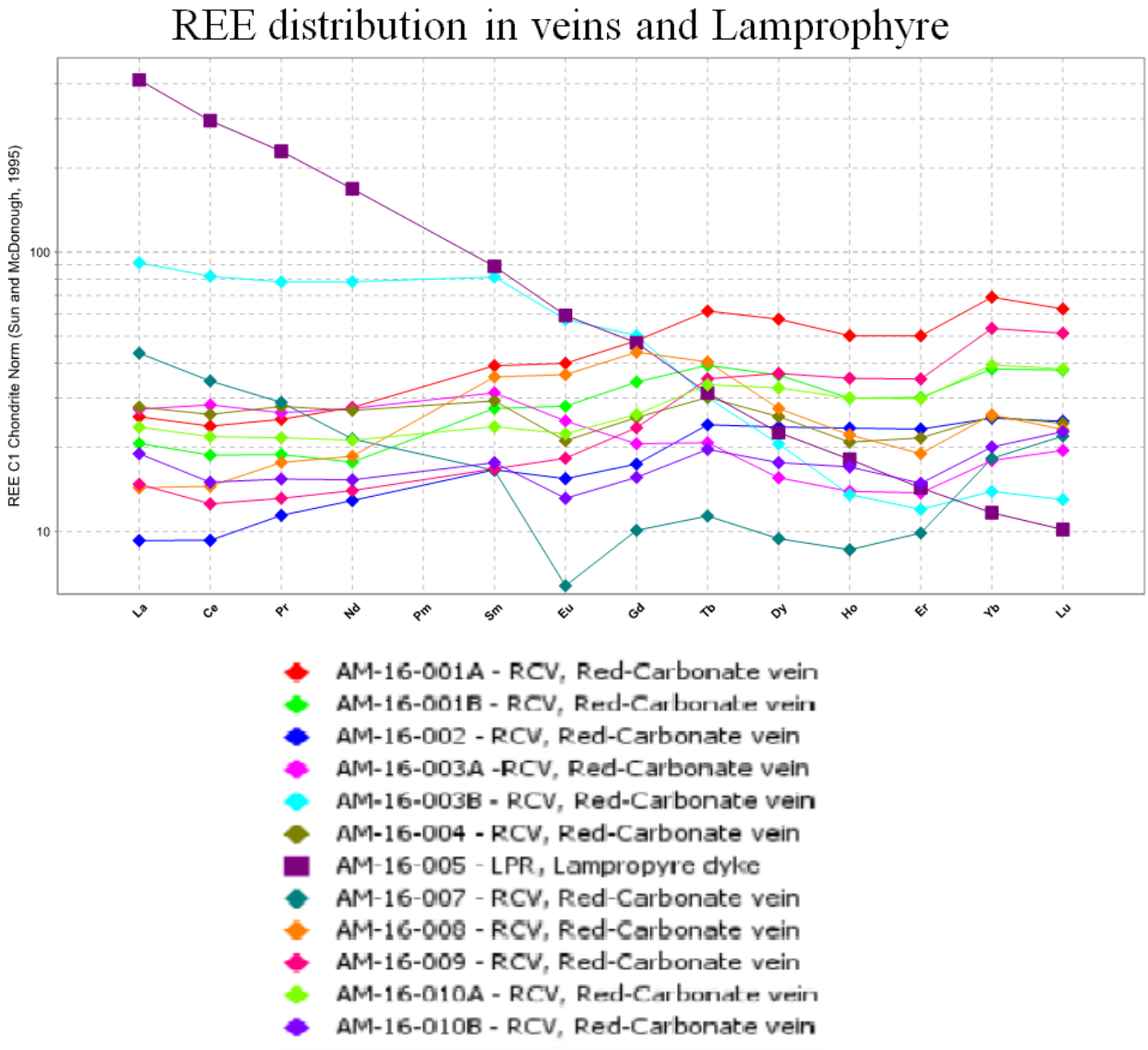


Figure 36. REE distribution plots for Trondheimfjord rock samples. Chondrite normalisation coefficients from Sun and McDonough (1995)

## 4.5.2 Incompatible trace element

In figure 37 incompatible trace element distribution in the samples are represented after being normalized to primordial mantle. Red-carbonate veins display similar patterns in most samples. The Lamprophyre dyke deviates again with a different pattern (Figure 37). Red-carbonate veins are observed to have high Ba, Th, U and Pb concentrations, though their concentration varies

between samples. In general, Ba concentrations are not evenly distributed due to its low and high value between samples. Other elements are present in small concentration whereas Ta and Ti are depleted in samples.

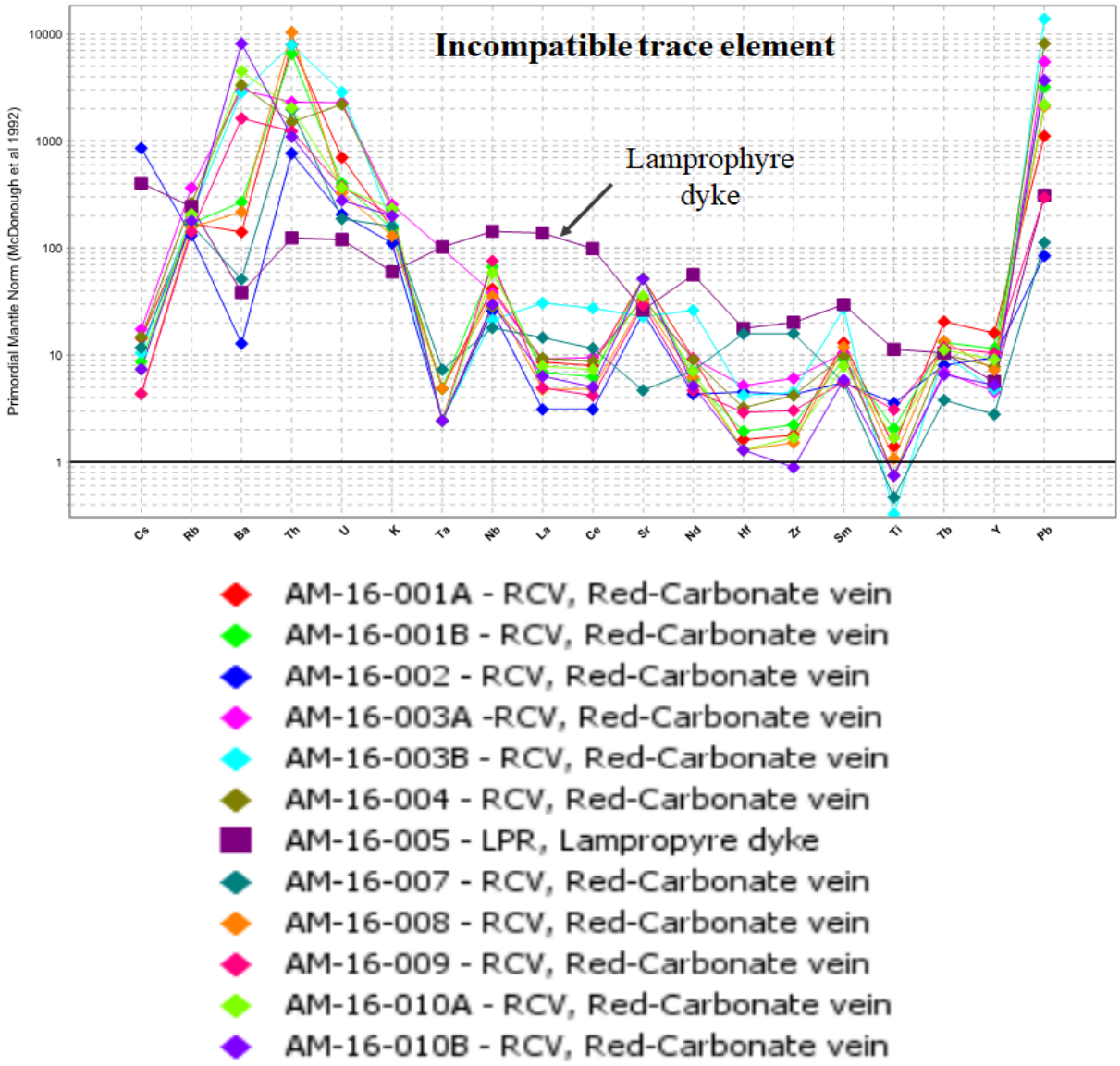


Figure 37. Incompatible trace element distribution in samples normalized to primordial mantle with distribution factors from McDonough et al (1992).

## 4.5.3 Harker diagram for major elements

In figure 38 most oxides are plotted in Harker diagram, where all red-carbonate veins and Lamprophyre dyke samples from the study area are represented. All samples contain variable oxide and silica composition in the rocks, where silica contents range from 38.2 to 80.9 wt% $SiO_2$. The data from red-carbonate veins display a continuous trend in most of the plots.

However, a contribution from the Lamprophyre dyke to these plots is difficult to deal with. This is because only one sample was included in the analysis, therefore, it might not give a correlative interpretation relative to other plots. With exception to Harker plots of BaO, SrO, $K_2O$ and $Al_2O_3$, display more scatter between samples. In the plots of $Fe_2O_3$, MgO, $TiO_2$, MnO and CaO displays a linear trend which decrease with increase in silica content.

Plots of $Na_2O$ and $P_2O_5$ have low oxide concentrations and display nearly flat patterns with constant trend relative to the silica composition. Oxides with concentration >1 wt% are considered as major rock-forming oxides in the red-carbonate veins which include; CaO (ca.1.0 – 13.5 wt%), MgO (0.5 – 8.5 wt%), $Fe_2O_3$ (ca. 1.0 – 7.5 wt%), $Al_2O_3$ (4.8 – 10 wt%), $K_2O$ (3.0 – 7.25 wt%) and BaO (0 – 6 wt%). Oxides with concentration < 1 wt% also, are considered as accessory forming oxides including; $TiO_2$ (<0.75 – 0.75 wt%), MnO (<0.025 – 0.15 wt%), $Na_2O$ (0 – 2 wt%), SrO (0.04 – 0.12 wt%) and $P_2O_5$ (<0.05 – 0.5 wt%).

Similarly, Lamprophyre dyke can be considered as red-carbonate veins in terms of major and accessory forming oxides, where $Al_2O_3$ (10 wt%), MgO (13 wt%), $Fe_2O_3$ (11 wt%), and $TiO_2$ (>2.25 wt%) form the major forming oxides whilst $K_2O$ (ca. <1.5 wt%), BaO (0.0 wt%), MnO (0.27 wt%), $Na_2O$ (0.25 – 0.5 wt%), SrO (0.05 wt%) and $P_2O_5$ (0.7 wt%) form accessory forming oxides.

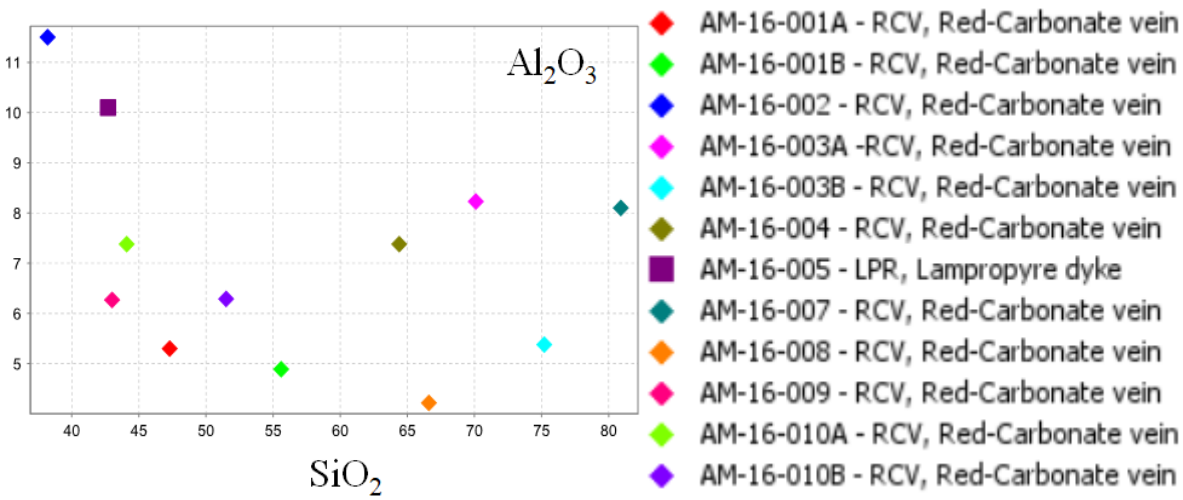

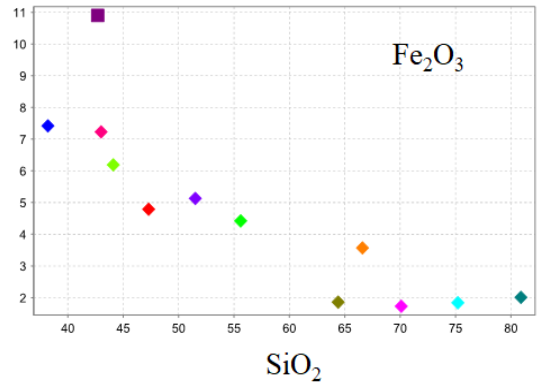
Fe2O3
SiO2

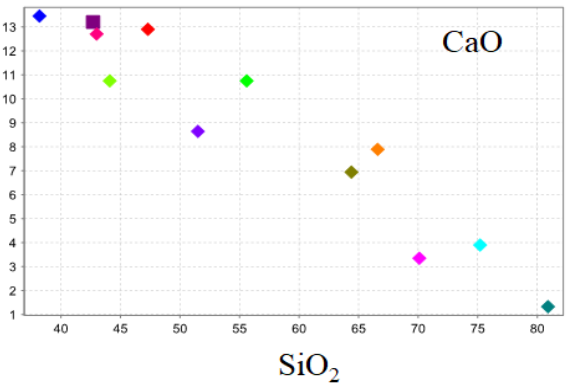
CaO
SiO2

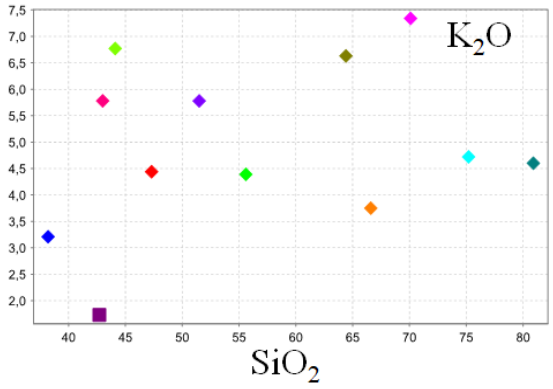
K2O
SiO2

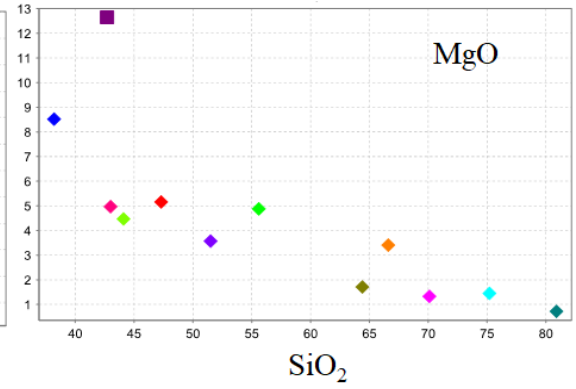
MgO
SiO2

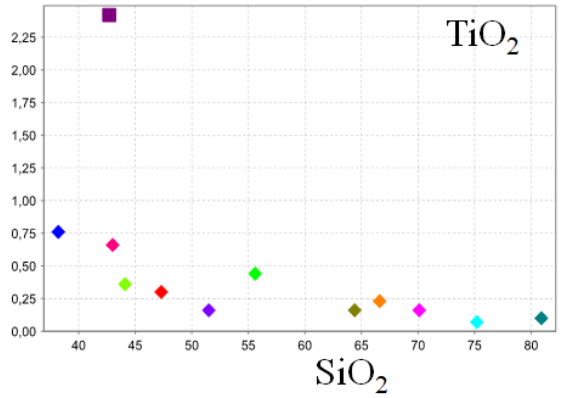
TiO2
SiO2

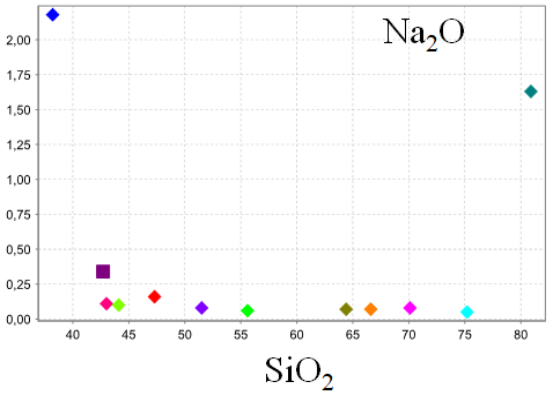
Na2O
SiO2

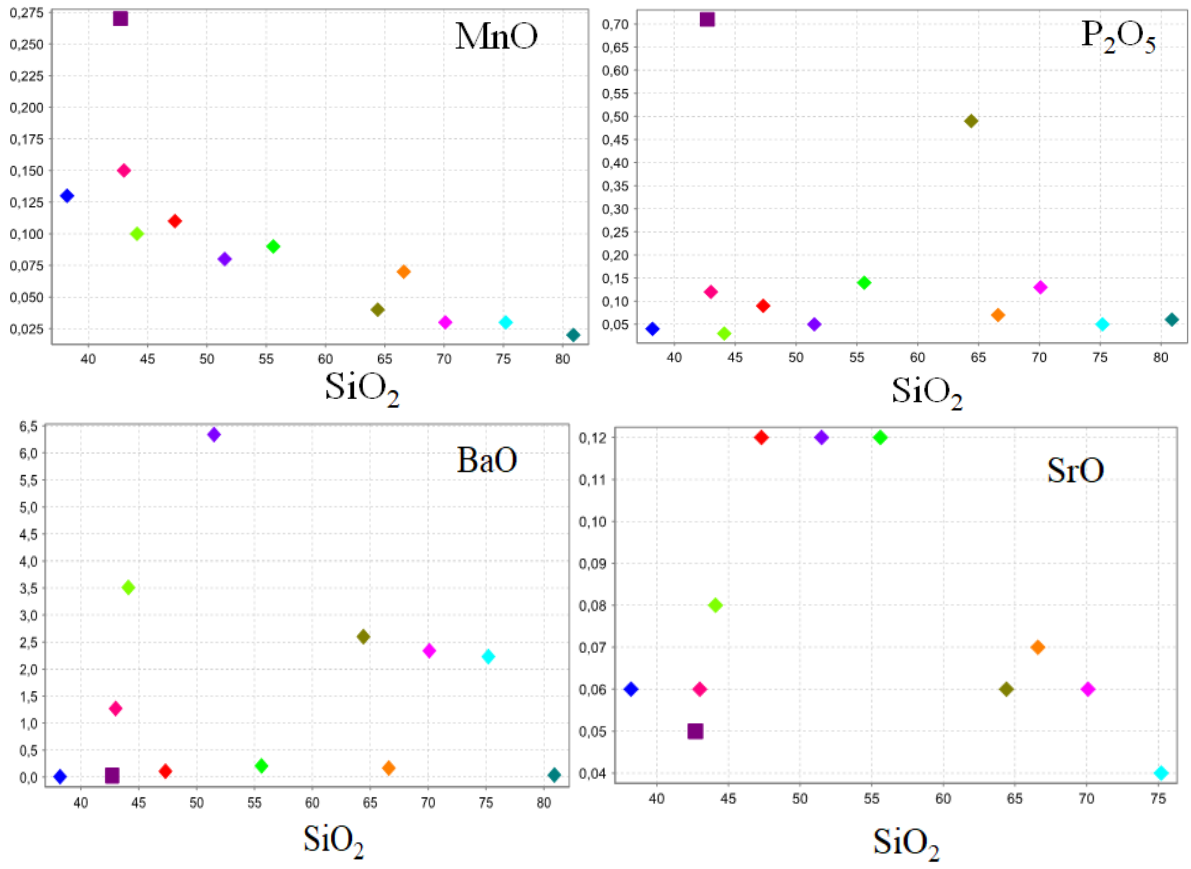


Figure 38. Harker diagrams for all analyzed red-carbonate veins and Lamprophyre rock. Oxides are given in wt%.

## 4.6 Electron Probe Micro Analysis (EPMA)

EPMA uses the X-ray Dispersive Spectrometers (EDS) for mineral identification in weight percent (wt%) for major and parts per million (ppm) for trace elements composition. Different mineral composition in samples were identified and mineral formula was calculated using ***Andy Tindle Software*** (Tindle). Identified minerals in each sample are represented in table 16.

***Note****: Some minerals display total percentage of their chemical composition greater or less than 100 wt% (see appendix II). Unfortunately, the EPMA was very unstable at the time of running the analysis. Therefore, the analysis must be regarded as semi-quantitative.*

Table 15. Show mineral composition in the rock samples

| **AM-16-001A** | **AM-16-001B** | **AM-16-002** | **AM-16-003A** | **AM-16-003B** |
|---|---|---|---|---|
| Thorogummite | Thorogummite | Microcline | Thorogummite | Microcline |
| Dolomite | Dolomite | Albite | Dolomite | Fluorapatite |
| Microcline | Microcline | Fluorite | Microcline | Quartz |
| Ankerite | Ankerite | Clinozoisite | Ankerite | |
| Quartz | Fluorite | Epidote | Quartz | |
| | Quartz | | Ba-REE Carbonate | |
| | | | | |
| **AM-16-004** | **AM-16-005** | **AM-16-007** | **AM-16-008** | **AM-16-009** |
| Microcline | Clinozoisite | Thorogummite | Thorogummite | Thorogummite |
| Ankerite | Quartz | Microcline | Microcline | Ankerite |
| Quartz | Ba-REE Carbonate | Quartz | Dolomite | Ba-REE Carbonate |
| Fluorapatite | Magnesiohornblende | Perovskite | Calcite | |
| Ba-REE Carbonate | | | Quartz | |
| | | | Fluorapatite | |

| AM-16-010A | AM-16-010B |
|---|---|
| Microcline | Microcline |
| Ankerite | Ankerite |
| Quartz | Quartz |
| Ba-REE Carbonate | Ba-REE Carbonate |

Table 16. Mineral phases and their chemical formula identified under Electron Micro Probe Analysis (EPMA). The chemical formula was calculated using ***Andy Tindle Software*** and some are theoretical formula.

| Mineral name | Calculated Mineral formula |
|---|---|
| Thorogummite | (Th, U, REE) (Ca, Fe, Si) (O, F) (?) |
| Dolomite | $Ca\ Mg\ (CO3)_2$ |
| Calcite | $CaCO_3$ |
| Ankerite | $Ca\ (Mg, Fe)\ (CO3)_2$ |
| Microcline | $KAlSi_3O_8$ |
| Albite | $NaAlSi_3O_8$ |
| Fluorite | $CaF_2$ |
| Ba-REE Carbonate | $Ba\ (Ce, REE)\ (CO_3)_2\ F$ |
| Epidote/Clinozoisite | $Ca_2\ Al_{(2.5)}\ (SiO_4)_3\ (OH)Fe^{3+}_{(0.41)}$ |
| Epidote/Clinozoisite | $Ca_2Al_{(2.3)}\ Fe^{3+}_{(0.5)}\ (SiO_4)_3\ (OH)$ |
| Magnesiohornblende | $Ca_2\ Mg_4\ (Al, Fe^{3+})_2\ Si_6\ O_{22}\ (OH)_2$ |
| Perovskite | $CaTiO_3$ |
| Fluorapatite | $Ca_5\ (PO4)_3\ F$ |

# Chapter 5

# Discussion

Evaluation of the chemistry and mineralogy associated with alteration of the thorium (Th) mineralised veins at the Ytterøy island was a major focus and the principal aim of this study. The investigation is based on field work, mineral chemistry and geochemistry of selected samples from the Ytterøy island. Chemical analyses of the samples indicate that the alteration in the red-carbonate veins was a function of the fluid – rock interaction processes and the next sections will discuss various aspects of these processes.

## 5.1 Mineralogy

Optical microscopy, XRD, SEM and EPMA documents the dominance of quartz, calcite, dolomite, ankerite, barite, microcline, albite, epidote and hornblende comprising the red-carbonate vein samples. Accessory phases includes siderite, fluorite, thorogummite, biotite, muscovite, pyrite, apatite, and diopside. The Lamprophyre dyke is dominated by an assemblages of hornblende, epidote and microcline whilst pyrite, titatite, biotite and calcite occur are accessory phases. Geiger Muller investigations indicated Th radiation up to 8 µsv/h in the veins, occassionaly, in some samples relatively low or no Geiger Muller reading were observed. This obeservation indicates that Th was not equally distributed in the red-carbonate veins. Mineral assemblages associated with red-carbonate veins were formed as a result of hot aqueous solution interacting with the host-rock and led to the formation of a new stable mineral assemblages. This mineral assemblage includes quartz, microcline, fluorite and calcite (Grønlie & Torsvik, 1989) and was often replaced/altered by other minerals.

Based on alteration assemblages described in the result section, the following major and minor assemblages are isolated.

(1) Quartz – microcline – dolomite ± thorogummite, calcite, pyrite, apatite, fluorite

(2) Quartz – microcline – barite – calcite – dolomite ± pyrite and

(3) Quartz – microcline – albite – hornblende – dolomite/ankerite ± fluorite, calcite, diopside and biotite.

The dominance of quartz and microcline in most mineral assemblages indicate that these mineral phases are highly resistance to rock-fluid interaction. Thus, these mineral phases may be considered to have been affected with hydothermal fluids in a non-pervasive way of alteration (Pirajno, 2009). Calcite was altered by the hydrothermal fluids to form other carbonate minerals such as dolomite, siderite and ankerite series (Grønlie & Torsvik, 1989). This occurred because the hydrothermal fluids were rich in Mg, Fe and Mn (Robb, 2005). However, elsewhere calcite is stable which indicate that not all the hydrothermal fluids were rich in Mg, Fe, and Mn. Accordingly, the presence or absence of calcite demonstrates both a selective and a non-pervasive style of hydrothermal alteration (Pirajno, 2009). Barite is not associated with thorogummite which indicate dissimilar sources of fluids responsible for barite and thorogummite precipitation, respectively.

The Lamprophyre dyke and red-carbonate vein samples was equally treated during laboratory analyses. The dyke is dominated by mineral assemblages of hornblende, epidote, titanite, calcite, quartz, biotite and microcline. Lamprophyre dyke show mineral assemblages like red-carbonate vein but is characterized with low silica content (i.e. $CO_2$-rich rock) (S. Foley, 1992). The lamprophyre dyke phases are less affected by fluid interaction compared to those observed in the red-carbonate vein. This was due to the reason that most of the minerals in the Lamprophyre dyke preserve their original texture as opposed to red-carbonate veins. Epidote occur enclosed in hornblende (Figure 22 – C) which indicate that hornblende was formed after epidote crystallization.

## 5.2 Thorogummite

Thorogummite is an important accessory phase in the red-carbonate veins. Occassionally, it is associated with fluorite, apatite and pyrite. Thorogummite and pyrite are the most dominant secondary phases and replace each other in the samples. In the backscattered image (Figure 27 – A), thorogummite is characterized by fractures filled with pyrite. Formation of fractures indicate excess fluid pressure (Robb, 2005) generating a network of fractures where pyrite was precipitated. The red-cabonate veins are silica poor (up to 15wt% $SiO_2$) and also has low U concentrations. Th, Ce, Ca, Fe and P contents are strongly variable indicating either variable fluid chemistries and/or variable host rock conpositions (Hirtopanu et al., 2013). The effect of variable hydrothermal fluid compositions can be observed in the EDS spectra (Figure 39);

where Th, Si, P, Fe and Ca in thorogummite varies dramatically from grain to grain and within single grains. Again, thorogummite and pyrite were observed precipitating an intermediate mineral composition (i.e. Fe+ Si + Al + Ca) (Figure 33 – C & D) indicating co-precipitation of two dissimilar mineral phases. It may be considered that the compositional differences is a result of Fe – Si rich fluids interacting with feldspars (microcline) and carbonates (calcite/dolomite) phases. Therefore, feldspars and carbonate might have contributed Al and Ca to the hydrothermal solutions. A similar situation may be observed in fractured apatite crystals (Figure 29 – C) where co-precipitation of an intermediate composition (i.e. Ca + P + Ti + Zr) was observed. Due to the dominance of secondary phases such as thorogummite, pyrite and apatite, the host rock is considered selectively altered (Pirajno, 2009) by hydrothermal fluid rich in $Th^{4+}$, $Fe^{2+}$, $S^{2-}$, $(PO_4)^{3-}$ and $Si^{4+}$. These cation and anion are considered to have been incorporated into thorogummite and pyrite, but not limited to REE, Ca, U, Ti, Zr and F species. The presence of pyrite in the host rock indicate relatively reducing conditions during the formation of the red-carbonate vein. Thorogummite partially replaces earlier formed fluorite (Figure 18 & 27 – C).

EPMA analyses reported variable compositions of thorogummite in some of the red-carbonate vein samples with a range from 58.96 wt% to 77.21 wt% $ThO_2$. In contrast, Grønlie, 1984; in Grønlie and Torsvik (1989) reported 48 wt% to 56 wt% of $ThO_2$. This indicate more Th-rich fluid activity within rocks and was responsible for fluid – rock interaction and/or metamictization process (Grønlie & Torsvik, 1989; Hirtopanu et al., 2013). Consequently, the process led to precipitation of Th-rich phases for example thorogummite. Variable $ThO_2$ concentrations were even in single thorogummite grains (e.g. AM-16-007: 30.11 wt% and 61.74 wt% and AM-16-008: 19.15 wt% to 58.98 wt% $ThO_2$, see appendix II) indicating variable hydrothermal fluid interaction in the host rocks. A close relationship between Ce and Th was observed in samples rich in thorium indicating a possible redox reaction (oxidation) involving $Ce^{3+} \rightarrow Ce^{4+}$ (Wood, 1990a). Like $Th^{4+}$, oxidized cerium ($Ce^{4+}$) is considered to be incorporated together with the thorium in the crystal lattice due to similar size and charge. This define an oxidation stable state of Cerium ($Ce^{4+}$) which associate strongly with $Th^{4+}$. This might explain why Ce show strong association with Th in the atomic lattice in some of the red-carbonate vein samples. Scanning electron microscopy and EPMA analyses indicate the dominance of Th in thorogummite phase whilst feldspars (microcline), barite, phosphate carbonates (dolomite, calcite and ankerite) and the lamprophyre dyke contains less/no thorium.

In most cases, thorium rich minerals are reported to occur in rocks that are associated with alkaline igneous complexes (Van Gosen et al., 2009). Thorogummite form after hydrothermal alteration of thorite ($ThSiO_4$) (Hirtopanu et al., 2013) that led to the formation of an intermediate pseudomorph mineral thorogummite between Xenotime ($YPO_4$) and the thorite end-members (Burt, 1989b). The alteration process occurs through substitution of $(SiO_4)^{4-}$ and $(OH)^{4-}$ in the thorite atomic lattice (Piilonen et al., 2014). In this case, the alteration process is considered to form a crystal structure that can accommodate other large and highly charged cations and anions such as $Ce^{4+}$, $REE^{3+}$, $U^{4+}$, $Ca^{2+}$, $Fe^{2+}$, and $Mg^{2+}$ to form thorogummite; (Th, REE, U) (Ca, Fe, Si) (O, F). The chemical formula is expected to change relative to the composition of the fluid and the fluid/rock ratio (Piilonen et al., 2014). Thorium (Th) is easily transported in aqueous solution rich in $F^-$, however, aqueous solution rich in $Cl^-$ and $(CO_3)^{2-}$ decrease the Th solubility (Hazen et al., 2009). Thorogummite in the northern Trondheimfjord area is comparable with that of the Belcina & Jolotca area (Hirtopanu et al., 2013) in sharing similar characteristics in optical microscopy and SEM. Similarly, both areas are characterized by low $UO_2$, $Ce_2O_3$ and chemical variation within thorogummite due to variation in fluid chemistries and fluid/rock ratio. However, EPMA analyses reported higher $ThO_2$ concentrations (77.21 wt%) in the northern Trondheimfjord thorogummite than thorogummite in Belcina and Jolotca (68.49 wt% $ThO_2$). Unlike northern Trondheimfjord, Belcina and Jolotca thorogummite, Gradistea de Munte occurrence (GM, Sebes Mts, South Carpathians) (e.g. Hirtopanu et al., 2012 in Hirtopanu et al., 2013) thorogummite contains high $UO_2$ (>20 wt %).

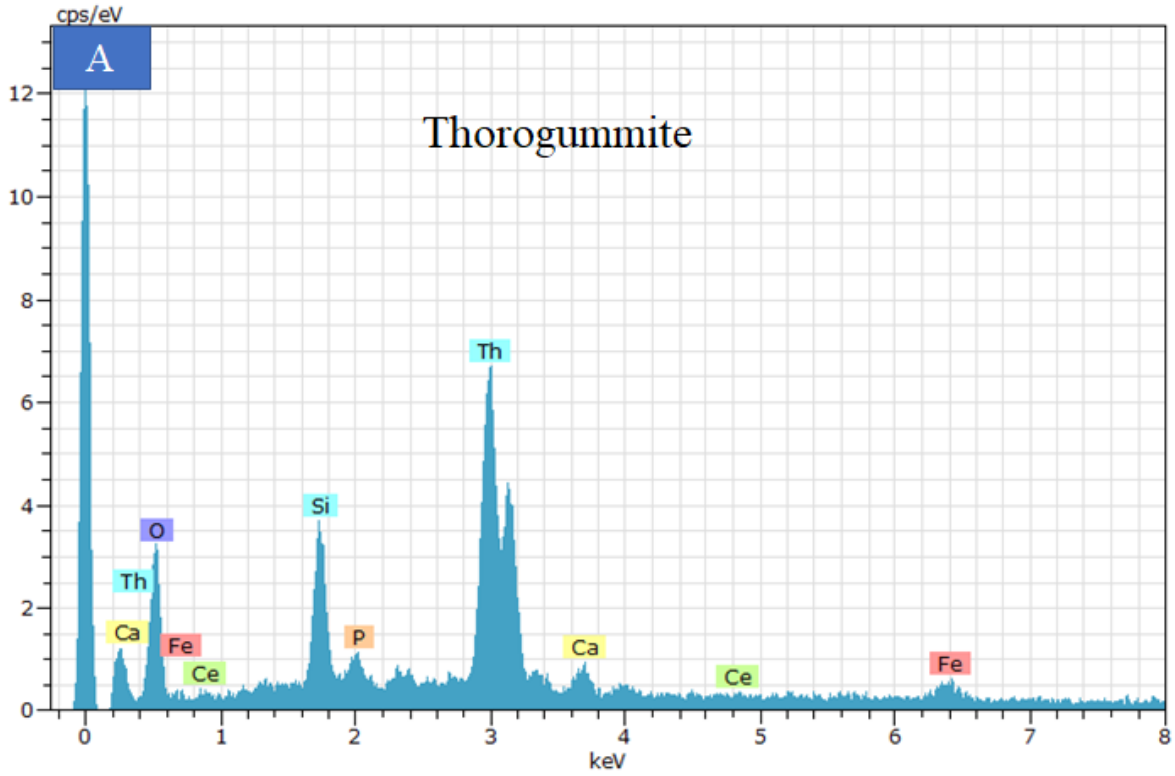
cps/eV
A
Thorogummite
O
Th
Ca
Fe
Ce
Si
P
Th
Ca
Ce
Fe
keV

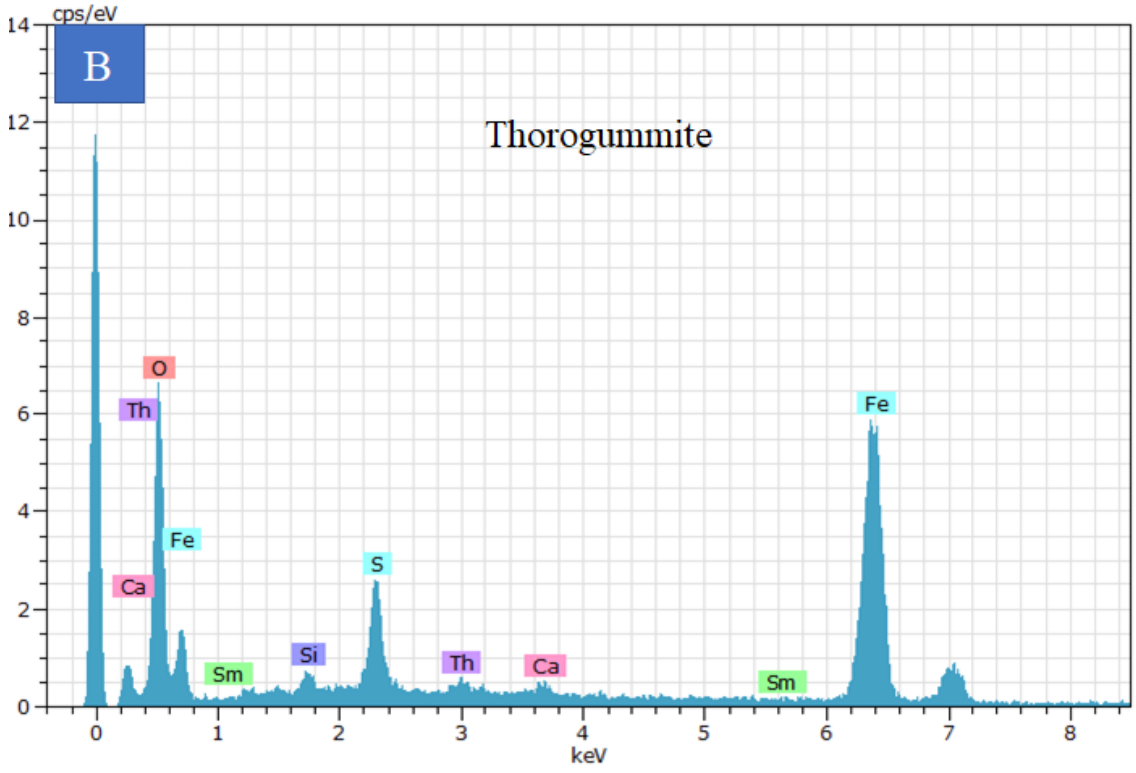
cps/eV
B
Thorogummite
O
Th
Fe
Ca
Sm
Si
S
Th
Ca
Sm
Fe
keV

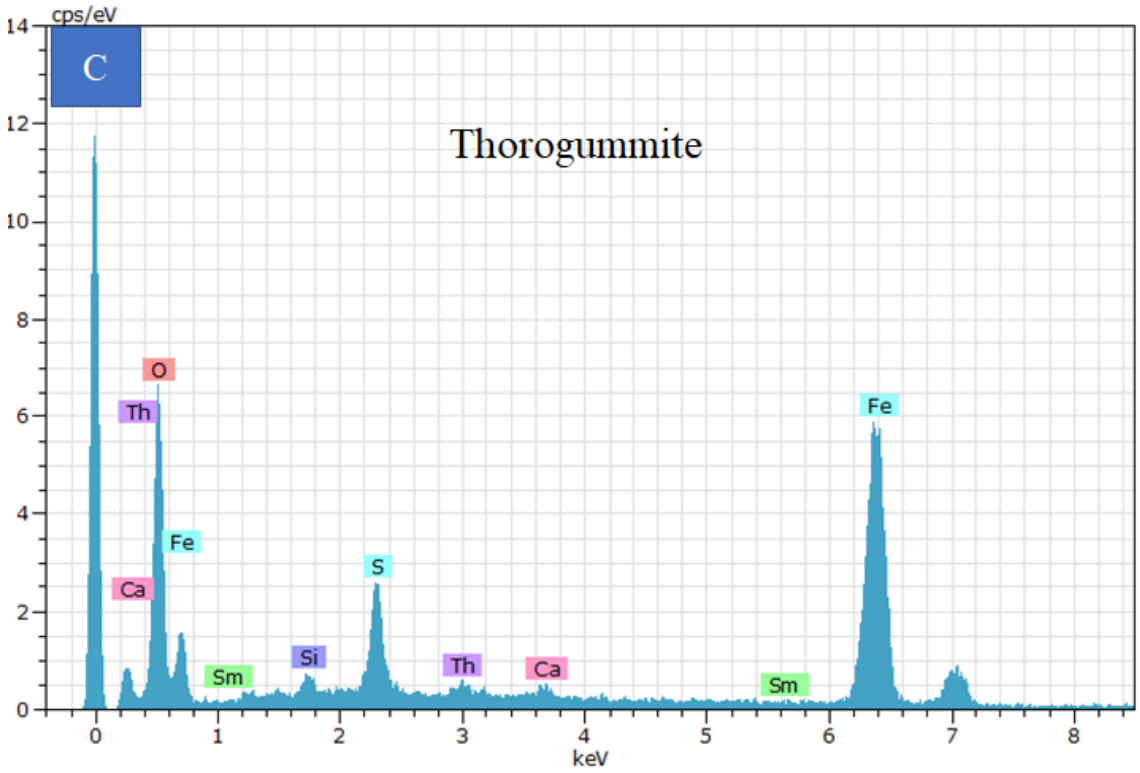


Figure 39. A – C show the effect of hydrothermal fluid oscillation reflected in thorogummite mineral phase.

## 5.3 Geochemistry

Whole-rock chemistry of investigated samples indicates different REE patterns and variable compositions. Most of the red-carbonate vein display parallel REE patterns indicating that the rocks are genetically related. Harker variation diagrams for major oxides also show similar trends for the samples. With exception to sample AM-16-003B (red – carbonate vein), other samples are characterized with LREE depletion. Red-carbonate vein (AM-16-003B, Figure 36) and Lamprophyre dyke (AM-16-005) show similar LREE enrichment, however, the former sample contain low LREE concentration. The enrichment of LREE might be facilitated by the presence of an accessory phase of Ba-REE rich carbonate, apatite and fluorapatite. It can also be suggested that, both rock types were enriched in similar processes despite that they may originate from different source rocks. Most of the investigated accessory minerals in the red-carbonate (Ba-REE rich carbonate, apatite and fluorapatite) contain low REE concentration. Whole-rock trace element chemistry show high Ba, Th, U and Pb concentrations in red-carbonate vein but low concentration in the Lamprophyre dyke. High concentrations of Ba, Th, U and Pb were also reported using SEM and EPMA analyses and are mostly incorporated in barite, thorogummite and sulfides (pyrite). Lamprophyre dyke contain incompatible trace

elements in a range of Cs, La, Ce, Nd and Sm. Despite of its composition, the origin of lamprophyre dyke is beyond this study since there is only one sample being analysed. Unlike the northern Trondheimfjord area, Belcina and Jolotca areas are highly associated with high LREE carbonates such as (bastnasit-(Ce), bastnasite-(La), parisite-(Ce), hydroxylbastnasite-(Ce) and lanthanite(Ce) (Hirtopanu et al., 2013).

## 5.4 Sources of hydrothermal fluids

The mineral assemblages and alteration patterns obeserved in red-carbonate veins indicate variable sources of the hydrothermal fluid. Thorogummite is considered to form because of hydrothermal alteration of thorite (Piilonen et al., 2014). It was reported that $Th^{4+}$ is often transported in aqueous fluids rich in fluoride complexes (Hazen et al., 2009) as implied by common fluorite in the red-carbonate veins. Presence of apatite indicate fluid – rock interaction with phosphate $(PO_4)^{3-}$ rich fluids that led to apatite crystallization. Also, formation of carbonates (dolomite, ankerite and siderite) can be directly linked with fluid – rock interaction with a Mg, Fe and Mn rich fluid. Formation of barite and fluorite indicate an introduction of sulfate and fluoride rich fluids probably from anhydrite and/or calcium fluorite (CaF). There is a possibility that the circulation of hydrothermal fluids in the red-carbonate veins were enriched in brines composition such as NaCl and KCl. The dissociation of NaCl and KCl might have released $Na^+$ and $K^+$ into hydrothermal fluid which in turn resulted in metasomatism of the host rocks (Grønlie & Torsvik, 1989). The behavior of REE in hydrothermal fluids have been studied theoretically (Wood, 1990b) and (Haas et al., 1995) as well as experimentally (Gammons et al., 1996). With regards to the chemistry of fluids and mineral assemblages of samples, the possible ligands that might have been involved in the transportation of REE are $F^-$, $(PO_4)^{3-}$, $(SO_4)^{2-}$ and $(CO_3)^{2-}$ (Williams-Jones et al., 2000; Linnen et al., 2014). In addition, $F^-$, $(CO_3)^{2-}$, sulfate and hydroxide form strong complexes with REE whilst $Cl^-$ form weaker complexes (Williams-Jones et al., 2000). EPMA analyses reported some accessory phases with low concentration of REE including fluorapatite, Ba-REE carbonate and /or fluorite.

## 5.5 Genetic evolution

It may be proposed that the hydrothermal activity in the northern Trondheimfjord area was initiated by emplacement of alkaline magmas at shallow depths accompanied by separation of volatile fluids. The Lamprophyre dykes support this idea, but it can not be confirmed or rejected unless isotope analysis are undertaken. Continuous separation of volatiles led to rapid, focused release of volatile fluids increasing the fluid pressure to exceed the ambient P. Consequently, this caused the formation of veins and hydrothermal breccias. The hydrothermal system developed in multiple stages involving fluid-rock interaction and mineral precipitation in the fracture systems. The earliest effects of hydrothermal alteration involved Na-metasomatism and iron carbonate precipitation and was followed by K-metasomatism and subsequent deposition of quartz, calcite and fluorite (Glønlie & Torsvik, 1989). Availability of fluorite was considered as a major indicator mineral for REE mineralization in the northern Trondheimfjord area. Further alteration and deposition of mineral assemblages in the host rocks is considered to have been accompanied by influx of external fluids (meteoric water). This may be associated by leaching, transportation and deposition of components derived from the source rocks. The deposition of carbonates (dolomite, ankerite and siderite) indicate the introduction of fluids rich in Mg, Fe and Mn that led to pervasive alteration of calcite (carbonization), a process often observed in most of the calcite – rich samples. Formation of mineral such as apatite, barite and pyrite may be caused by continuous mixing of phosphate, barium and sulfides. As discussed earlier, the formation of thorogummite is directly linked with hydrothermal fluid alteration of the mineral thorite probably located at a shallow depth.

# Chapter 6

## 6.1 Conclusion

- It was investigated that, red-carbonate veins and Lamprophyre dyke samples show similar mineral assemblages, but the difference was observed due to dissimilar source rocks. The most mineral assemblage include quartz, microline, calcite, ankerite, dolomite, hornblende, fluorite, barite, epidote, apatite and thorogummite whilst Ba-REE carbonate and fluorapatite form the major REE minerals.
- Mineral assemblages are generally formed through hydrothermal fluid alteration that led to deposition of new minerals. The process involved hydrothermal fluid circulation and influx of external fluids (meteoric waters) responsible for leaching, transportation and deposition of various minerals.
- Th content is concentrated in the thorogummite mineral phase and range between 10.09 wt% to 62.4 wt% Th. However, chemical variation within thorogummite was observed following variable hydrothermal fluid chemistries. The red carbonate veins contain thorogummite concentration up to 77.2 wt% $ThO_2$. In contrast, the lamprophyre dyke contain no thorogummite phase, but chemical analyses have indicated some traces of thorium content in the sample.
- The Lamprophyre dyke is enriched with LREE whilst red-carbonate veins are depleted in HREE mineralization. Despite of different REE mineralization, both rock type indicate to have enriched with similar process but originate from different source rocks.
- Ytterøy island contains limited distribution of Lamprophyre dyke indicating that the dyke was probably extracted/eroded or was not exposed as per field work observation.
- Occurrence of mineral assemblages in the Ytterøy island are considered to have been occurred due to hydrothermal fluid circulation, influx of external fluid and igneous intrusion of Lamprophyre dyke.

## 6.2 Recommendation (Future work)

- As discussed, limited distribution of Lamprophyre dyke due to continuous extraction, erosion and/ or poorly exposed in the Ytterøy island further investigation to locate their exact position is highly needed. Much focus on locating the igneous intrusion (Lamprophyre dyke) in the Ytterøy island might be a future research work. This can be accomplished using a detailed geological mapping and geophysical methods (i.e. magnetic and gravity) where magnetic mineral and density contrast for rock formations can be investigated.
- According to Kara and Committee (2008) on a report titled "*Thorium as an Energy Source–Opportunities for Norway*", reported that Norway contains high thorium content in the world i.e. 170,000 tonnes and have energy potential ca.100 times greater than all oil extracted to date by Norway. Thus, there is a possibility that the reserve could be hosted in the thorogummite mineral phase due to high Th content than the most known uranium, thorite and huttonite radioactive minerals. Therefore, a detailed investigation of thorogummite distribution and its Th content in the red-carbonate veins will be probable future research topic. This will help to estimate the overall amount and concentration of thorium present in the host rocks and this could be an alternative source of energy in the future.

**Reference**


Bach, W., Jöns, N., & Klein, F. (2013). Metasomatism within the ocean crust *Metasomatism and the Chemical Transformation of Rock* (pp. 253-288): Springer.

Barthel, F., & Tulsidas, H. (2014). Thorium Occurrences, Geological Deposits and Resources.

Blundy, J., & Wood, B. (2003). Mineral-melt partitioning of uranium, thorium and their daughters. *Reviews in Mineralogy and Geochemistry*, 59-123.

Bowden, P. (1985). The geochemistry and mineralization of alkaline ring complexes in Africa (a review). *Journal of African Earth Sciences (1983)*, 17-39.

Burt, D. (1989a). Compositional and phase relations among rare earth element minerals. *Reviews of Mineralogy*, 260-307.

Burt, D. (1989b). Compositional and phase relations among rare earth element minerals. *Reviews of Mineralogy, 21*, 260-307.

Carstens, H. (1961). A post-Caledonian ultrabasic biotite lamprophyre dyke of the Island Ytterøy in the Trondheimsfjord, Norway. *Norg. Geol. Undersøk., 215*, 10-21.

Cocks, L., & Torsvik, T. (2002). Earth geography from 500 to 400 million years ago: a faunal and palaeomagnetic review. *Journal of the Geological Society*, 631-644.

Coward, M. P. (1995). Structural and tectonic setting of the Permo-Triassic basins of northwest Europe. *Geological Society, London, Special Publications, 91*, 7-39.

Cox, S. (2005). Coupling between deformation, fluid pressures, and fluid flow in ore-producing hydrothermal systems at depth in the crust. *Economic Geology*, 39-75.

Dyar, M. D., Gunter, M. E., & Tasa, D. (2008). *Mineralogy and Optical Mineralogy*. Chantilly, VA: Mineralogical Society of America.

Edgar, A. D., & Vukadinovic, D. (1992). Implications of experimental petrology to the evolution of ultrapotassic rocks. *Lithos, 28*(3), 205-220.

Finch, R., & Murakami, T. (1999). Systematics and paragenesis of uranium minerals. *Reviews in Mineralogy, 38*, 91-180.

Foley, S. (1992). Petrological characterization of the source components of potassic magmas: geochemical and experimental constraints. *Lithos, 28*(3), 187-204.

Foley, S. F., Venturelli, G., Green, D. H., & Toscani, L. (1987). The ultrapotassic rocks: characteristics, classification, and constraints for petrogenetic models. *Earth-Science Reviews, 24*(2), 81-134.

Gabrielsen, R., & Ramberg, I. (1979). Fracture patterns in Norway from LANDSAT imagery: results and potential use. *Proceedings, Norwegian Sea Symposium, Tromsø*, 1-28.

Gammons, C., Wood, S., & Williams-Jones, A. (1996). The aqueous geochemistry of the rare earth elements and yttrium: VI. Stability of neodymium chloride complexes from 25 to 300 C. *Geochimica et Cosmochimica Acta, 60*(23), 4615-4630.

Grønlie, A., & Roberts, D. (1989). Resurgent strike-slip duplex development along the Hitra-Snåsa and Verran Faults, Møre-Trøndelag fault zone, Central Norway. *Journal of structural geology, 11*(3), 295-305.

Grønlie, A., & Torsvik, T. H. (1989). On the origin and age of hydrothermal thorium-enriched carbonate veins and breccias in the Møre-Trøndelag Fault Zone, Central Norway. *Norsk Geologisk Tidsskrift, 69*(1), 1-19.

Haas, J. R., Shock, E. L., & Sassani, D. C. (1995). Rare earth elements in hydrothermal systems: estimates of standard partial molal thermodynamic properties of aqueous complexes of the rare earth elements at high pressures and temperatures. *Geochimica et Cosmochimica Acta, 59*(21), 4329-4350.

Hazen, R. M., Ewing, R. C., & Sverjensky, D. A. (2009). Evolution of uranium and thorium minerals. *American Mineralogist, 94*(10), 1293-1311.

Hirtopanu, P., Jakab, G., Andersen, C. J., & Fairhurst, J. R. (2013). Thorite, thorogummite and xenotime-(Y) occurrence in Ditrau alkaline intrusive massif, East Carpathians, Romania. *Proceedings of the Romanian Academy, Series B: Chemistry, Life Sciences and Geoscience, 15*(2), 111-132.

Holland, H. (2003). The geologic history of seawater. *Treatise on geochemistry*, 625.

Kara, M., & Committee, C. o. t. R. (2008). Thorium as an Energy Source–Opportunities for Norway. *Thorium Report Committee, Norway*.

Keppler, H., & Wyllie, P. J. (1990). Role of fluids in transport and fractionation of uranium and thorium in magmatic processes. *Nature*, 531-533.

Korzhinskii, D. (1957). Physico-chemical basement of the mineral parageneses analysis. *Nauka Publ., Moscow*.

Lagat, J. K. e. (2007). Hydrothermal alteration mineralogy in geothermal fields with case examples from Olkaria domes geothermal field, Kenya. *001045504*.

Linnen, R., Samson, I., Williams-Jones, A., & Chakhmouradian, A. (2014). Geochemistry of the rare-earth element, Nb, Ta, Hf, and Zr deposits. *Treatise on geochemistry, 13*, 543-568.

Mitchell, J., & Roberts, D. (1986a). Ages of lamprophyre dykes from Ytterøy and Lerkehaug, near Steinkjer, Central Norwegian caledonides. *Norsk geologisk tidsskrift*, 255-261.

Mitchell, J., & Roberts, D. (1986b). Ages of lamprophyre dykes from Ytterøy and Lerkehaug, near Steinkjer, Central Norwegian caledonides. *Norsk Geologisk Tidsskrift, 66*(4), 255-261.

Nelson, S. A. (Producer). (2016, November, Tuesday). Earth & Environmental Sciences 2110. https://www.google.no/?gfe_rd=cr&ei=ODUtWd-sOu_k8AeKwbKoBQ#q=Earth+%26+Environmental+Sciences+2110+MINERALOGY. Retrieved from http://www.tulane.edu/~sanelson/eens211/

Nixon, P., & Hornung, G. (1973). The carbonatite lavas and tuffs near Fort Portal, western Uganda. *HM Stationery Office*, 41: 168-179.

Oftedahl, C. (1972). A sideritic ironstone of Jurassic age in Beitstadfjorden, Trøndelag. *Norsk Geologisk Tidsskrift, 52*, 123-134.

Petruk, W. (2000). *Applied mineralogy in the mining industry*: Elsevier.

Piilonen, P. C., Rowe, R., Poirier, G., Grice, J. D., & McDonald, A. M. (2014). Discreditation of thorogummite. *The Canadian Mineralogist*, canmin. 1400058.

Pirajno, F. (2009). Hydrothermal processes and wall rock alteration *Hydrothermal Processes and Mineral Systems* (pp. 73-164): Springer.

Pollard, P. (1983). Magmatic and postmagmatic processes in the formation of rocks associated with rare-element deposits. *Trans. Inst. Mining Metal. Sect. B, Applied Earth Sci.*, 1-9.

ROBB, J. (2005). Hydrothermal ore forming processes. *Introduction to ore forming processes. Johannesburg, Black well Publishing Company*, 129-214.

Robert, T. (Producer). (2007, May Saturday). Wikipedia. *Wikipedia*. Retrieved from https://en.wikipedia.org/wiki/File:Euramerica_en.svg

Roberts, D. (1983). Devonian tectonic deformation in the Norwegian Caledonides and its regional perspectives. *Norges geologiske undersøkelse, 380*, 85-96.

Roberts, D., & Gee, D. G. (1985). An introduction to the structure of the Scandinavian Caledonides. *The Caledonide orogen–Scandinavia and related areas*, 55-68.

Roberts, D., & Sturt, B. (1980). Caledonian deformation in Norway. *Journal of the Geological Society, 137*(3), 241-250.

Roberts, D., & Tucker, R. D. (1998). Late Cambrian U-Pb zircon age of a metatrondhjemite from Ytterøya, Trondheimsfjorden, Central Norwegian Caledonides. *Norsk Geologisk Tidsskrift, 78*, 253-258.

Schneider, M. E., & Eggler, D. H. (1984). Compositions of fluids in equilibrium with peridotite: implications for alkaline magmatism-metasomatism.

Slagstad, T., Pin, C., Roberts, D., Kirkland, C. L., Grenne, T., Dunning, G., Sauer, S., & Andersen, T. (2014). Tectonomagmatic evolution of the Early Ordovician suprasubduction-zone ophiolites of the Trondheim Region, Mid-Norwegian Caledonides. *Geological Society, London, Special Publications, 390*(1), 541-561.

Sturt, B., Torsvik, T., & Grønlie, A. (1987). *Dating of hydrothermal alteration-zones and breccias in the Trondheimsfjord region: The Møre-Trøndelag Fault Zone*. Retrieved from Norway:

Tindle, A. (Producer). http://www.open.ac.uk/earth-research/tindle/AGTWebPages/AGTSoft.html. http://www.open.ac.uk/earth-research/tindle/AGTWebPages/AGTSoft.html. Retrieved from http://www.open.ac.uk/earth-research/tindle/AGTWebPages/AGTSoft.html

Torsvik, T. H. (2003). The Rodinia jigsaw puzzle. *Science, 300*(5624), 1379-1381.

Torsvik, T. H., & Van der Voo, R. (2002). Refining Gondwana and Pangea palaeogeography: estimates of Phanerozoic non-dipole (octupole) fields. *Geophysical Journal International, 151*(3), 771-794.

V, D. S., Love, G., & S, J. B. R. (1995). *Quantitative Electron-Probe Microanalysis*. New York: Ellis Horwood Limited.

Van Gosen, B. S., Gillerman, V. S., & Armbrustmacher, T. J. (2009). *Thorium Deposits of the United States-Energy Resources for the Future?* (2330-5703). Retrieved from

Van Staal, C., Dewey, J., Mac Niocaill, C., & McKerrow, W. (1998). The Cambrian-Silurian tectonic evolution of the northern Appalachians and British Caledonides: history of a complex, west and southwest Pacific-type segment of Iapetus. *Geological Society, London, Special Publications, 143*(1), 197-242.

Williams-Jones, A. E., Samson, I. M., & Olivo, G. R. (2000). The genesis of hydrothermal fluorite-REE deposits in the Gallinas Mountains, New Mexico. *Economic Geology, 95*(2), 327-341.

Wolff, F. C. (1976). Geologisk kart over Norge, berggrunnskart Trondheim 1: 250 000. *Geological Survey of Norway*.

Wood, S. A. (1990a). The aqueous geochemistry of the rare-earth elements and yttrium: 2. Theoretical predictions of speciation in hydrothermal solutions to 350 C at saturation water vapor pressure. *Chemical Geology*, *88*(1-2), 99-125.

Wood, S. A. (1990b). The aqueous geochemistry of the rare-earth elements and yttrium: 2. Theoretical predictions of speciation in hydrothermal solutions to 350 C at saturation water vapor pressure. *Chemical Geology*, 99-125.

Yardley, B. W. (2013). The chemical composition of metasomatic fluids in the crust *Metasomatism and the Chemical Transformation of Rock* (pp. 17-51): Springer.

ZharikovF, V. (2007). 9. Metasomatism and metasomatic rocksF. *A classification of metamorphic rocks and glossary of terms. Recommendations of the International Union of Geological Sciences Subcommission on the Systaematics of Metamorphic Rocks*.

Ziegler, P. (1981). Evolution of sedimentary basins in North-West Europe. *Petroleum geology of the continental shelf of north-west Europe*, 3-39.

## Other sources

Geological Survey of Queensland (GSQ), Department of Natural Resources and Mines., 2014. Thorium opportunities in Queensland. [Online] Available at: https://www.dnrm.qld.gov.au/__data/assets/pdf_file/0003/238116/thorium.pdf [Accessed 23 10 2017].

Encyclopedia Britannica, 2009. Thorium (Th) element [Online] Available at: https://www.britannica.com/science/thorium [Accessed 13 November 2017]

# 8. Appendix

# Appendix I: Whole-rock major analyses From ICP – MS

| **Sample No.** | **AM-16-001A** | **AM-16-001B** | **AM-16-002** | **AM-16-003A** | **AM-16-003B** | **AM-16-004** |
|---|---|---|---|---|---|---|
| **Major elements** | | | | | | |
| $SiO_2$ (wt%) | 47.3 | 55.6 | 38.2 | 70.1 | 75.2 | 64.4 |
| $Al_2O_3$ | 5.3 | 4.89 | 11.5 | 8.23 | 5.38 | 7.38 |
| $TiO_2$ | 0.3 | 0.44 | 0.76 | 0.16 | 0.07 | 0.16 |
| $Fe_2O_3$ | 4.79 | 4.42 | 7.42 | 1.73 | 1.84 | 1.86 |
| MnO | 0.11 | 0.09 | 0.13 | 0.03 | 0.03 | 0.04 |
| MgO | 5.16 | 4.88 | 8.52 | 1.33 | 1.45 | 1.71 |
| CaO | 12.9 | 10.75 | 13.45 | 3.35 | 3.9 | 6.94 |
| $Na_2O$ | 0.16 | 0.06 | 2.18 | 0.08 | 0.05 | 0.07 |
| K2O | 4.44 | 4.39 | 3.21 | 7.34 | 4.72 | 6.63 |
| $Cr_2O_3$ | 0.03 | 0.02 | 0.09 | 0.01 | 0.01 | 0.01 |
| $P_2O_5$ | 0.09 | 0.14 | 0.04 | 0.13 | 0.05 | 0.49 |
| BaO | 0.11 | 0.21 | 0.01 | 2.34 | 2.23 | 2.6 |
| SrO | 0.12 | 0.12 | 0.06 | 0.06 | 0.04 | 0.06 |
| LOI | 17.45 | 14.7 | 14.35 | 4.89 | 5.33 | 7.41 |
| **Total** | **98.26** | **100.71** | **99.92** | **99.78** | **100.3** | **99.76** |

| **SAMPLE** | **AM-16-005** | **AM-16-007** | **AM-16-008** | **AM-16-009** | **AM-16-010A** | **AM-16-010B** |
|---|---|---|---|---|---|---|
| $SiO_2$, wt% | 42.7 | 80.9 | 66.6 | 43 | 44.1 | 51.5 |
| $Al_2O_3$ | 10.1 | 8.1 | 4.22 | 6.27 | 7.38 | 6.29 |
| $Fe_2O_3$ | 10.9 | 2.01 | 3.57 | 7.23 | 6.19 | 5.13 |
| CaO | 13.2 | 1.33 | 7.89 | 12.7 | 10.75 | 8.64 |
| MgO | 12.65 | 0.72 | 3.41 | 4.97 | 4.47 | 3.57 |
| $Na_2O$ | 0.34 | 1.63 | 0.07 | 0.11 | 0.1 | 0.08 |
| $K_2O$ | 1.73 | 4.6 | 3.75 | 5.78 | 6.77 | 5.78 |
| $Cr_2O_3$ | 0.11 | 0.01 | 0.02 | 0.02 | 0.02 | 0.01 |
| $TiO_2$ | 2.42 | 0.1 | 0.23 | 0.66 | 0.36 | 0.16 |
| MnO | 0.27 | 0.02 | 0.07 | 0.15 | 0.1 | 0.08 |
| $P_2O_5$ | 0.71 | 0.06 | 0.07 | 0.12 | 0.03 | 0.05 |
| SrO | 0.05 | - | 0.07 | 0.06 | 0.08 | 0.12 |
| BaO | 0.03 | 0.04 | 0.17 | 1.27 | 3.51 | 6.34 |
| LOI | 4.14 | 2.1 | 11.55 | 18.1 | 15.85 | 12.15 |
| **Total** | **99.35** | **101.62** | **101.69** | **100.44** | **99.71** | **99.9** |

# Appendix II: Trace element analyses from ICP – MS

| SAMPLE | AM-16-001A | AM-16-001B | AM-16-002 | AM-16-003A | AM-16-003B | AM-16-004 | AM-16-005 | AM-16-007 | AM-16-008 | AM-16-009 | AM-16-010A | AM-16-010B |
|---|---|---|---|---|---|---|---|---|---|---|---|---|
| Trace element, ppm | | | | | | | | | | | | |
| Ba | 1055 | 1985 | 78.4 | >10000 | >10000 | >10000 | 356 | 382 | 1600 | >10000 | >10000 | >10000 |
| Hf | 0.5 | 0.6 | 1.4 | 1.6 | 1.3 | 1 | 5.5 | 4.9 | 0.4 | 0.9 | 0.4 | 0.4 |
| Rb | 107.5 | 108 | 83.6 | 232 | 130.5 | 167.5 | 154.5 | 104 | 99.1 | 89.7 | 131.5 | 114 |
| Sn | 2 | 1 | 1 | 5 | 8 | 5 | 2 | 1 | 1 | 1 | 1 | 2 |
| Sr | 1095 | 1095 | 524 | 697 | 483 | 712 | 556 | 98.9 | 664 | 617 | 753 | 1090 |
| Ta | 0.2 | 0.2 | 0.1 | <0.1 | 0.1 | 0.1 | 4.2 | 0.3 | 0.2 | 0.1 | 0.1 | 0.1 |
| Th | 669 | 550 | 64.4 | 194 | 665 | 126.5 | 10.45 | 166 | 874 | 103.5 | 171 | 92.1 |
| U | 14.7 | 8.44 | 4.33 | 47.8 | 60 | 46.2 | 2.52 | 3.94 | 6.91 | 7.87 | 7.71 | 5.85 |
| V | 616 | 472 | 168 | 121 | 110 | 111 | 212 | 89 | 408 | 672 | 633 | 433 |
| W | 41 | 44 | 38 | 49 | 33 | 32 | 7 | 60 | 41 | 67 | 44 | 26 |
| Zr | 20 | 25 | 48 | 68 | 50 | 47 | 226 | 178 | 17 | 34 | 19 | 10 |
| As | 88.5 | 101.5 | 38.8 | 43.7 | 26.6 | 43.8 | 3.2 | 19.5 | 56.5 | 143 | 38.6 | 75.4 |
| Bi | <0.01 | 0.01 | 0.01 | 0.01 | <0.01 | 0.01 | 0.04 | 0.01 | <0.01 | 0.01 | 0.04 | 0.11 |
| Hg | 0.103 | 0.12 | 0.027 | 0.504 | 0.512 | 0.321 | 0.006 | 0.013 | 0.058 | 0.049 | 0.074 | 0.07 |
| In | 0.023 | 0.023 | 0.025 | 0.018 | 0.018 | 0.011 | 0.015 | 0.028 | 0.02 | 0.053 | 0.034 | 0.021 |
| Re | 0.001 | 0.001 | 0.001 | <0.001 | 0.001 | <0.001 | <0.001 | <0.001 | 0.001 | <0.001 | <0.001 | 0.001 |
| Sb | 10.2 | 20.3 | 3.7 | 43.1 | 91.1 | 37.7 | 0.95 | 3.64 | 8.43 | 13.15 | 5.34 | 5.81 |
| Se | 1.9 | 1.3 | 0.8 | 0.5 | 1.6 | 1 | 0.3 | 0.3 | 1.2 | 1.3 | 1.3 | 0.8 |
| Te | 0.02 | 0.01 | <0.01 | 0.01 | 0.04 | 0.01 | 0.03 | 0.01 | <0.01 | <0.01 | 0.02 | 0.01 |
| Tl | 2.81 | 2.16 | 0.99 | 1.97 | 2.46 | 1.32 | 0.96 | 0.69 | 0.7 | 2.76 | 0.52 | 1.08 |
| Ag | 1 | 0.8 | 0.6 | 0.6 | <0.5 | 1 | 0.7 | <0.5 | <0.5 | 0.7 | 0.9 | 1.3 |
| Cd | <0.5 | <0.5 | <0.5 | <0.5 | <0.5 | <0.5 | <0.5 | <0.5 | <0.5 | <0.5 | <0.5 | <0.5 |
| Co | 18 | 18 | 45 | 12 | 9 | 8 | 49 | 10 | 14 | 15 | 9 | 6 |
| Cu | 25 | 41 | 58 | 9 | 12 | 7 | <1 | 7 | 13 | 18 | 19 | 7 |
| Li | 10 | <10 | 50 | 30 | 40 | 40 | 40 | <10 | <10 | 10 | 10 | 10 |
| Mo | 2 | 11 | <1 | 69 | 141 | 64 | 2 | 1 | 5 | 1 | 1 | 3 |
| Ni | 53 | 69 | 310 | 25 | 17 | 22 | 260 | 5 | 33 | 27 | 15 | 7 |
| Pb | 79 | 227 | 6 | 391 | 983 | 579 | 22 | 8 | 150 | 21 | 155 | 262 |
| Sc | 30 | 25 | 24 | 7 | 7 | 8 | 33 | 5 | 19 | 32 | 26 | 17 |
| Zn | 23 | 30 | 45 | 162 | 183 | 68 | 125 | 16 | 32 | 41 | 54 | 32 |

# Appendix III. Analyses of mineral chemistry from EPMA

| SAMPLE AM-16-001A | | | | | |
|---|---|---|---|---|---|
| **Point** | **1** | **2** | **3** | **4** | **5** |
| **Mineral name** | **Dolomite** | **Ankerite** | **Thorogummite** | **Microcline** | **Quartz** |
| $SiO_2$, wt% | 0 | 0 | 13.24 | 59.03 | 98.10 |
| $Al_2O_3$ | 0.01 | 0 | 0.07 | 1.82 | 0.14 |
| $TiO_2$ | 0.04 | 0 | 0 | 0 | 0 |
| FeO | 5.90 | 13.18 | 2.34 | 0.11 | 0 |
| MnO | 0.34 | 0.31 | 0 | 0.01 | 0 |
| MgO | 17.35 | 12.13 | 0 | 0 | 0 |
| CaO | 34.67 | 30.12 | 2.88 | 0 | 0.03 |
| $Na_2O$ | 0.02 | 0.06 | 0 | 0.19 | 0 |
| $K_2O$ | 0 | 0.01 | 0.02 | 14.21 | 0.04 |
| $P_2O_5$ | 0.01 | 0.04 | 3.69 | 0 | 0.02 |
| BaO | 0 | 0 | 0 | 0 | 0.02 |
| $ThO_2$ | 0.02 | 0 | 75.46 | 0.96 | 0.11 |
| **Total** | **58.35** | **55.84** | **97.71** | **76.32** | **98.46** |
| **Trace** | | | | | |
| Th | 510 | 1530 | 623410 | 3090 | 1340 |
| U | 780 | 530 | 18830 | 0 | 30 |
| Ba | 0 | 0 | 0 | 0 | 0 |
| F | 0 | 11920 | 3290 | 0 | 140 |
| La | 580 | 0 | 0 | 0 | 0 |
| Ce | 0 | 0 | 810 | 1560 | 560 |
| Pr | 0 | 0 | 0 | 0 | 0 |
| Nd | 70 | 130 | 130 | 370 | 0 |
| Sm | 0 | 0 | 1470 | 160 | 0 |
| Eu | 230 | 0 | 0 | 0 | 0 |
| Gd | 700 | 0 | 1780 | 0 | 530 |
| Tb | 310 | 0 | 0 | 180 | 430 |
| Dy | 1560 | 0 | 1120 | 1510 | 20 |
| Ho | 0 | 80 | 1270 | 0 | 0 |
| Er | 230 | 1000 | 0 | 2150 | 0 |
| Tm | 400 | 200 | 0 | 0 | 300 |
| Yb | 160 | 0 | 0 | 2500 | 0 |
| Lu | 550 | 190 | 0 | 240 | 0 |

| SAMPLE AM-16-001B | | | | | | |
|---|---|---|---|---|---|---|
| **Point** | 1 | 2 | 3 | 4 | 5 | 6 |
| **Mineral name** | **Thorogummite** | **Fluorite** | **Quartz** | **Microcline** | **Ankerite** | **Dolomite** |
| $SiO_2$, wt% | 15.25 | 0 | 99.71 | 63.76 | 0 | 0 |
| $Al_2O_3$ | 0.08 | 0.03 | 0.01 | 17.98 | 0.03 | 0.10 |
| $TiO_2$ | 0 | 0 | 0.02 | 0 | 0 | 0 |
| FeO | 1.16 | 0.02 | 0.00 | 0.42 | 1.56 | 1.62 |
| MnO | 0.09 | 0.01 | 0 | 0 | 0.33 | 0.29 |
| MgO | 0.04 | 0 | 0 | 0 | 0.43 | 0.51 |
| CaO | 2.96 | 78.09 | 0.18 | 0 | 61.63 | 60.83 |
| $Na_2O$ | 0 | 0.05 | 0.02 | 0.17 | 0 | 0.03 |
| $K_2O$ | 0 | 0.01 | 0 | 18.13 | 0 | 0.22 |
| $P_2O_5$ | 1.94 | 0.14 | 0 | 0.06 | 0.07 | 0.02 |
| BaO | 0 | 0 | 0.04 | 0 | 0 | 0 |
| $ThO_2$ | 77.21 | 0.22 | 0 | 0 | 0.07 | 0.10 |
| **Total** | **92.46** | **79.46** | **99.98** | **100.53** | **64.13** | **63.71** |
| **Trace elements (ppm)** | | | | | | |
| Th | 674160 | 1980 | 0 | 0 | 660 | 920 |
| U | 18430 | 0 | 790 | 0 | 300 | 190 |
| Ba | 0 | 0 | 370 | 0 | 0 | 0 |
| F | 1050 | 13730 | 140 | 0 | 280 | 280 |
| La | 790 | 0 | 560 | 0 | 640 | 0 |
| Ce | 3010 | 0 | 1060 | 0 | 0 | 940 |
| Pr | 0 | 80 | 0 | 0 | 0 | 0 |
| Nd | 960 | 60 | 0 | 0 | 0 | 270 |
| Sm | 3300 | 0 | 0 | 180 | 370 | 0 |
| Eu | 0 | 300 | 0 | 0 | 0 | 480 |
| Gd | 4690 | 130 | 470 | 360 | 0 | 0 |
| Tb | 0 | 680 | 0 | 0 | 560 | 410 |
| Dy | 1530 | 0 | 450 | 0 | 1810 | 1340 |
| Ho | 1770 | 0 | 0 | 320 | 0 | 0 |
| Er | 180 | 0 | 20 | 0 | 0 | 940 |
| Tm | 300 | 0 | 0 | 0 | 0 | 520 |
| Yb | 120 | 0 | 0 | 0 | 0 | 360 |
| Lu | 0 | 0 | 0 | 480 | 350 | 0 |

| SAMPLE AM-16-002 | | | | |
|---|---|---|---|---|
| **Point** | **1** | **2** | **3** | **4** |
| **Mineral name** | **Epidote/Clinozoisite** | **Albite** | **Fluorite** | **Microcline** |
| $SiO_2$, wt% | 38.79 | 68.89 | 0 | 66.71 |
| $Al_2O_3$ | 26.47 | 19.80 | 0.08 | 18.60 |
| $TiO_2$ | 0.16 | 0 | 0 | 0.04 |
| FeO | 6.23 | 0.20 | 0.00 | 0.1 |
| MnO | 0.11 | 0.02 | 0 | 0.02 |
| MgO | 0.02 | 0.11 | 0.05 | 0.06 |
| CaO | 23.82 | 0.17 | 79.19 | 0 |
| $Na_2O$ | 0.02 | 11.21 | 0.04 | 0.22 |
| $K_2O$ | 0.04 | 0.07 | 0.01 | 11.51 |
| $P_2O_5$ | 0.03 | 0 | 0.11 | 0 |
| BaO | 0.08 | 0.10 | 0 | 0 |
| $ThO_2$ | 0.04 | 0 | 0.04 | 0 |
| **Total** | **95.82** | **100.56** | **79.52** | **97.27** |
| **Trace Element, ppm** | | | | |
| Th | 0 | 0 | 1300 | 570 |
| U | 720 | 420 | 140 | 360 |
| Ba | 0 | 0 | 0 | 0 |
| F | 150 | 0 | 13240 | 0 |
| La | 0 | 0 | 0 | 480 |
| Ce | 0 | 500 | 0 | 0 |
| Pr | 0 | 20 | 0 | 0 |
| Nd | 0 | 0 | 0 | 130 |
| Sm | 70 | 290 | 0 | 560 |
| Eu | 0 | 200 | 0 | 0 |
| Gd | 0 | 120 | 520 | 20 |
| Tb | 0 | 0 | 600 | 0 |
| Dy | 590 | 260 | 100 | 1420 |
| Ho | 470 | 0 | 490 | 0 |
| Er | 0 | 0 | 0 | 950 |
| Tm | 0 | 250 | 700 | 0 |
| Yb | 0 | 0 | 670 | 0 |
| Lu | 0 | 410 | 0 | 490 |

| SAMPLE AM-16-003A | | | | | | |
|---|---|---|---|---|---|---|
| **Point.** | **1** | **2** | **3** | **4** | **5** | **6** |
| **Mineral name** | **Ba-REE Carbonate** | **Thorogummite** | **Dolomite** | **Microcline** | **Quartz** | **Ankerite** |
| $SiO_2$, wt% | 0 | 14.40 | 0.22 | 65.53 | 99.75 | 0.02 |
| $Al_2O_3$ | 0.11 | 0.12 | 0.32 | 18.41 | 0.09 | 0 |
| $TiO_2$ | 5.70 | 0 | 0.04 | 0 | 0 | 0.02 |
| FeO | 0 | 0.84 | 0.74 | 0.02 | 0.02 | 14.15 |
| MnO | 0 | 0 | 0.03 | 0 | 0 | 0.35 |
| MgO | 0 | 0.05 | 24.17 | 0 | 0 | 11.77 |
| CaO | 0.07 | 2.15 | 29.54 | 0 | 0 | 28.75 |
| $Na_2O$ | 0.24 | 0 | 0.17 | 0.20 | 0.00 | 0.20 |
| $K_2O$ | 0.02 | 0 | 0.14 | 16.27 | 0.04 | 0.03 |
| $P_2O_5$ | 0.0 | 1.83 | 0.03 | 0.02 | 0.03 | 0.03 |
| BaO | 67.46 | 0.61 | 0.04 | 0.02 | 0 | 0 |
| $ThO_2$ | 0.01 | 72.60 | 0.03 | 0.03 | 0.03 | 0.07 |
| **Total** | **73.60** | **92.62** | **55.46** | **100.49** | **99.97** | **55.39** |
| **Trace Element, ppm** | | | | | | |
| Th | 0 | 623930 | 0 | 0 | 0 | 390 |
| U | 0 | 23800 | 0 | 0 | 180 | 230 |
| Ba | 577760 | 7370 | 160 | 0 | 680 | 0 |
| F | 220 | 800 | 200 | 130 | 0 | 0 |
| La | 0 | 950 | 0 | 0 | 0 | 0 |
| Ce | 166120 | 11590 | 0 | 0 | 740 | 660 |
| Pr | 0 | 320 | 0 | 0 | 0 | 50 |
| Nd | 0 | 2980 | 180 | 230 | 0 | 0 |
| Sm | 0 | 8330 | 70 | 0 | 0 | 0 |
| Eu | 210 | 0 | 690 | 160 | 0 | 0 |
| Gd | 0 | 8720 | 0 | 0 | 0 | 0 |
| Tb | 0 | 0 | 450 | 0 | 850 | 460 |
| Dy | 0 | 3010 | 0 | 280 | 0 | 610 |
| Ho | 80 | 3250 | 0 | 700 | 660 | 0 |
| Er | 2430 | 1460 | 0 | 0 | 0 | 750 |
| Tm | 0 | 0 | 0 | 0 | 160 | 410 |
| Yb | 1520 | 570 | 770 | 0 | 0 | 0 |
| Lu | 540 | 70 | 220 | 1580 | 980 | 0 |

| SAMPLE AM-16-003B | | | |
|---|---|---|---|
| **Point** | 1 | 2 | 3 |
| **Mineral name** | **Quartz** | **Fluorapatite** | **Microcline** |
| $SiO_2$, wt% | 99.84 | 0.11 | 64.69 |
| $Al_2O_3$ | 0.04 | 0.20 | 17.93 |
| $TiO_2$ | 0 | 0.08 | 0.03 |
| FeO | 0 | 0.06 | 0.63 |
| MnO | 0.02 | 0 | 0.02 |
| MgO | 0 | 0.02 | 0.01 |
| CaO | 0.01 | 55.97 | 0 |
| $Na_2O$ | 0.01 | 0 | 0.20 |
| $K_2O$ | 0.06 | 0.26 | 18.52 |
| $P_2O_5$ | 0 | 42.69 | 0.06 |
| BaO | 0.01 | 0 | 0.10 |
| $ThO_2$ | 0.013 | 0.056 | 0 |
| **Total** | **100.47** | **102.13** | **102.43** |
| **Trace element (ppm)** | | | |
| Th | 120 | 490 | 0 |
| U | 0 | 670 | 0 |
| Ba | 80 | 0 | 890 |
| F | 0 | 38330 | 40 |
| La | 160 | 50 | 110 |
| Ce | 0 | 0 | 160 |
| Pr | 20 | 0 | 150 |
| Nd | 80 | 80 | 0 |
| Sm | 640 | 550 | 0 |
| Eu | 770 | 180 | 0 |
| Gd | 0 | 0 | 80 |
| Tb | 0 | 410 | 0 |
| Dy | 0 | 0 | 0 |
| Ho | 830 | 0 | 990 |
| Er | 580 | 590 | 0 |
| Tm | 0 | 1380 | 520 |
| Yb | 840 | 0 | 30 |
| Lu | 290 | 2510 | 220 |

| SAMPLE AM-16-004 | | | | | |
|---|---|---|---|---|---|
| **Sample No.** | **1** | **2** | **3** | **4** | **5** |
| **Mineral name** | **Fluorapatite** | **Microcline** | **Quartz** | **Ankerite** | **Ba-REE Carbonate** |
| $SiO_2$, wt% | 0 | 65.13 | 99.62 | 0 | 0.10 |
| $Al_2O_3$ | 0 | 18.68 | 0.05 | 0.03 | 0.07 |
| $TiO_2$ | 0.06 | 0.07 | 0 | 0 | 5.74 |
| FeO | 0.84 | 0.13 | 0.02 | 6.06 | 0.05 |
| MnO | 0.03 | 0 | 0.01 | 0.11 | 0 |
| MgO | 0.24 | 0.02 | 0 | 18.93 | 0 |
| CaO | 50.48 | 0 | 0 | 32.74 | 0 |
| $Na_2O$ | 0.27 | 0.08 | 0 | 0.07 | 0.16 |
| $K_2O$ | 0 | 16.84 | 0.05 | 0 | 0.00 |
| $P_2O_5$ | 34.32 | 0 | 0 | 0 | 0.02 |
| BaO | 0 | 0 | 0 | 0 | 67.77 |
| $ThO_2$ | 0 | 0.01 | 0 | 0.01 | 0 |
| **Total** | **86.21** | **100.95** | **99.75** | **57.95** | **73.90** |
| **Trace element, ppm** | | | | | |
| Th | 0 | 610 | 0 | 0 | 410 |
| U | 160 | 700 | 0 | 140 | 0 |
| Ba | 0 | 0 | 0 | 1170 | 580040 |
| F | 70 | 280 | 0 | 0 | 120 |
| La | 690 | 0 | 0 | 0 | 0 |
| Ce | 0 | 0 | 190 | 1250 | 164270 |
| Pr | 0 | 140 | 0 | 130 | 0 |
| Nd | 0 | 30 | 270 | 0 | 0 |
| Sm | 510 | 290 | 200 | 0 | 0 |
| Eu | 0 | 0 | 220 | 0 | 710 |
| Gd | 0 | 210 | 0 | 0 | 0 |
| Tb | 0 | 550 | 0 | 720 | 820 |
| Dy | 1850 | 0 | 220 | 1530 | 0 |
| Ho | 0 | 0 | 80 | 0 | 0 |
| Er | 0 | 0 | 1490 | 490 | 1610 |
| Tm | 0 | 20 | 610 | 0 | 940 |
| Yb | 0 | 230 | 0 | 790 | 0 |
| Lu | 0 | 110 | 720 | 90 | 0 |

| SAMPLE AM-16-005 | | | | |
|---|---|---|---|---|
| **Point** | **1** | **2** | **3** | **4** |
| **Mineral name** | **Clinozoisite** | **Magnesiohornblende** | **Quartz** | **Ba-REE Carbonate** |
| $SiO_2$, wt% | 26.40 | 37.74 | 97.68 | 1.52 |
| $Al_2O_3$ | 22.52 | 5.27 | 0.69 | 0.14 |
| $TiO_2$ | 0.10 | 0.13 | 0.09 | 4.77 |
| FeO | 11.96 | 7.68 | 0.42 | 0.49 |
| MnO | 0.13 | 0.26 | 0.02 | 0.00 |
| MgO | 0.11 | 19.00 | 0.56 | 0.00 |
| CaO | 23.45 | 12.04 | 0.36 | 0.22 |
| $Na_2O$ | 0.00 | 0.78 | 0.07 | 0.33 |
| $K_2O$ | 0.05 | 0.32 | 0.10 | 0.08 |
| $P_2O_5$ | 0.04 | 0.03 | 0.00 | 0.08 |
| BaO | 0.08 | 0.00 | 0.06 | 57.08 |
| $ThO_2$ | 0.04 | 0.02 | 0.00 | 0.06 |
| **Total** | **84.90** | **83.25** | **100.05** | **64.78** |
| **Trace element, ppm** | | | | |
| Th | 170 | 230 | 270 | 160 |
| U | 70 | 250 | 0 | 0 |
| Ba | 110 | 80 | 220 | 0 |
| F | 0 | 0 | 0 | 0 |
| La | 0 | 0 | 0 | 0 |
| Ce | 810 | 0 | 880 | 160 |
| Pr | 0 | 200 | 50 | 30 |
| Nd | 70 | 70 | 20 | 0 |
| Sm | 0 | 250 | 0 | 0 |
| Eu | 0 | 0 | 20 | 0 |
| Gd | 0 | 280 | 280 | 0 |
| Tb | 690 | 450 | 0 | 790 |
| Dy | 0 | 1890 | 210 | 690 |
| Ho | 0 | 160 | 0 | 0 |
| Er | 0 | 1240 | 0 | 0 |
| Tm | 0 | 0 | 0 | 0 |
| Yb | 0 | 0 | 0 | 850 |
| Lu | 500 | 770 | 0 | 280 |

| | SAMPLE AM-16-007 | | | | |
|---|---|---|---|---|---|
| **Point** | 1 | 2 | 3 | 4 | 5 |
| **Mineral name** | **Perovskite** | **Fluorapatite** | **Microcline** | **Quartz** | **Thorogummite** |
| $SiO_2$, wt% | 0.83 | 2.04 | 64.71 | 96.8 | 15.65 |
| $Al_2O_3$ | 0.30 | 1.01 | 17.19 | 0 | 0.21 |
| $TiO_2$ | 110.75 | 1.77 | 0 | 0 | 0 |
| FeO | 0.25 | 5.69 | 0.17 | 0 | 4.24 |
| MnO | 0.00 | 0.01 | 0.01 | 0 | 0.05 |
| MgO | 0.04 | 0.41 | 0 | 0 | 0.04 |
| CaO | 2.22 | 47.86 | 0 | 0 | 1.67 |
| $Na_2O$ | 0.15 | 0.23 | 0.10 | 0 | 0.12 |
| $K_2O$ | 0.40 | 0.49 | 16.86 | 0 | 0.06 |
| $P2O_5$ | 3.18 | 39.16 | 0.03 | 0 | 2.42 |
| BaO | 4.12 | 0.13 | 0 | 0 | 0 |
| $ThO_2$ | 0.04 | 0.47 | 0.04 | 0 | 61.74 |
| **Total** | **122.26** | **99.26** | **99.10** | **96.88** | **86.19** |
| **Trace element, ppm** | | | | | |
| Th | 340 | 4100 | 360 | 0 | 552740 |
| U | 0 | 590 | 0 | 0 | 14150 |
| Ba | 36470 | 1110 | 1020 | 0 | 0 |
| F | 1240 | 29770 | 0 | 0 | 2010 |
| La | 0 | 200 | 260 | 0 | 190 |
| Ce | 0 | 680 | 0 | 0 | 4620 |
| Pr | 0 | 220 | 40 | 0 | 0 |
| Nd | 0 | 0 | 270 | 50 | 960 |
| Sm | 0 | 280 | 0 | 60 | 690 |
| Eu | 210 | 530 | 40 | 260 | 0 |
| Gd | 350 | 0 | 0 | 1040 | 2550 |
| Tb | 460 | 720 | 0 | 280 | 0 |
| Dy | 0 | 0 | 0 | 470 | 5240 |
| Ho | 0 | 400 | 0 | 0 | 1250 |
| Er | 280 | 0 | 740 | 0 | 0 |
| Tm | 150 | 0 | 440 | 0 | 1320 |
| Yb | 0 | 830 | 90 | 690 | 4170 |
| Lu | 270 | 260 | 340 | 1020 | 1090 |

| SAMPLE AM-16-008 | | | | | | |
|---|---|---|---|---|---|---|
| **Point** | 1 | 2 | 3 | 4 | 5 | 6 |
| **Mineral name** | **Fluorite** | **Calcite** | **Microcline** | **Quartz** | **Thorogummite** | **Dolomite** |
| $SiO_2$, wt% | 0 | 0 | 65.92 | 97.51 | 11.80 | 0 |
| $Al_2O_3$ | 0 | 0 | 17.10 | 0.05 | 0.20 | 0.04 |
| $TiO_2$ | 0 | 0 | 0 | 0.00 | 0 | 0.05 |
| FeO | 0.01 | 0.14 | 0.03 | 0 | 7.44 | 0 |
| MnO | 0 | 0.44 | 0.03 | 0.01 | 0 | 0.20 |
| MgO | 0 | 0.13 | 0 | 0.01 | 0.07 | 14.84 |
| CaO | 82.67 | 64.76 | 0 | 0.77 | 0.00 | 31.72 |
| $Na_2O$ | 0.06 | 0.01 | 0.04 | 0.00 | 0.03 | 0.08 |
| K2O | 0.04 | 0.02 | 17.52 | 0.12 | 0.06 | 0.02 |
| $P_2O_5$ | 0 | 0 | 0.03 | 0 | 2.30 | 0.03 |
| BaO | 0.05 | 0.13 | 0.01 | 0.14 | 0 | 0.02 |
| $ThO_2$ | 0.05 | 0 | 0.02 | 0.01 | 58.96 | 0.02 |
| **Total** | **82.87** | **65.62** | **100.69** | **98.62** | **80.86** | **47.01** |
| **Trace element (ppm)** | | | | | | |
| Th | 450 | 0 | 180 | 90 | 533890 | 200 |
| U | 500 | 620 | 0 | 50 | 16060 | 0 |
| Ba | 410 | 1090 | 110 | 1190 | 0 | 150 |
| F | 95200 | 110 | 200 | 290 | 1220 | 150 |
| La | 0 | 0 | 0 | 0 | 0 | 50 |
| Ce | 300 | 960 | 0 | 0 | 5320 | 330 |
| Pr | 0 | 0 | 0 | 0 | 0 | 0 |
| Nd | 310 | 0 | 180 | 0 | 880 | 0 |
| Sm | 0 | 0 | 0 | 70 | 5960 | 0 |
| Eu | 0 | 0 | 0 | 630 | 0 | 0 |
| Gd | 0 | 0 | 0 | 0 | 4490 | 300 |
| Tb | 580 | 0 | 510 | 0 | 0 | 0 |
| Dy | 540 | 1690 | 0 | 100 | 3150 | 1120 |
| Ho | 1210 | 0 | 0 | 0 | 2520 | 0 |
| Er | 340 | 0 | 0 | 240 | 0 | 1460 |
| Tm | 0 | 0 | 0 | 60 | 390 | 120 |
| Yb | 380 | 800 | 60 | 910 | 630 | 520 |
| Lu | 0 | 0 | 240 | 40 | 0 | 280 |

| SAMPLE AM-16-009 | | | |
|---|---|---|---|
| **Point** | **1** | **2** | **3** |
| **Mineral name** | **Thorogummite** | **Ankerite** | **Ba-REE Carbonate** |
| $SiO_2$, wt% | 10.30 | 0 | 0 |
| $Al_2O_3$ | 0.13 | 0.02 | 0.19 |
| $TiO_2$ | 0.03 | 0 | 5.58 |
| FeO | 4.26 | 11.17 | 0 |
| MnO | 0 | 0.359 | 0 |
| MgO | 0.06 | 12.96 | 0 |
| CaO | 1.74 | 27.68 | 0 |
| $Na_2O$ | 0 | 0.1 | 0.31 |
| $K_2O$ | 0 | 0 | 0.02 |
| $P_2O_5$ | 2.86 | 0 | 0.03 |
| BaO | 0 | 0.13 | 66.45 |
| $ThO_2$ | 70.97 | 0 | 0 |
| **Total** | **90.35** | **52.43** | **72.57** |
| **Trace element, ppm** | | | |
| Th | 100940 | 710 | 430 |
| U | 3460 | 0 | 1220 |
| Ba | 0 | 990 | 574250 |
| F | 1620 | 0 | 0 |
| La | 670 | 110 | 0 |
| Ce | 1790 | 0 | 153070 |
| Pr | 10 | 0 | 0 |
| Nd | 410 | 0 | 0 |
| Sm | 1930 | 230 | 0 |
| Eu | 0 | 0 | 0 |
| Gd | 0 | 0 | 0 |
| Tb | 270 | 0 | 0 |
| Dy | 1580 | 2760 | 0 |
| Ho | 0 | 0 | 0 |
| Er | 0 | 0 | 0 |
| Tm | 0 | 750 | 500 |
| Yb | 130 | 140 | 0 |
| Lu | 0 | 20 | 1790 |

| SAMPLE AM-16-010A | | | | |
|---|---|---|---|---|
| **Point** | **1** | **2** | **3** | **4** |
| **Mineral name** | **Ba-REE Carbonate** | **Microcline** | **Quartz** | **Ankerite** |
| $SiO_2$, wt% | 0 | 64.64 | 96.24 | 0 |
| $Al_2O_3$ | 0.08 | 18.32 | 0.89 | 0.05 |
| $TiO_2$ | 5.40 | 0.01 | 0 | 0.04 |
| FeO | 0.01 | 1.34 | 0.02 | 5.32 |
| MnO | 0 | 0.04 | 0 | 0.16 |
| MgO | 0.01 | 0.05 | 0.05 | 20.46 |
| CaO | 0.04 | 0 | 0.1 | 33.56 |
| $Na_2O$ | 0.27 | 0.07 | 0.04 | 0.00 |
| $K_2O$ | 0.03 | 15.00 | 0.08 | 0.08 |
| $P_2O_5$ | 0 | 0.03 | 0.01 | 0 |
| BaO | 66.72 | 0.03 | 0 | 0.12 |
| $ThO_2$ | 0 | 0.04 | 0 | 0 |
| **Total** | **72.55** | **99.56** | **97.43** | **59.78** |
| **Trace element, ppm** | | | | |
| Th | 380 | 1270 | 0 | 90 |
| U | 170 | 840 | 0 | 0 |
| Ba | 563940 | 2670 | 350 | 590 |
| F | 0 | 0 | 0 | 220 |
| La | 0 | 0 | 0 | 180 |
| Ce | 153150 | 920 | 70 | 50 |
| Pr | 0 | 0 | 0 | 0 |
| Nd | 0 | 0 | 150 | 100 |
| Sm | 0 | 0 | 0 | 90 |
| Eu | 850 | 900 | 0 | 250 |
| Gd | 90 | 0 | 320 | 80 |
| Tb | 800 | 1650 | 290 | 0 |
| Dy | 0 | 40 | 0 | 0 |
| Ho | 0 | 0 | 0 | 380 |
| Er | 1890 | 400 | 0 | 200 |
| Tm | 1170 | 0 | 0 | 0 |
| Yb | 770 | 0 | 560 | 0 |
| Lu | 830 | 320 | 750 | 0 |

| SAMPLE AM-16-010B | | | | |
|---|---|---|---|---|
| **Point** | 1 | 2 | 3 | 4 |
| **Mineral name** | **Ankerite** | **Microcline** | **Quartz** | **Ba-REE Carbonate** |
| $SiO_2$, wt% | 0 | 65.74 | 98.66 | 0.45 |
| $Al_2O_3$ | 0.08 | 17.19 | 0 | 0.45 |
| $TiO_2$ | 0.03 | 0.07 | 0 | 4.63 |
| FeO | 10.42 | 0.18 | 0.02 | 0.03 |
| MnO | 0.28 | 0.02 | 0.00 | 0 |
| MgO | 14.36 | 0 | 0 | 0.04 |
| CaO | 28.88 | 0 | 0 | 0.08 |
| $Na_2O$ | 0.12 | 0.08 | 0 | 0.22 |
| $K_2O$ | 14.36 | 17.41 | 0.02 | 0.05 |
| $P_2O_5$ | 0.02 | 0.13 | 0.09 | 0 |
| BaO | 0.28 | 0 | 0.07 | 62.79 |
| $ThO_2$ | 0 | 0 | 0 | 0.08 |
| **Total** | **68.81** | **100.83** | **98.86** | **68.82** |
| **Trace element (ppm)** | | | | |
| Th | 0 | 20 | 0 | 730 |
| U | 130 | 0 | 650 | 0 |
| Ba | 2500 | 0 | 580 | 575450 |
| F | 310 | 380 | 50 | 0 |
| La | 0 | 0 | 790 | 0 |
| Ce | 1720 | 0 | 60 | 169600 |
| Pr | 0 | 0 | 0 | 0 |
| Nd | 0 | 290 | 0 | 190 |
| Sm | 0 | 0 | 570 | 0 |
| Eu | 0 | 520 | 130 | 1040 |
| Gd | 0 | 60 | 0 | 230 |
| Tb | 290 | 570 | 300 | 430 |
| Dy | 1410 | 0 | 950 | 540 |
| Ho | 0 | 0 | 290 | 0 |
| Er | 0 | 0 | 0 | 1410 |
| Tm | 0 | 0 | 890 | 0 |
| Yb | 390 | 0 | 0 | 1390 |
| Lu | 730 | 260 | 60 | 0 |

# Appendix IV. Analyses of mineral chemistry from XRD

160467: AM-16-001A

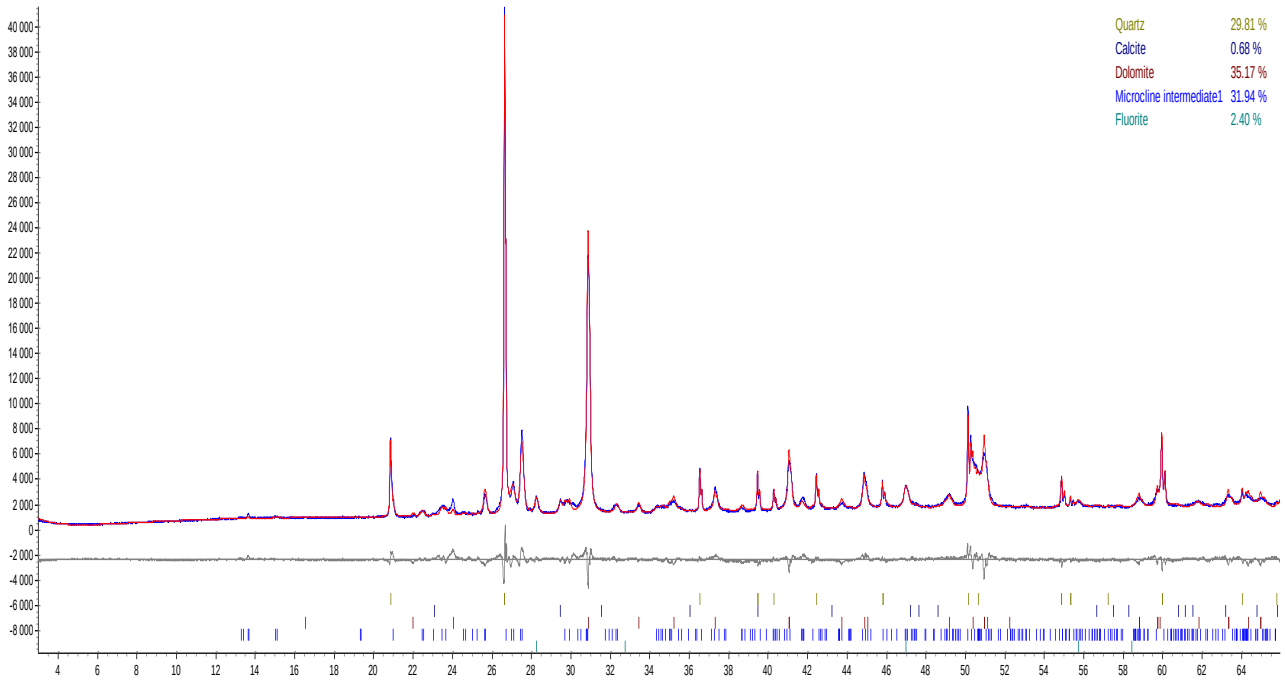


160468: AM-16-001B

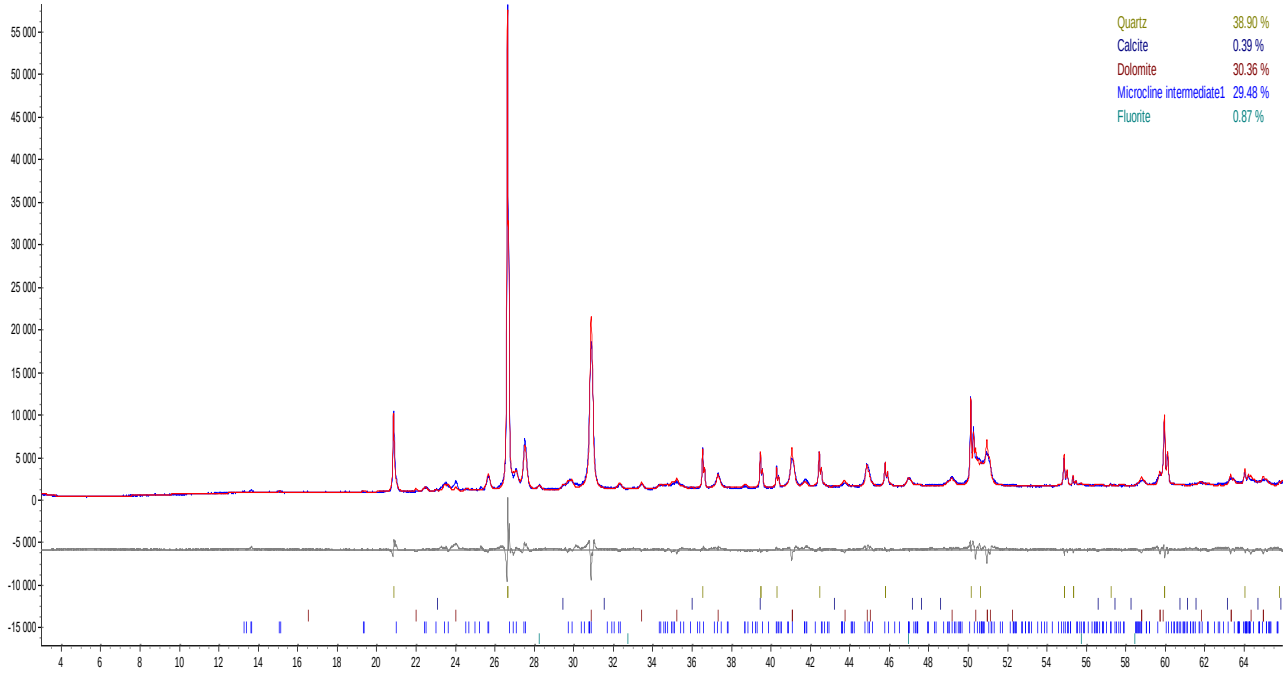

160469: AM-16-002

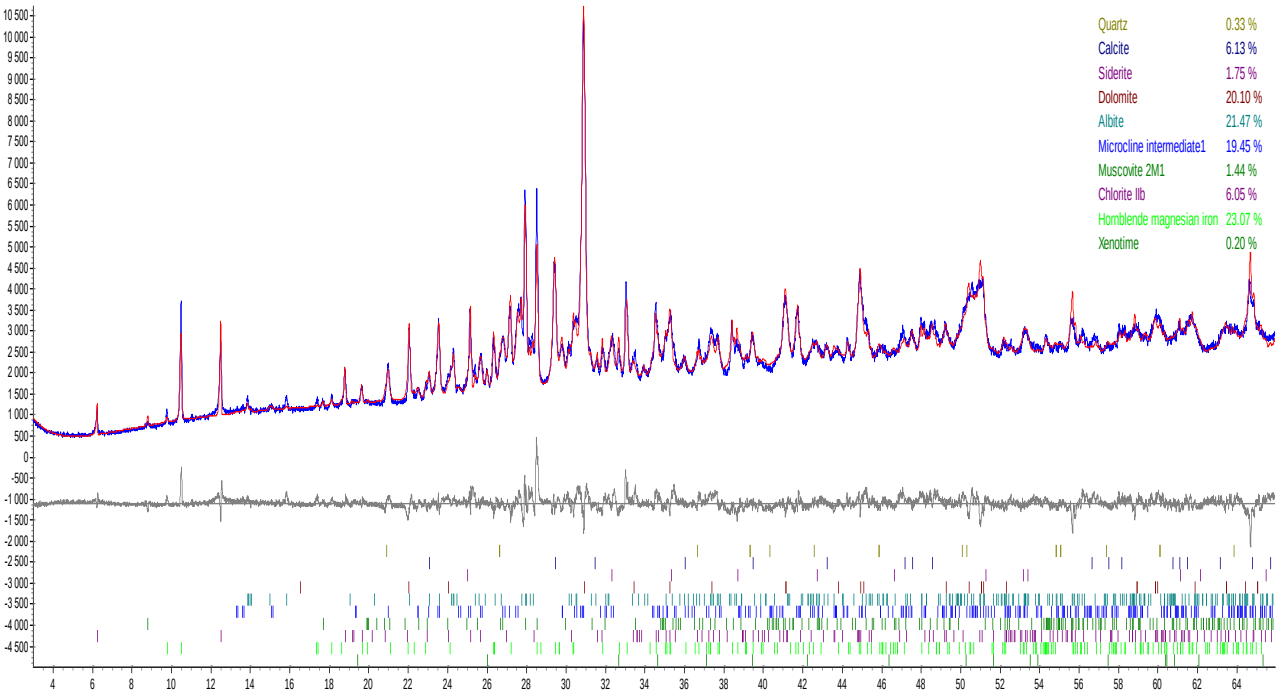


160470: AM-16-003A

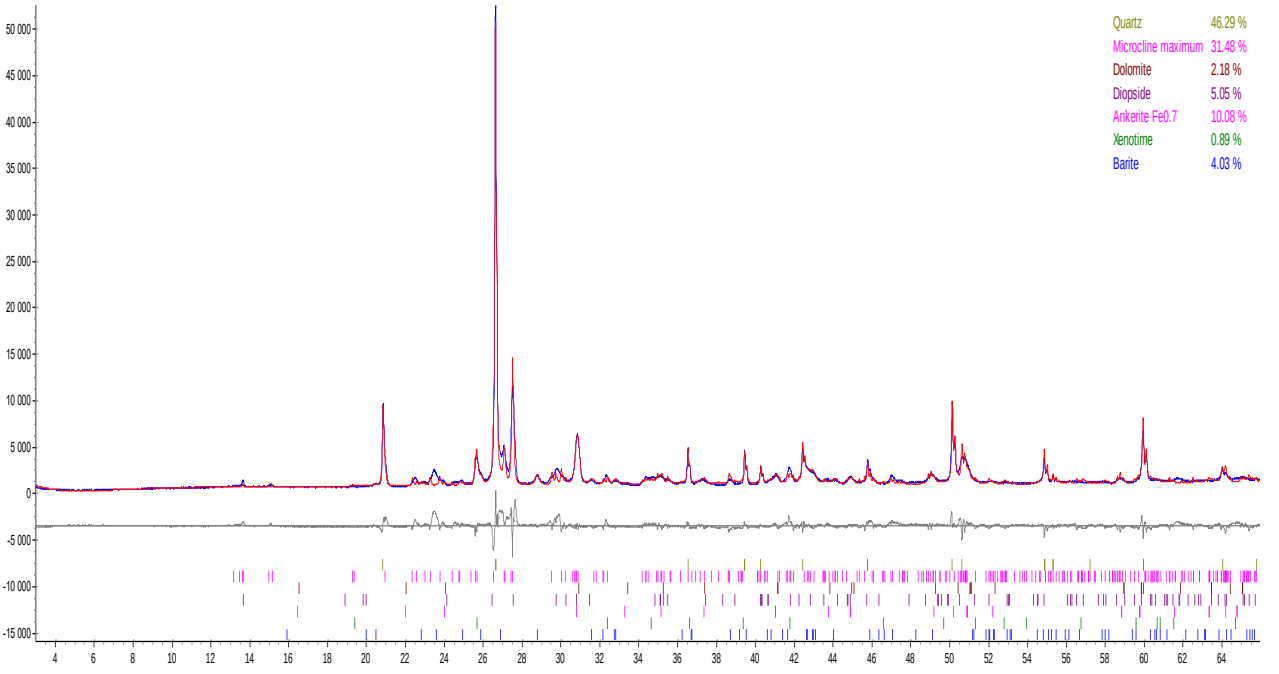

160471: AM-16-003B

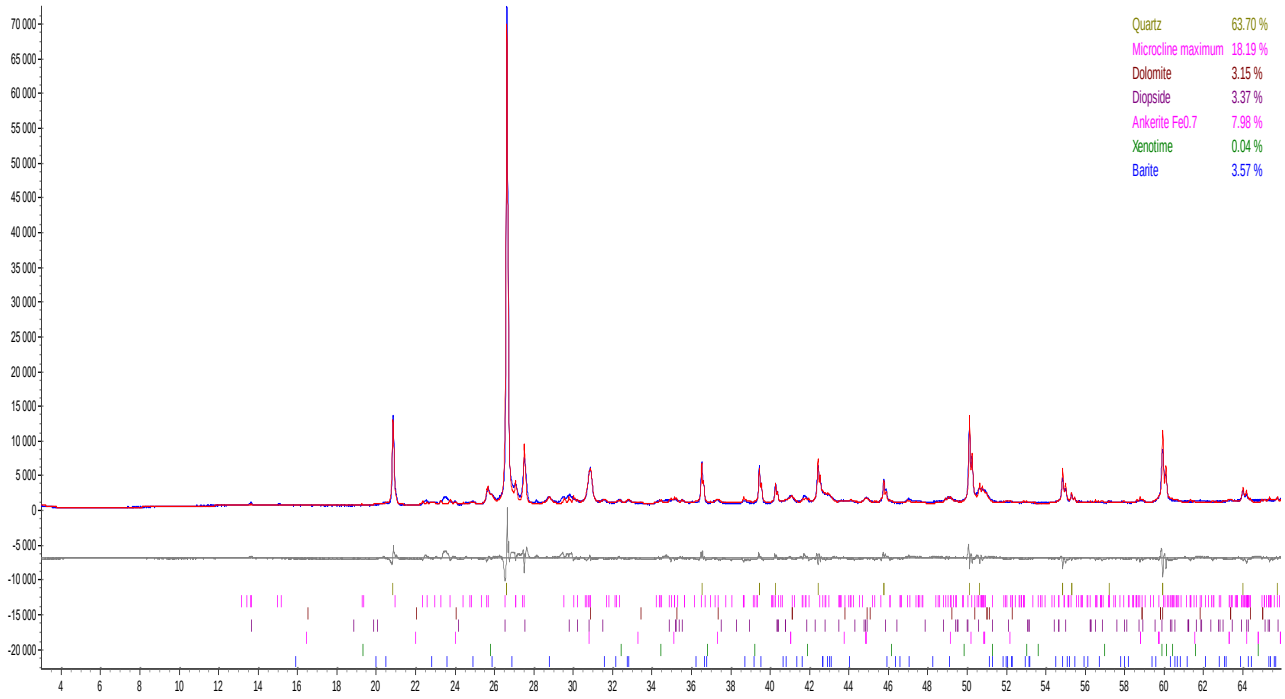


160472: AM-16-004

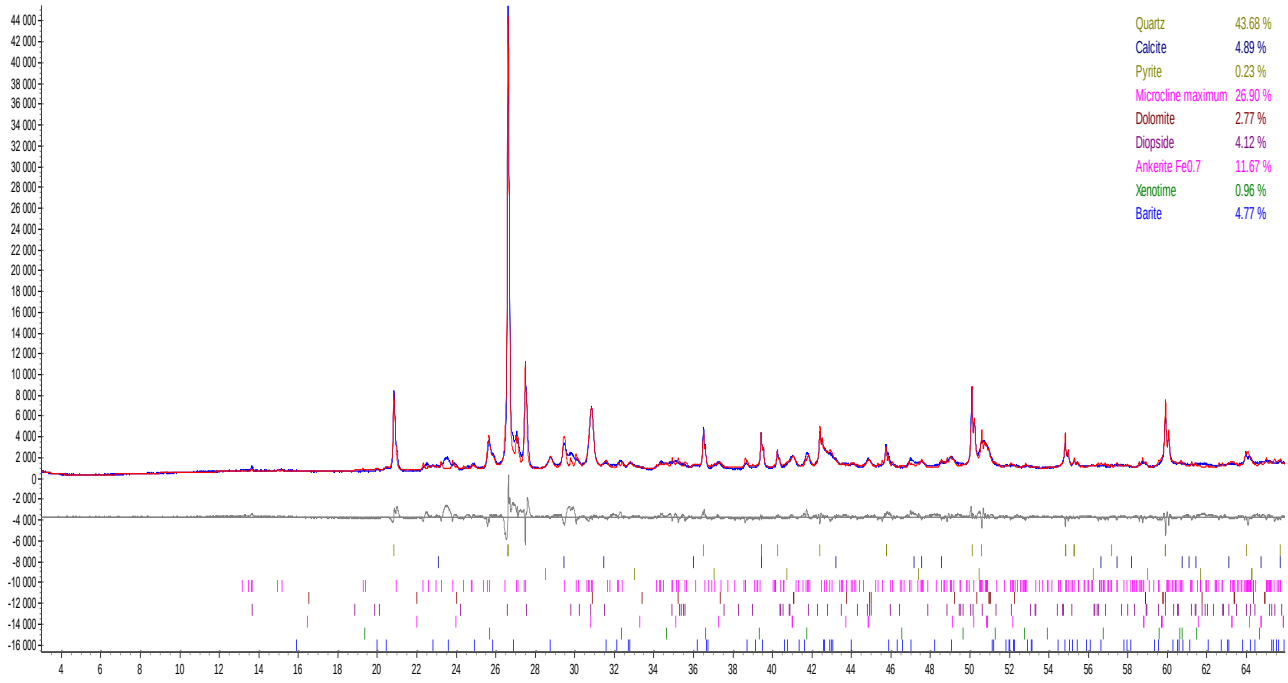

160473: AM-16-005

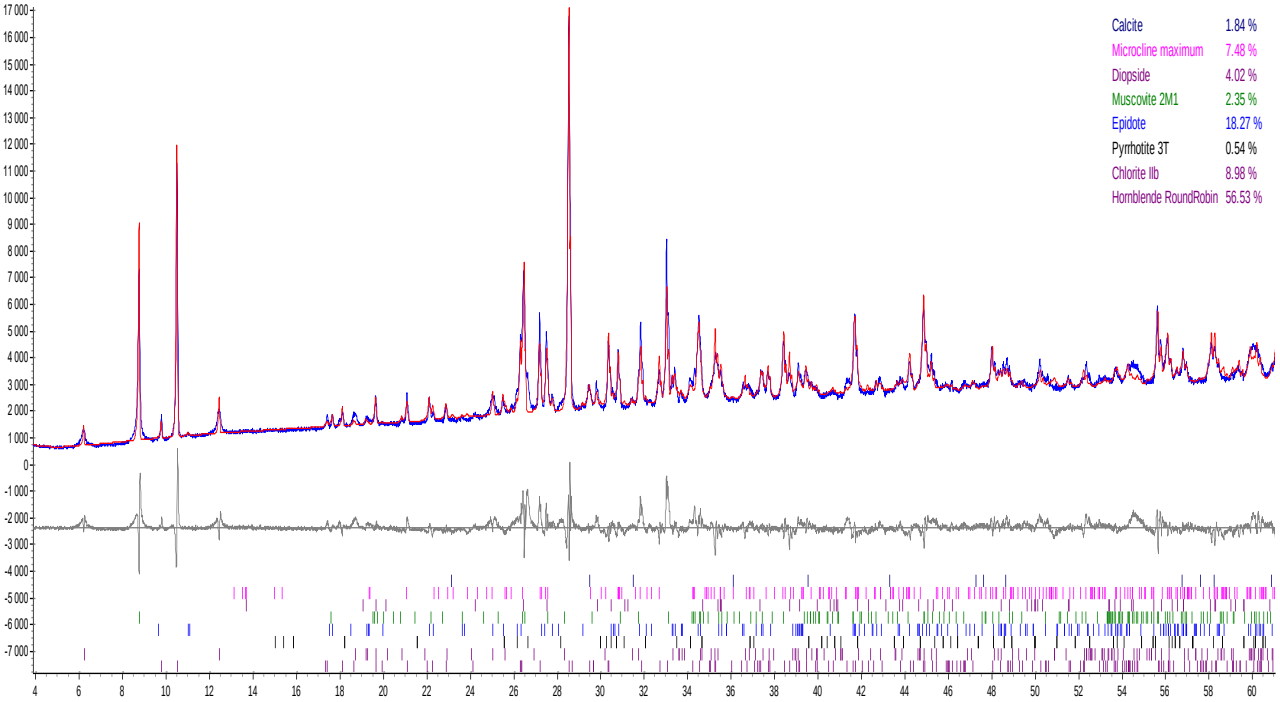


160474: AM-16-007

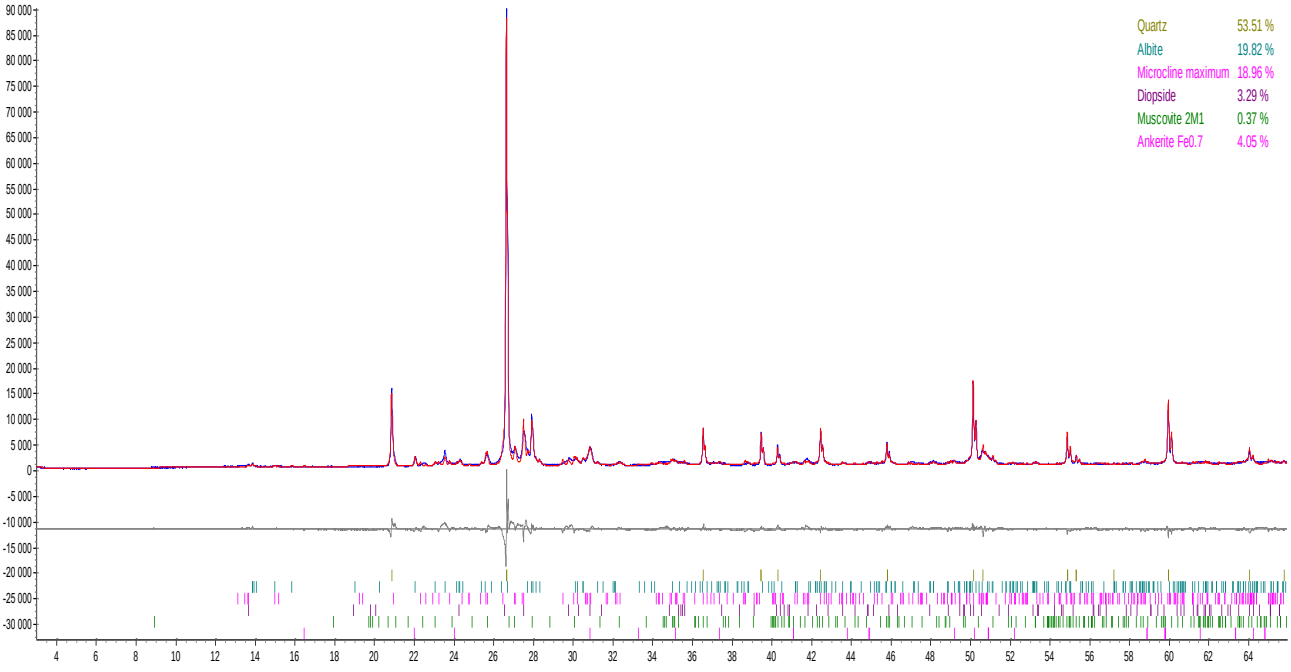

160475: AM-16-008

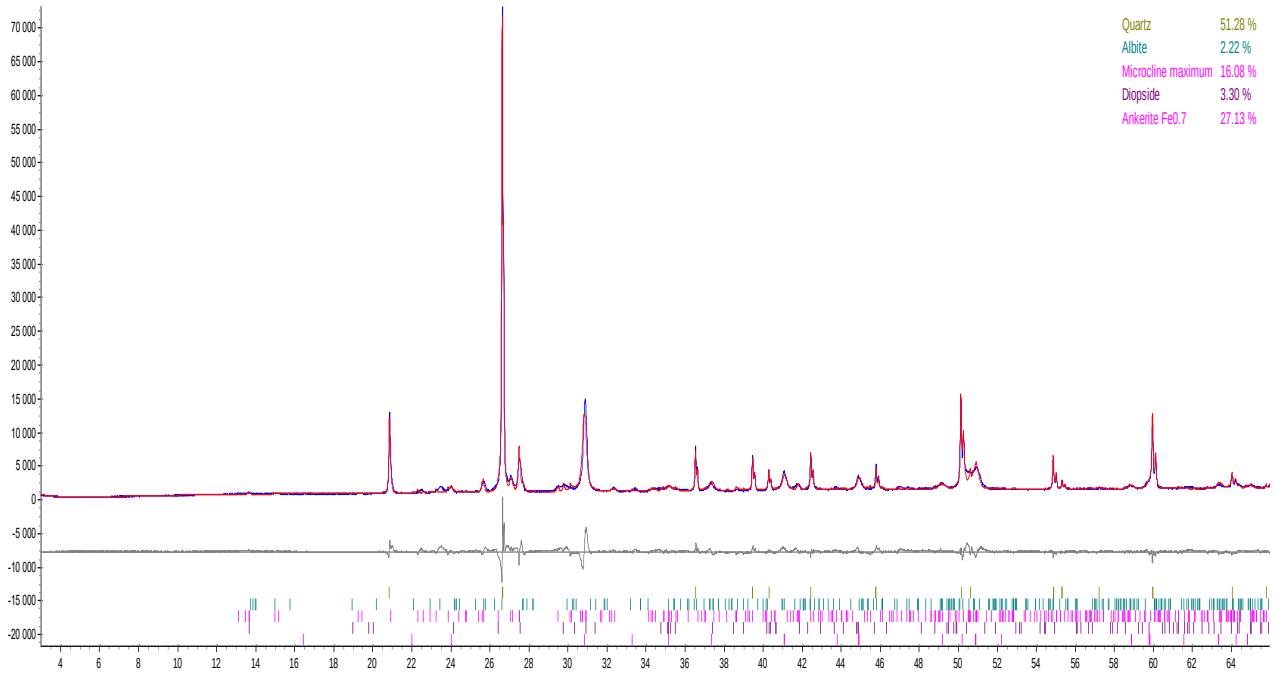


160476: AM-16-009

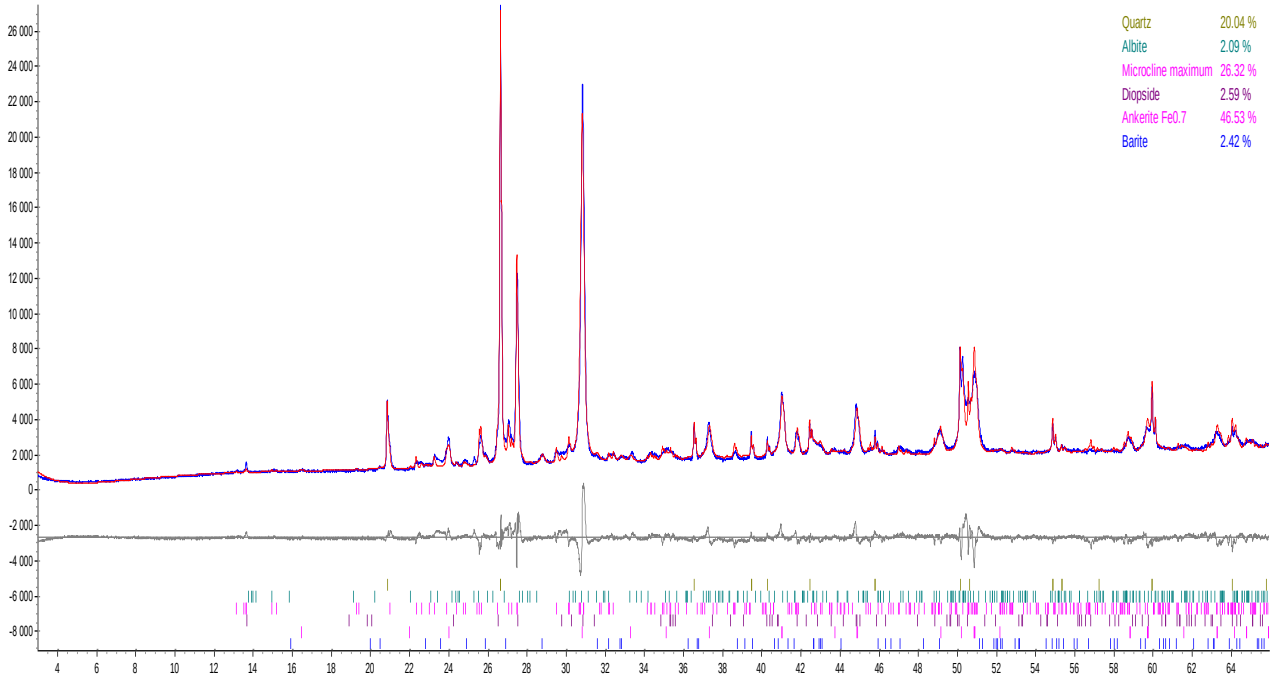

160477: AM-16-010A

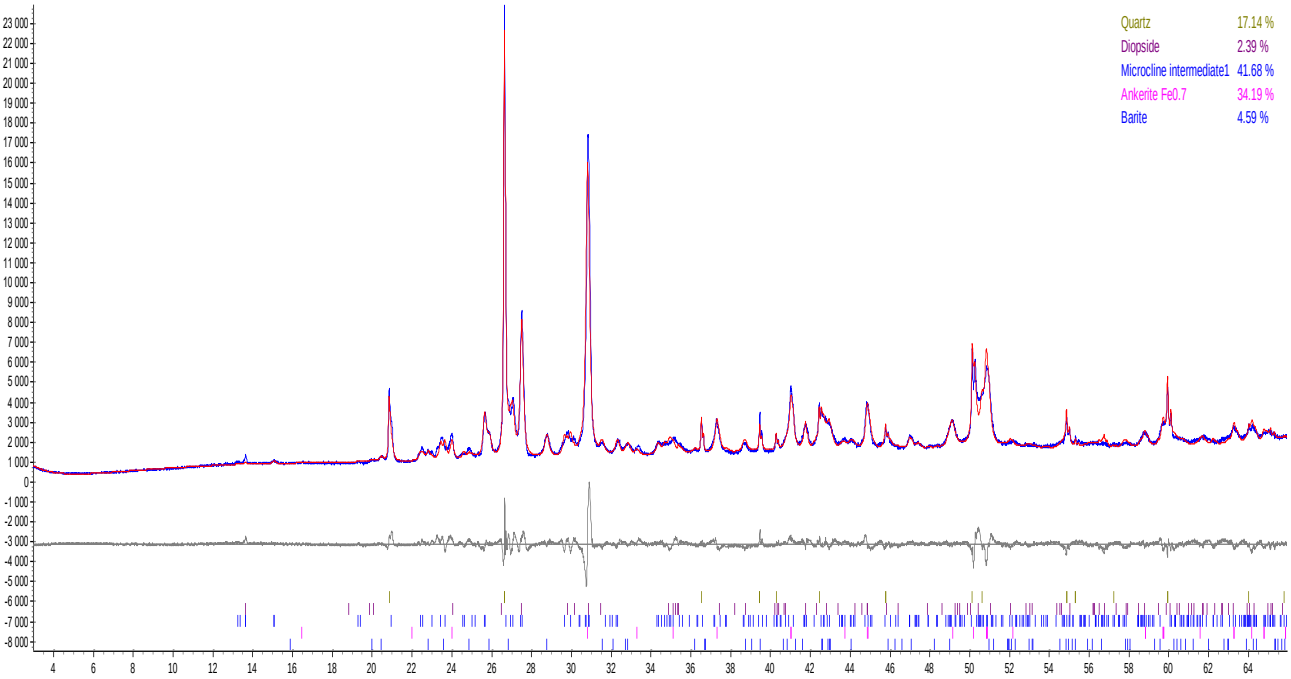


160478: AM-16-010B

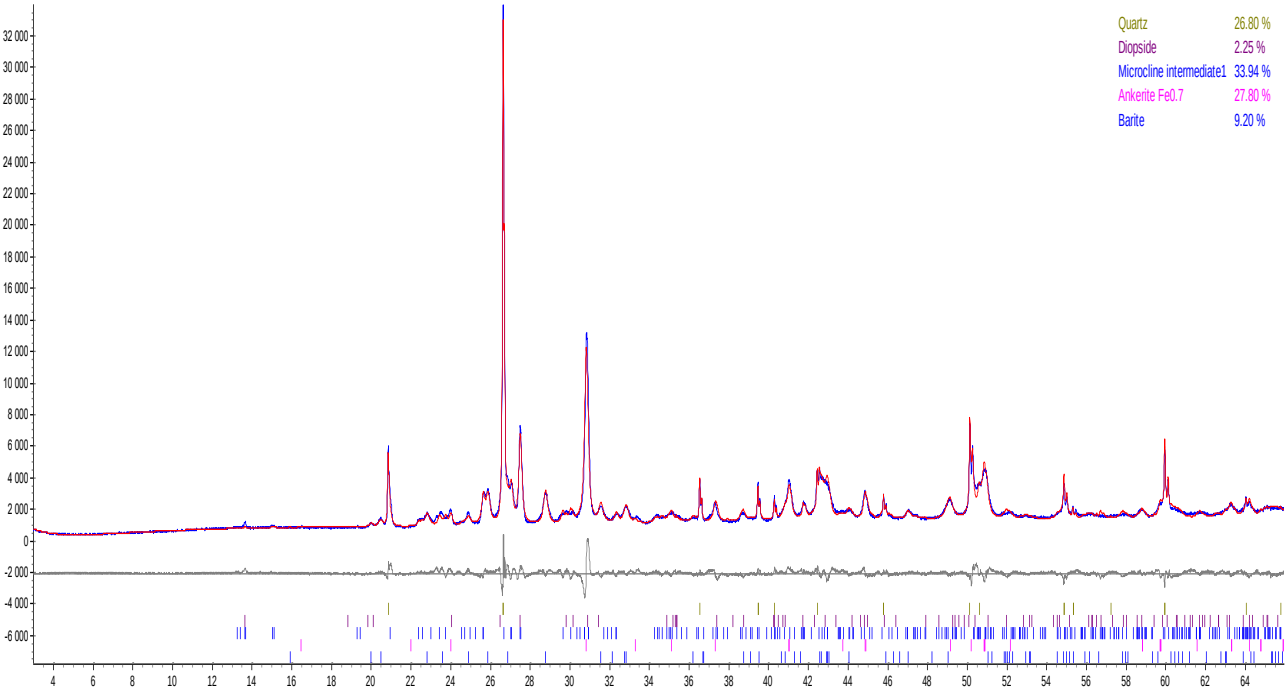

# Appendix V. Analyses of mineral chemistry from SEM

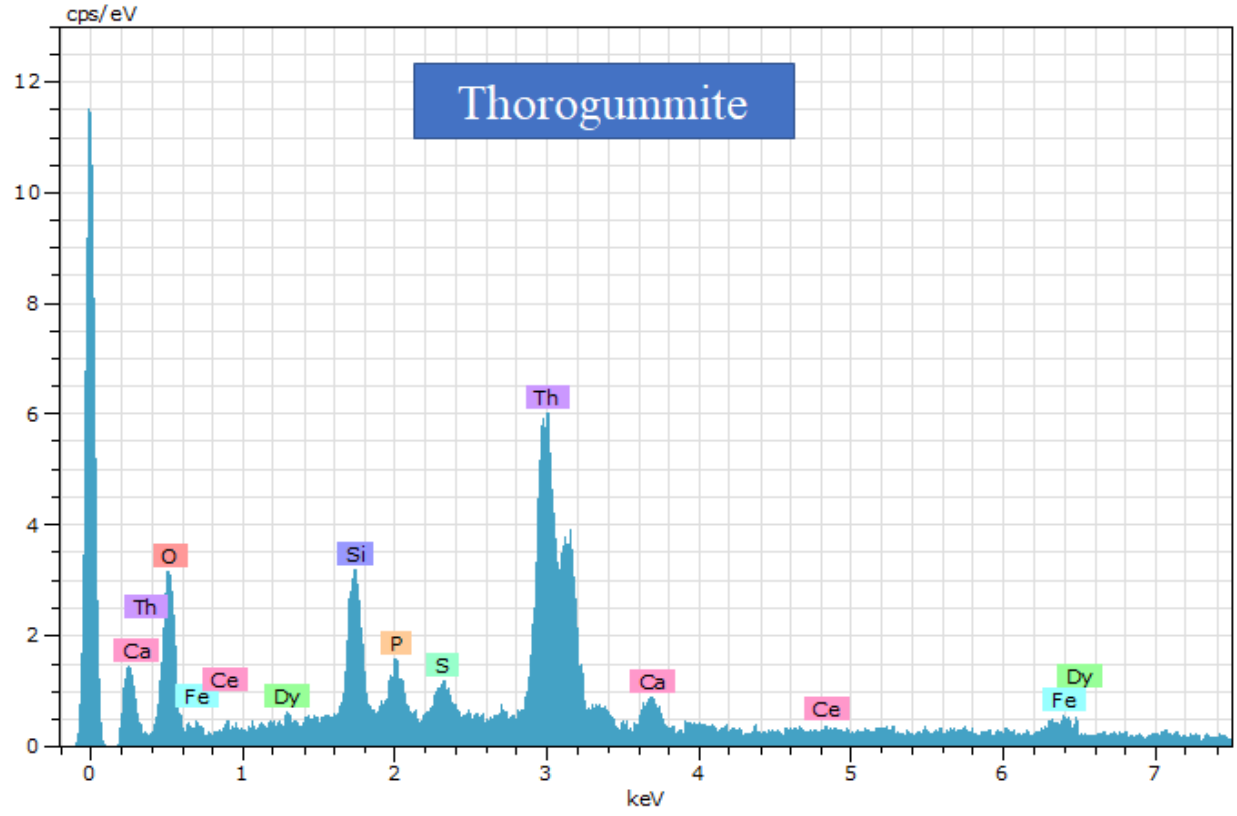


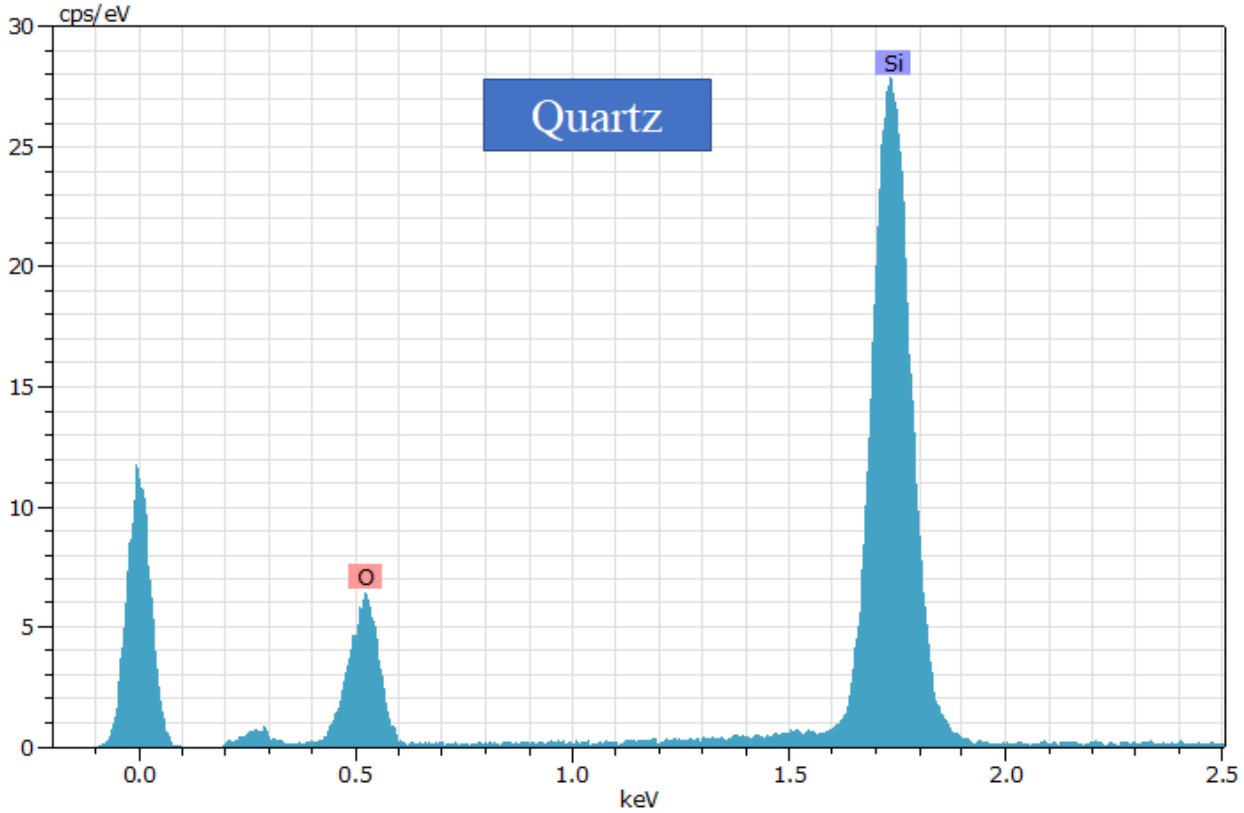

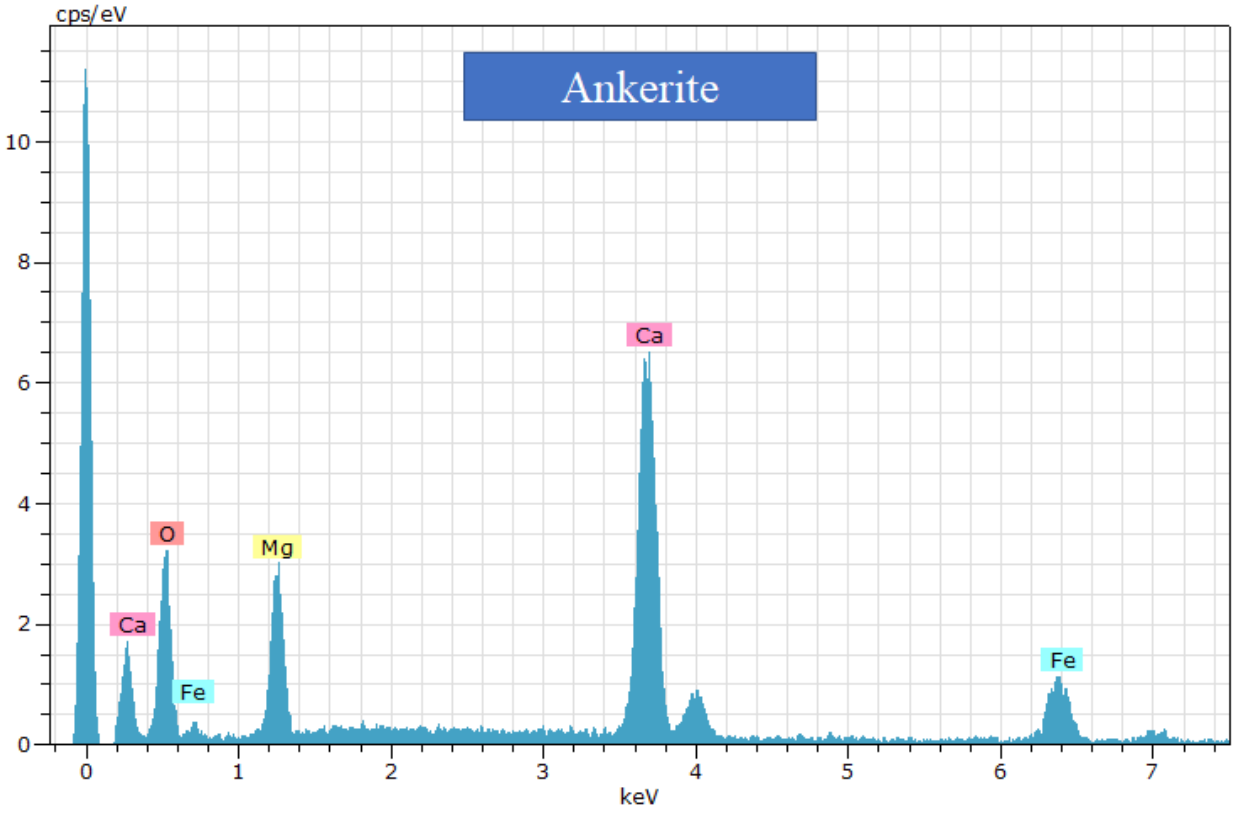
cps/eV
Ankerite
Ca
O
Mg
Ca
Fe
Fe
keV

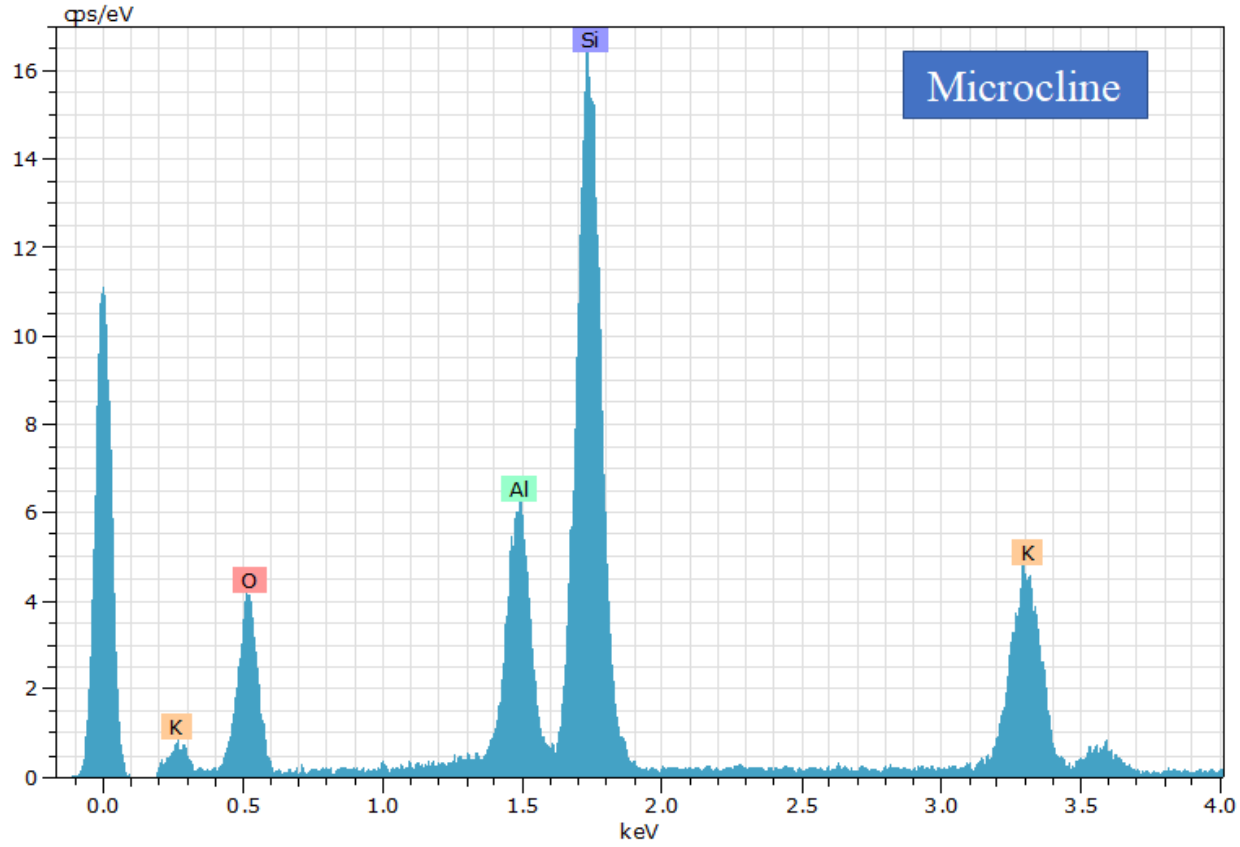
cps/eV
Si
Microcline
Al
O
K
K
keV

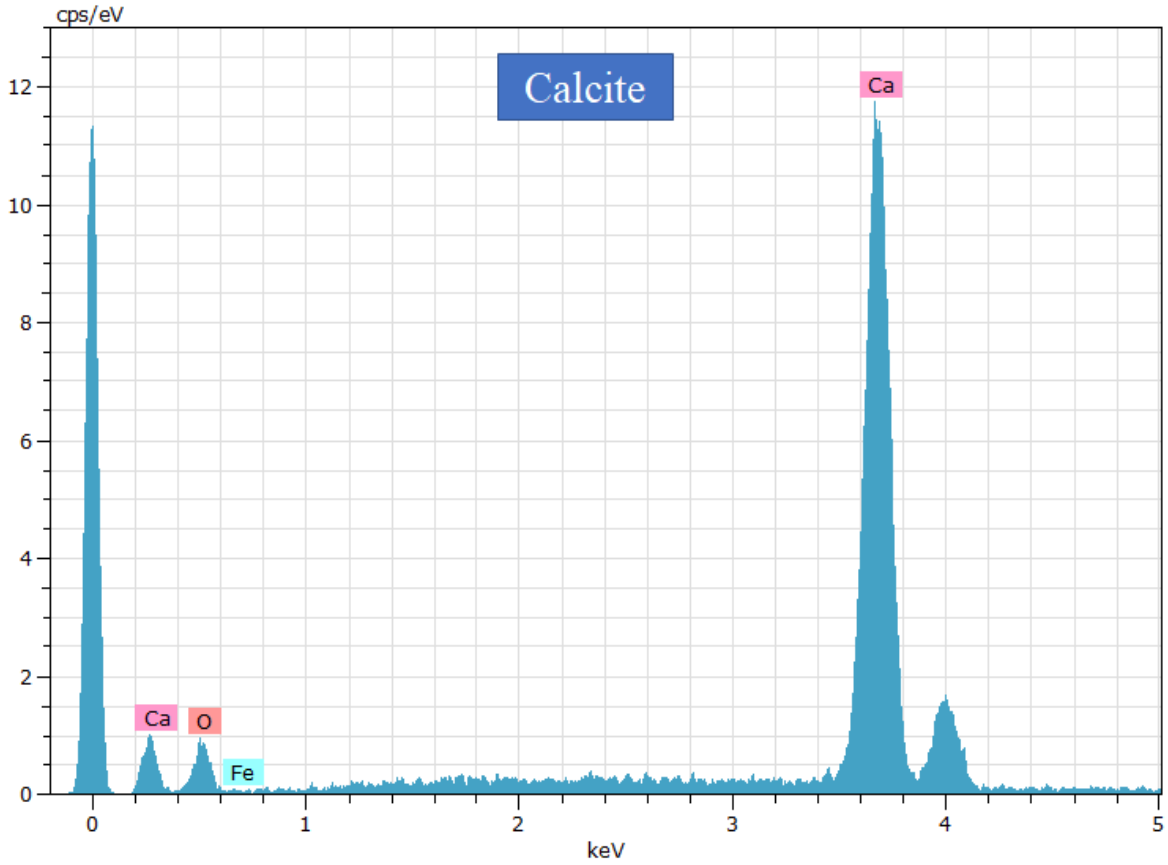
cps/eV
Calcite
Ca
Ca
O
Fe
keV

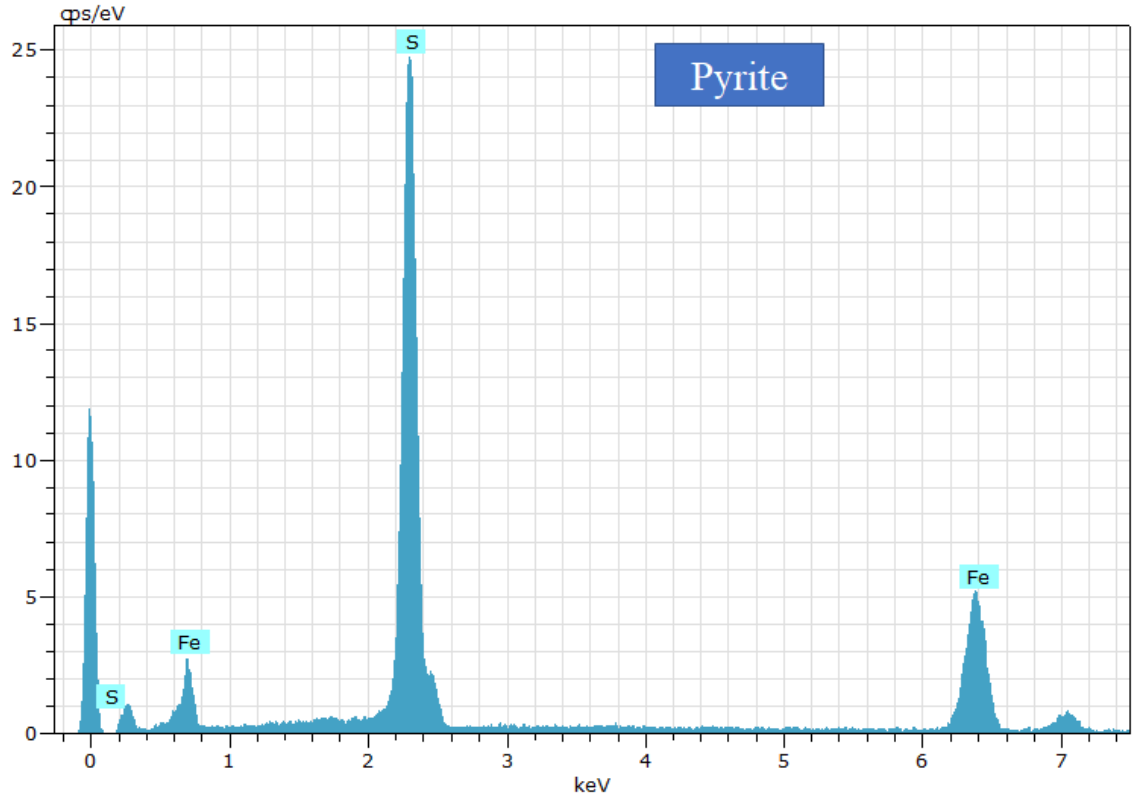
cps/eV
Pyrite
S
Fe
S
Fe
keV

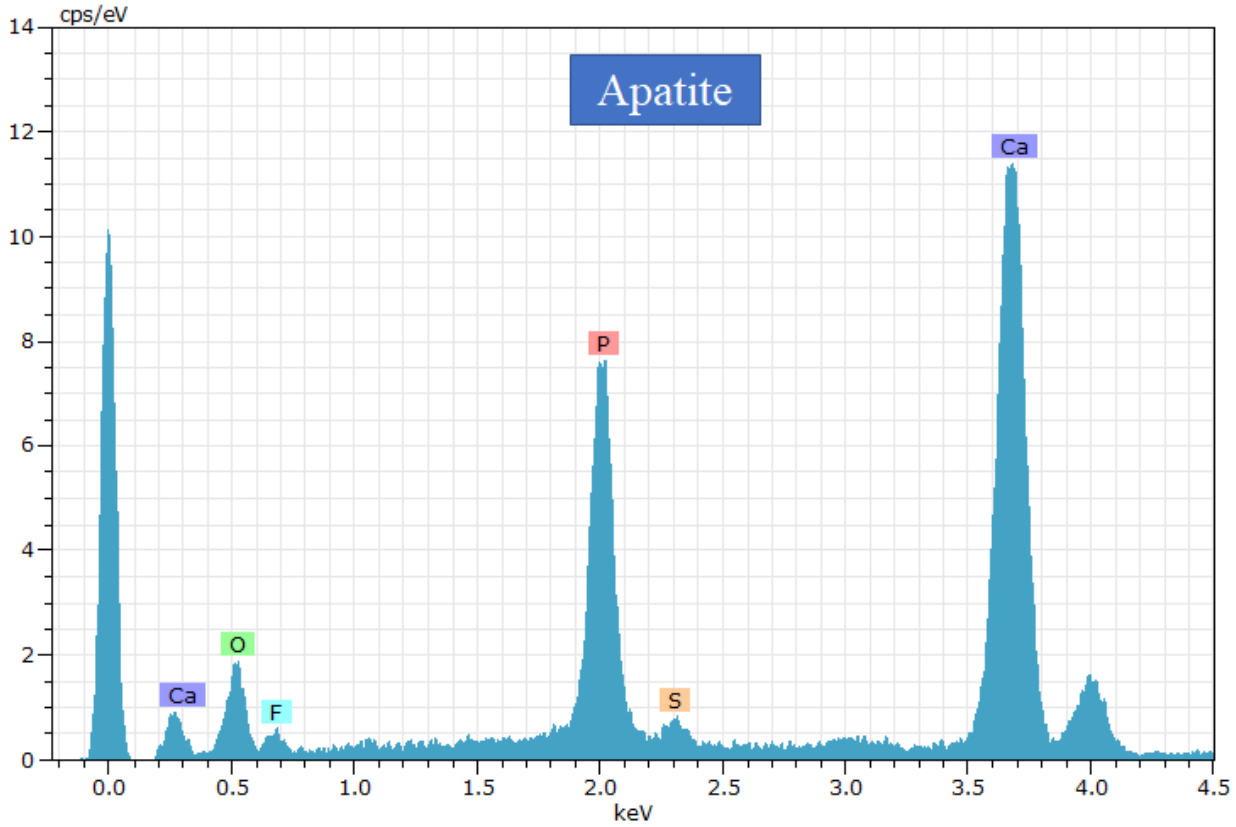
cps/eV
Apatite
Ca
P
O
Ca
F
S
keV

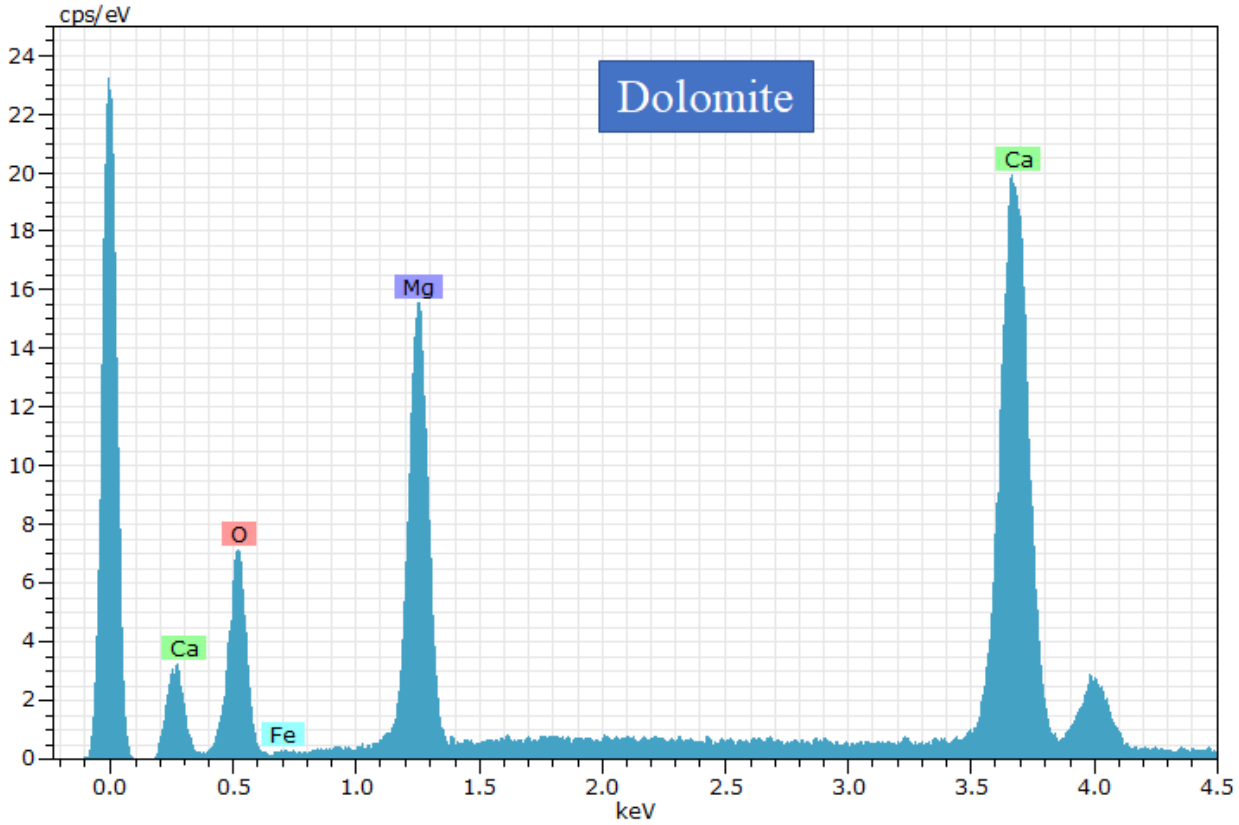
cps/eV
Dolomite
Ca
Mg
O
Ca
Fe
keV

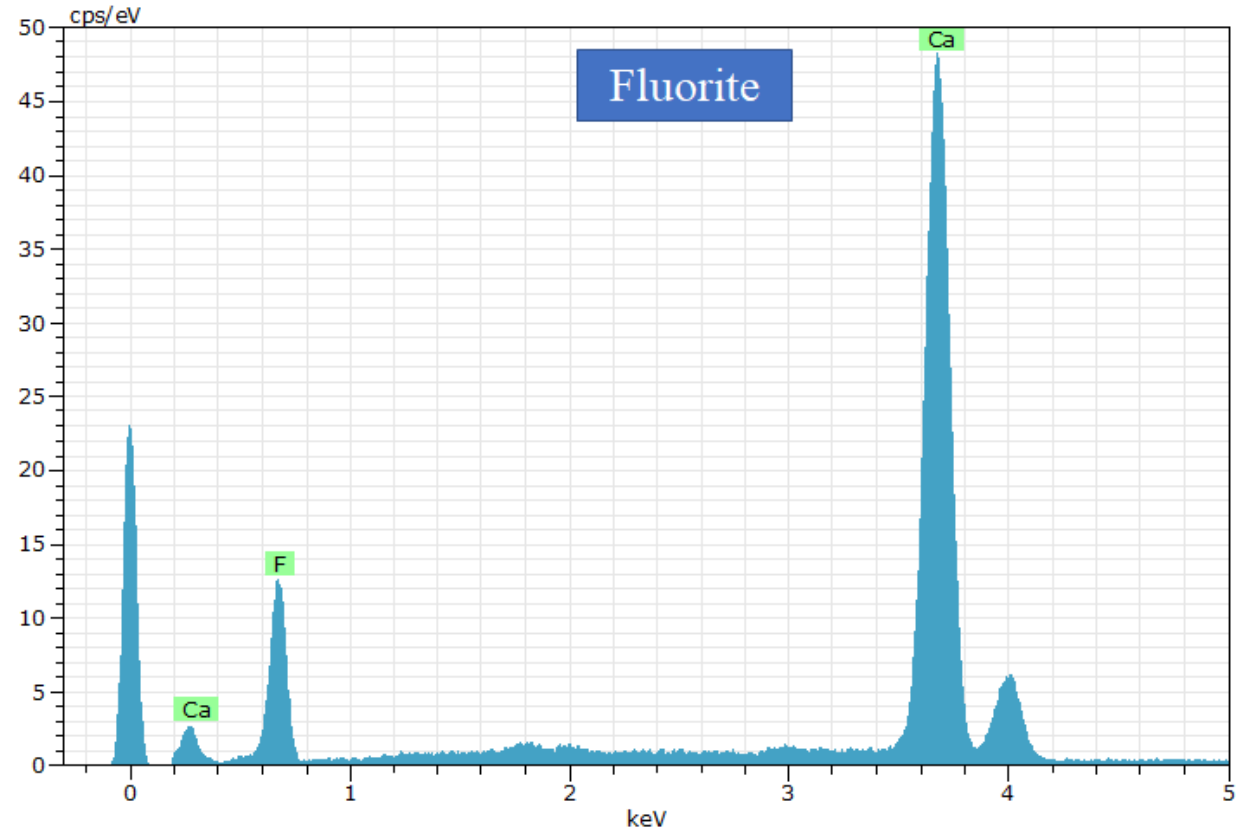
cps/eV
Fluorite
Ca
F
Ca
keV

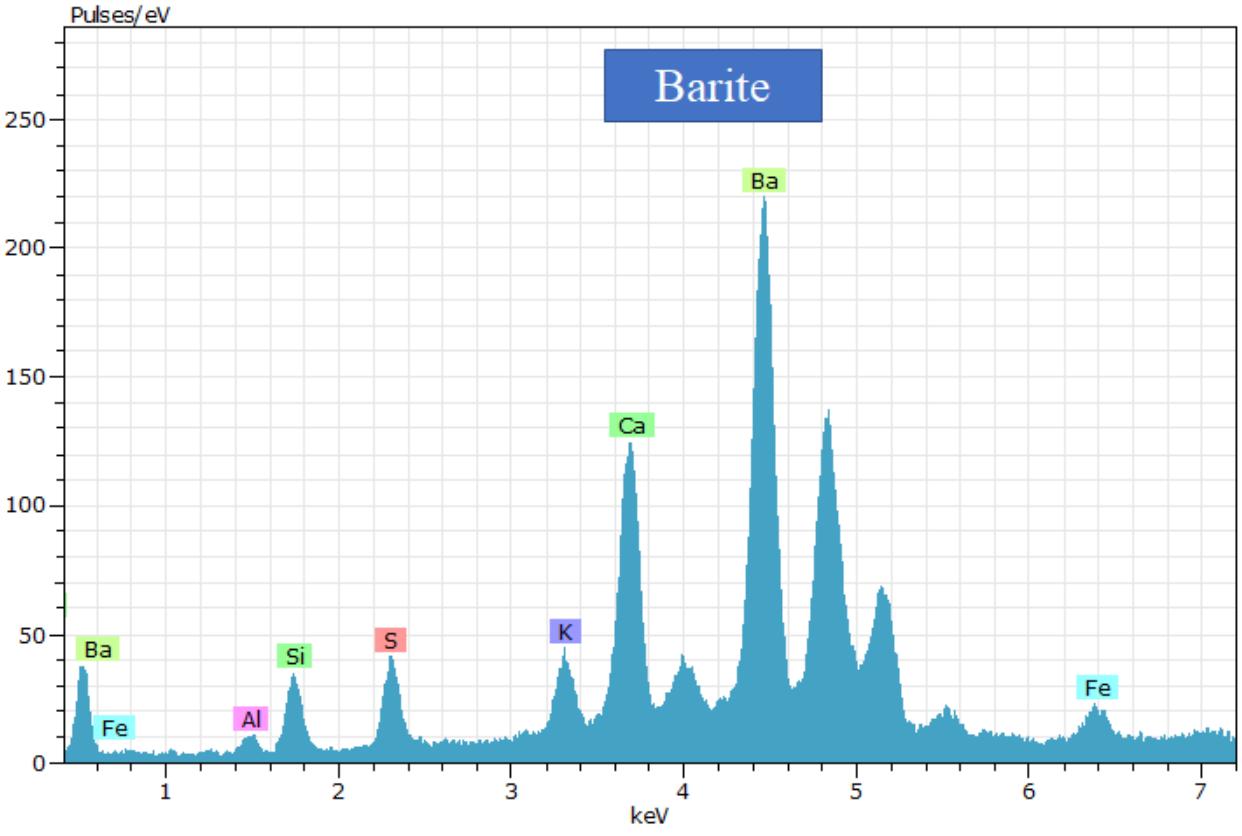
Pulses/eV
Barite
Ba
Ca
K
S
Si
Al
Ba
Fe
Fe
keV

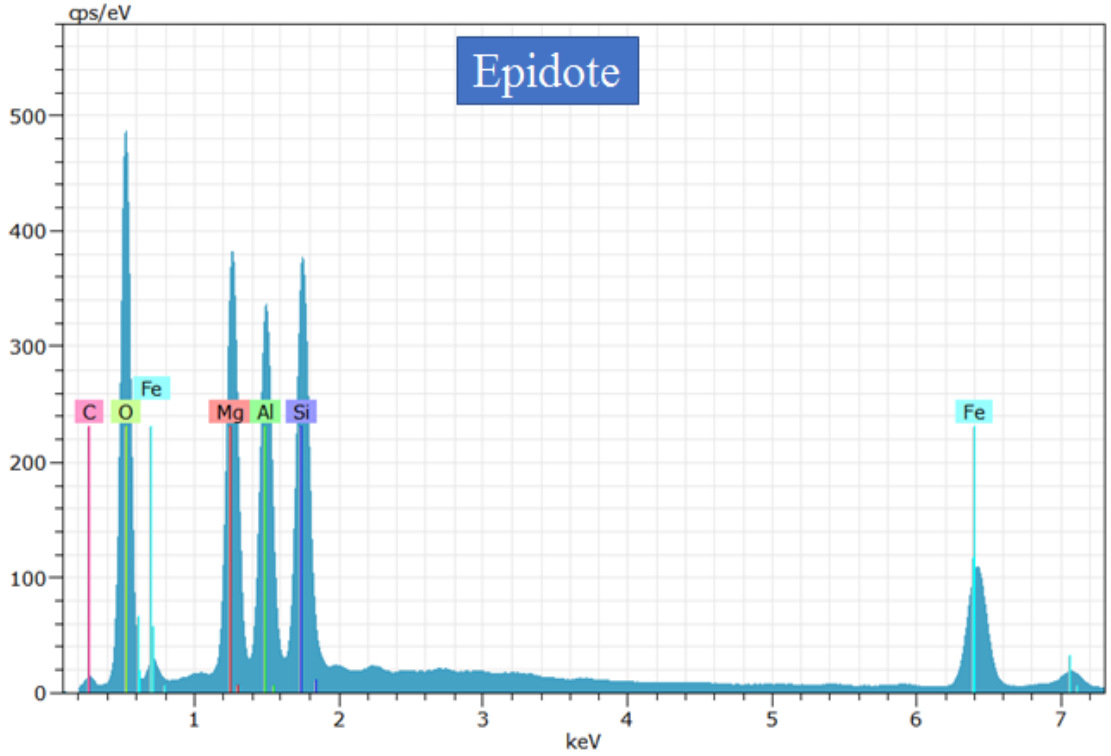
cps/eV
Epidote
500
400
300
200
100
0
C
O
Fe
Mg
Al
Si
Fe
1
2
3
4
5
6
7
keV

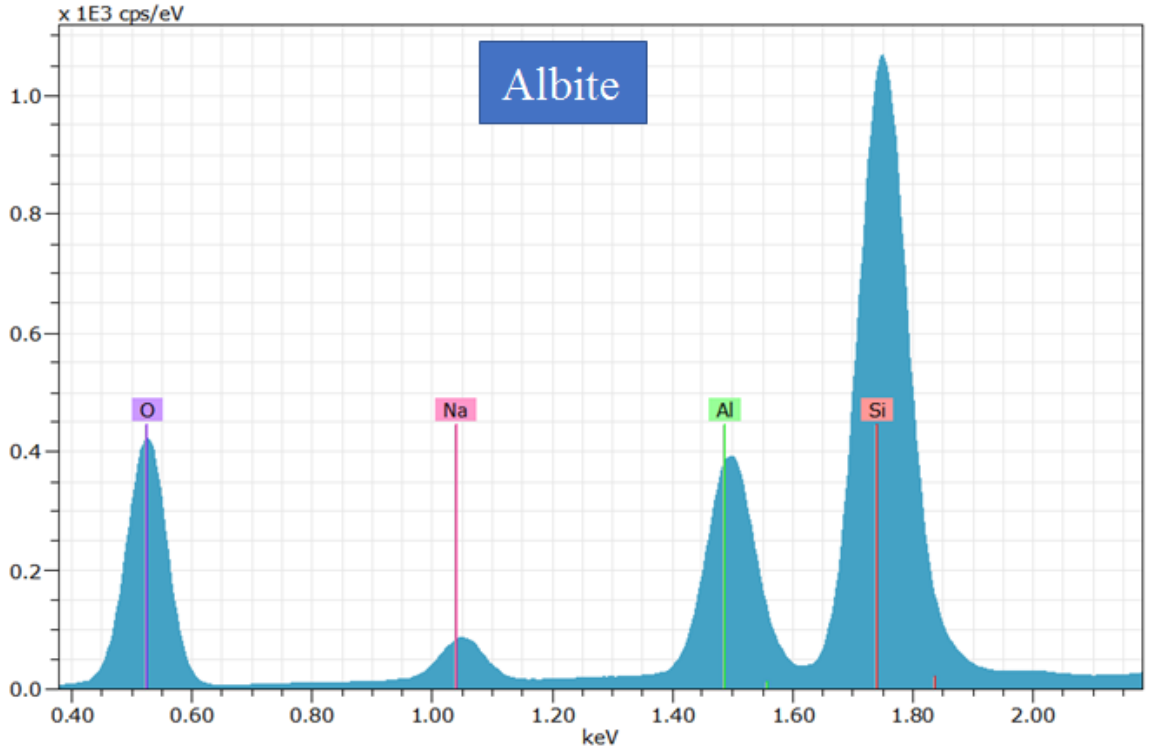
x 1E3 cps/eV
Albite
1.0
0.8
0.6
0.4
0.2
0.0
O
Na
Al
Si
0.40
0.60
0.80
1.00
1.20
1.40
1.60
1.80
2.00
keV

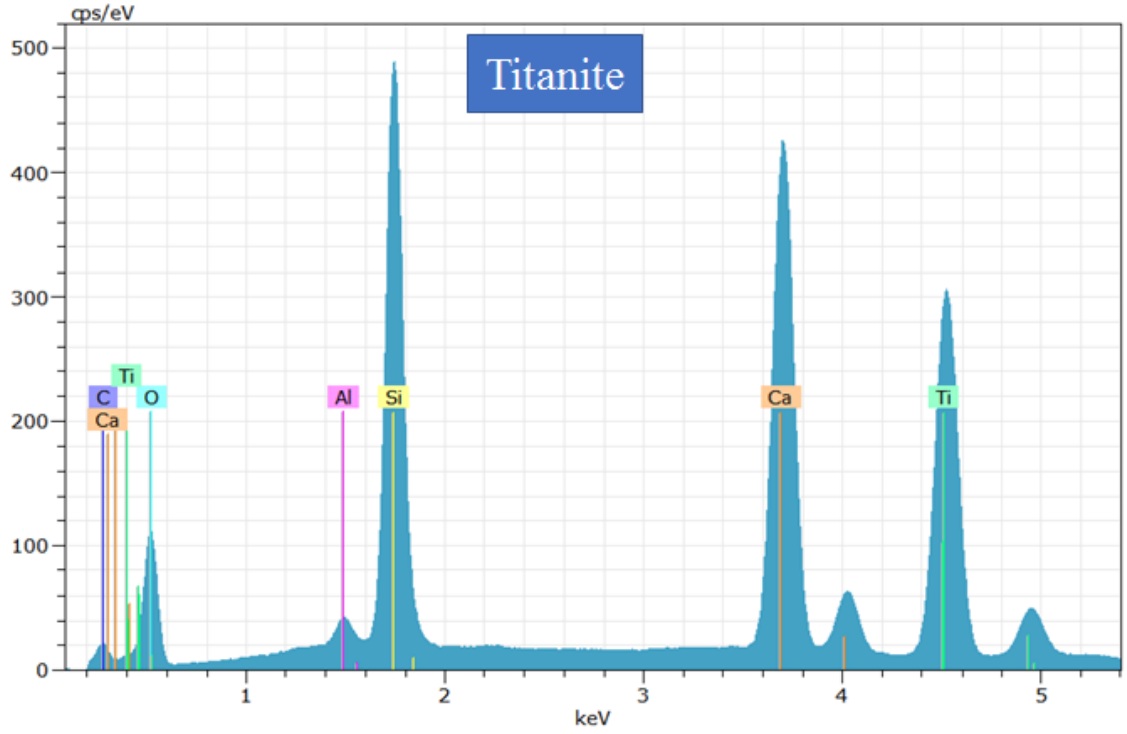
cps/eV
Titanite
500
400
300
200
100
0
Ti
C
O
Ca
Al
Si
Ca
Ti
1
2
3
4
5
keV

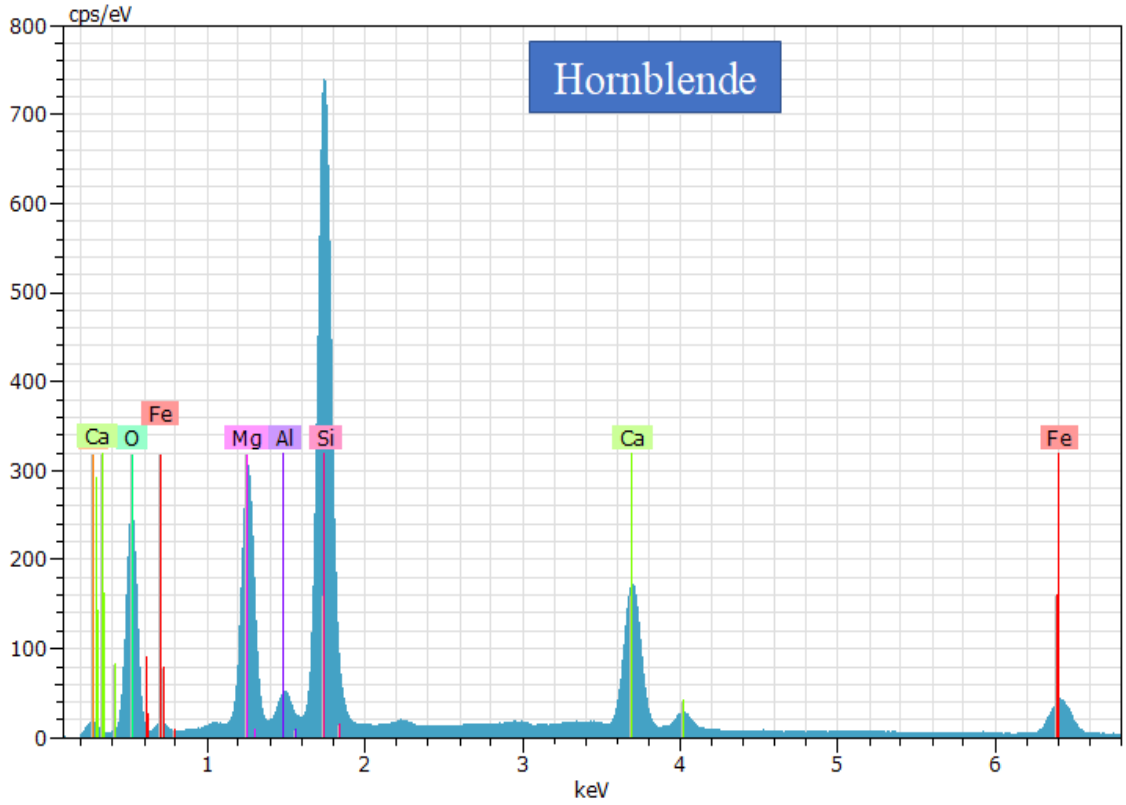
cps/eV
Hornblende
800
700
600
500
400
300
200
100
0
Fe
Ca
O
Mg
Al
Si
Ca
Fe
1
2
3
4
5
6
keV

# Appendix VI: Scanned pictured for thin sections

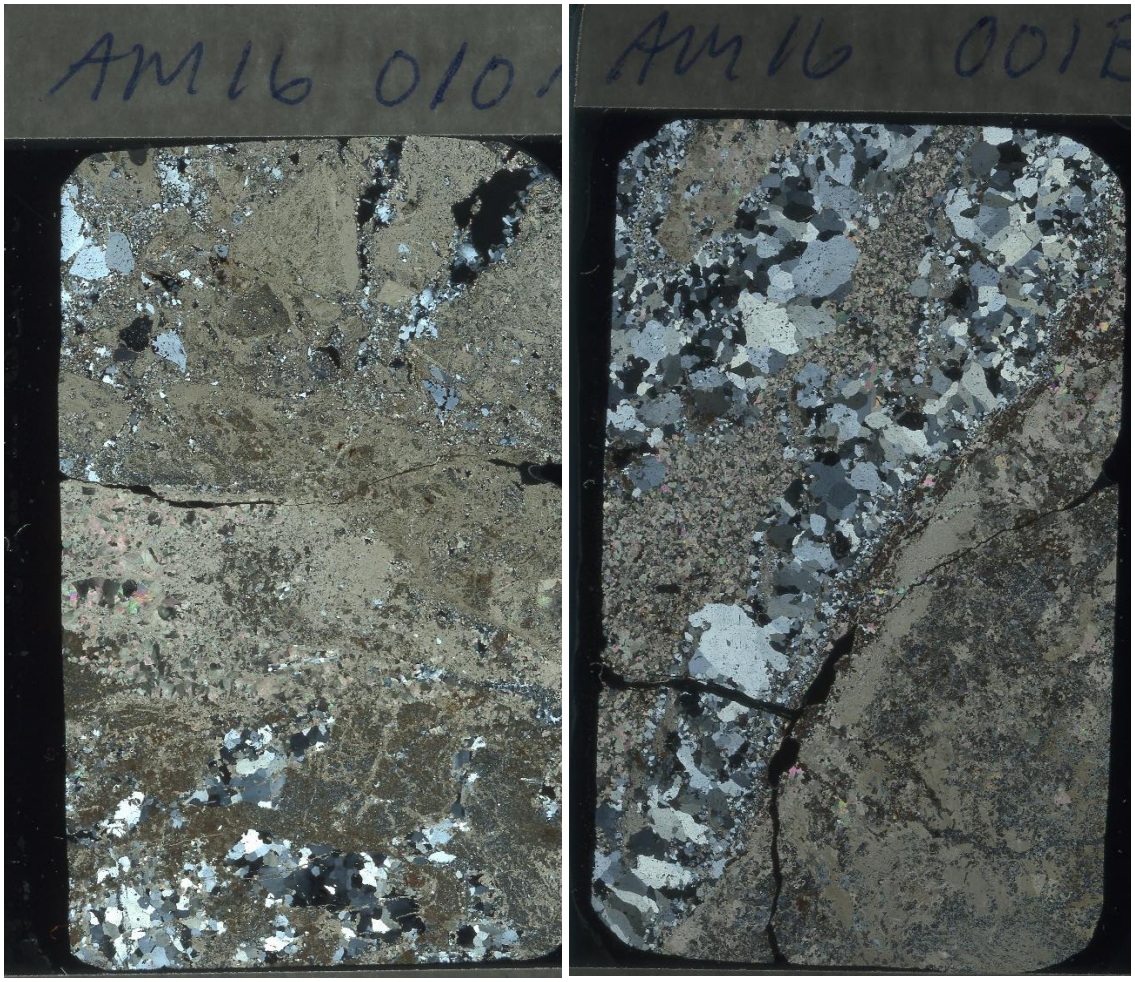


AM16 002


AM16 003A

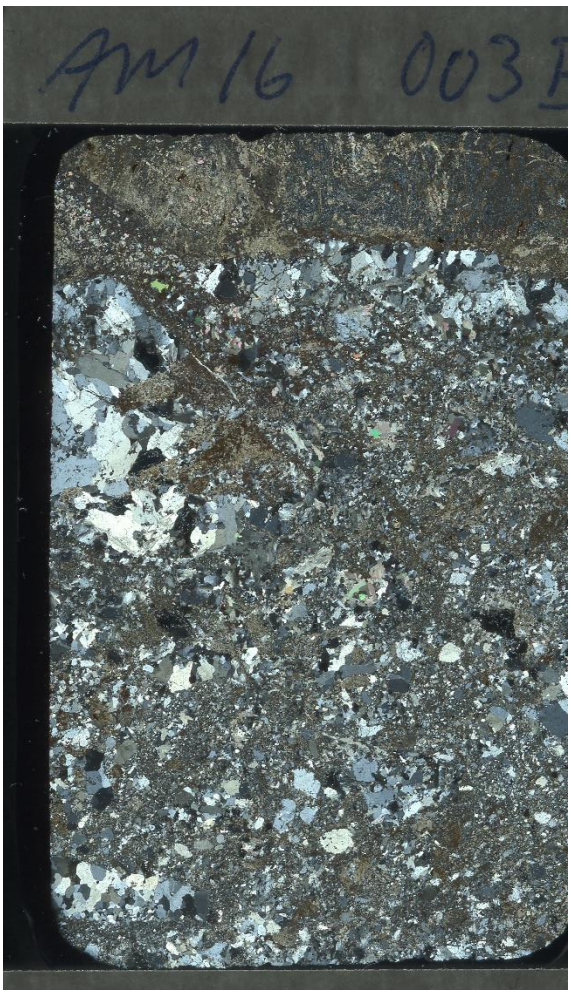
AM 16 003

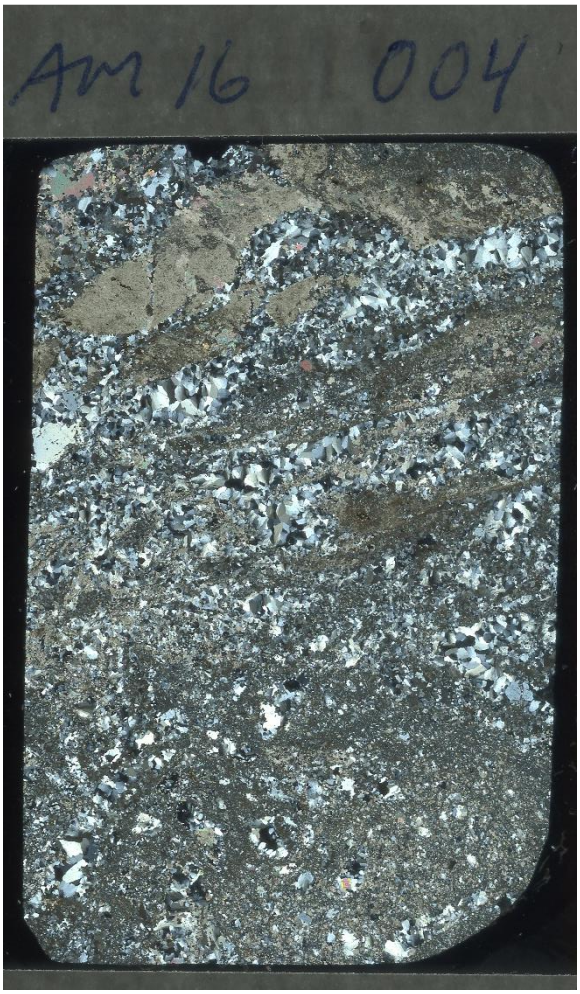
AM 16 004

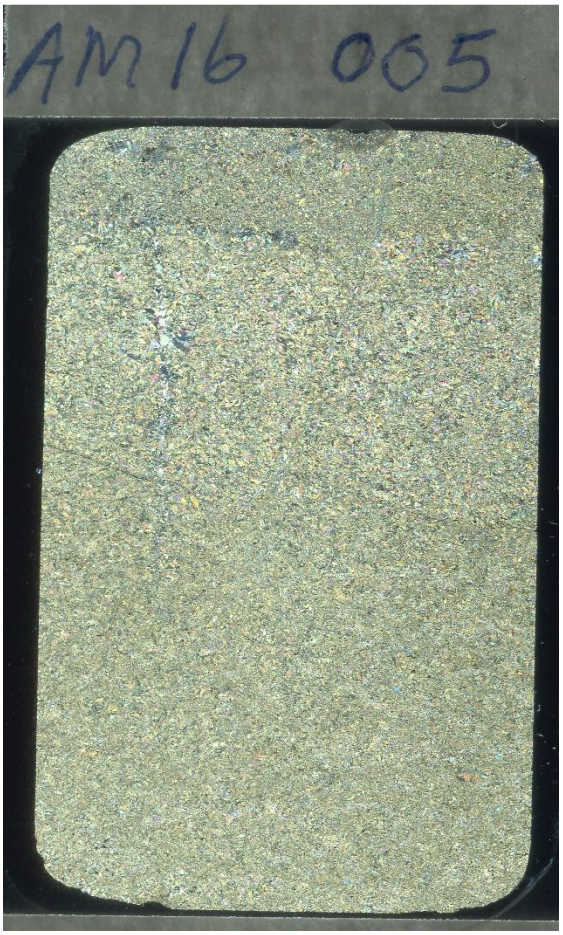
AM 16 005

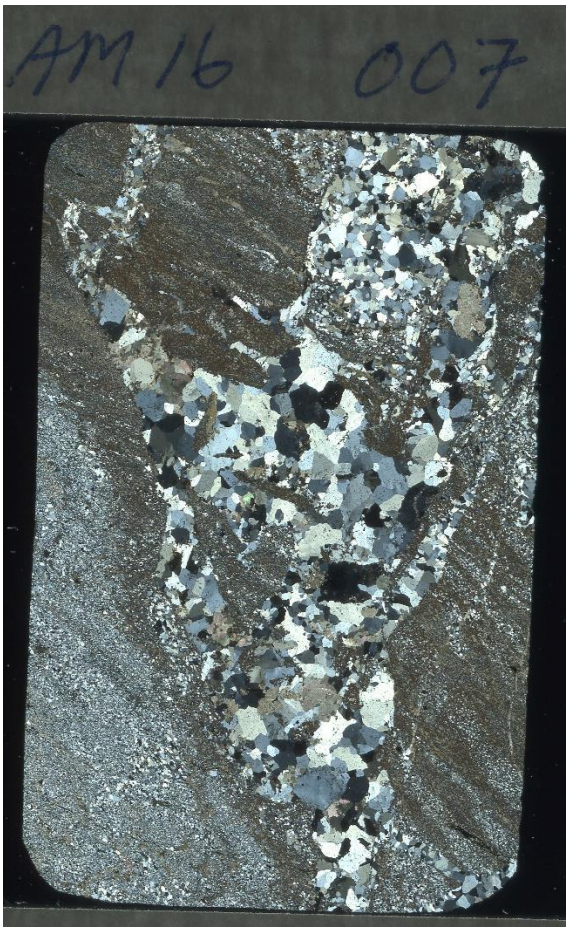
AM 16 007


AM16 008

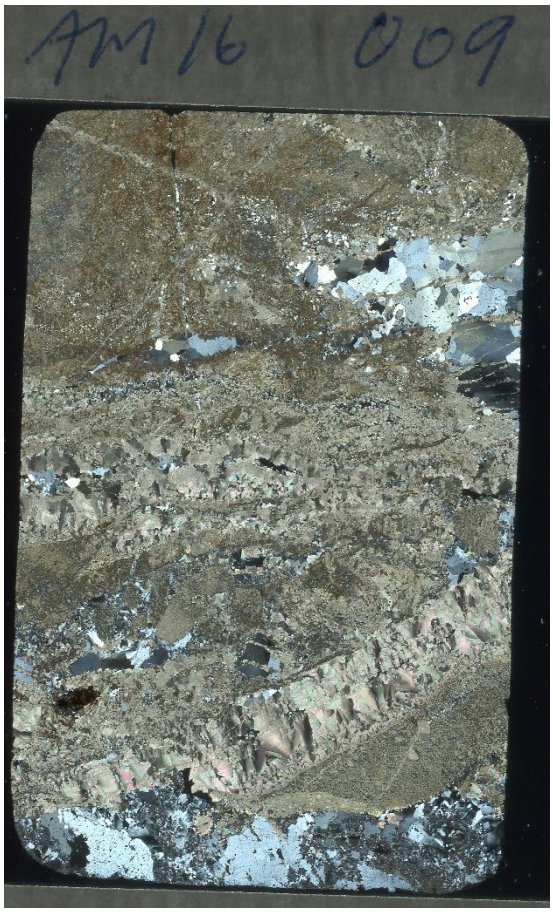
AM16 009


AM16 010A

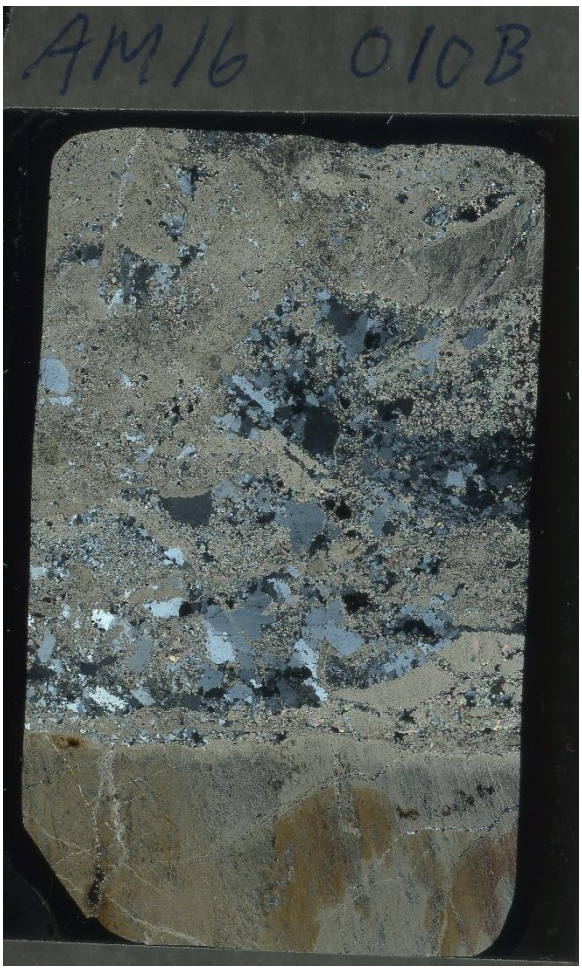
AM16 010B